

Analytical and Computational Tools for the Study of Grazing Bifurcations of Periodic Orbits and Invariant Tori

Phanikrishna Thota

Dissertation submitted to the Faculty of the
Virginia Polytechnic Institute and State University
in partial fulfillment of the requirements for the degree of

Doctor of Philosophy
in
Engineering Mechanics

Dr. Harry Dankowicz, Co-chair

Dr. Romesh Batra, Co-chair

Dr. Ali Nayfeh

Dr. Scott Hendricks

Dr. Daniel Inman

Dr. Mark Paul

February 2, 2007

Blacksburg, Virginia

Keywords: Hybrid Dynamical Systems, Grazing Bifurcations, Co-dimension-one Tori,
Co-dimension-two Tori, Discontinuity Mapping, Continuation Tools

Copyright 2007, Phanikrishna Thota

Analytical and Computational Tools for the Study of Grazing Bifurcations of Periodic Orbits and Invariant Tori

Phanikrishna Thota

(ABSTRACT)

The objective of this dissertation is to develop theoretical and computational tools for the study of qualitative changes in the dynamics of systems with discontinuities, also known as nonsmooth or hybrid dynamical systems, under parameter variations. Accordingly, this dissertation is divided into two parts.

The analytical section of this dissertation discusses mathematical tools for the analysis of hybrid dynamical systems and their application to a series of model examples. Specifically, qualitative changes in the system dynamics from a nonimpacting to an impacting motion, referred to as grazing bifurcations, are studied in oscillators where the discontinuities are caused by impacts. Here, the study emphasizes the formulation of conditions for the persistence of a steady state motion in the immediate vicinity of periodic and quasiperiodic grazing trajectories in an impacting mechanical system. A local analysis based on the discontinuity-mapping approach is employed to derive a normal-form description of the dynamics near a grazing trajectory. Also, the results obtained using the discontinuity-mapping approach and direct numerical integration are found to be in good agreement. It is found that the instabilities caused by the presence of the square-root singularity in the normal-form description affect the grazing bifurcation scenario differently depending on the relative dimensionality of the state space and the steady state motion at the grazing contact.

The computational section presents the structure and applications of a software program, $\widehat{\text{TC}}$, developed to study the bifurcation analysis of hybrid dynamical systems. Here, we present a general boundary value problem (BVP) approach to locate periodic trajectories corresponding to a hybrid dynamical system under parameter variations. A methodology to compute the eigenvalues of periodic trajectories when using the BVP formulation is illustrated using a model example. Finally, bifurcation analysis of four model hybrid dynamical

systems is performed using $\widehat{\text{TC}}$.

This work was supported by the National Science Foundation, Division of Civil and Mechanical Systems, grant numbers — 237370 and — 635469.

Dedication

To my mother

Acknowledgments

This dissertation, while an individual work, benefited from the great insights and direction of several individuals. Particularly, Dr. Harry Dankowicz, my dissertation advisor, has been a role model for the most part of my Ph.D study. He exemplifies the hard work, in-depth knowledge and dedication, required for a successful academic career, which I strive to emulate. The experience of working with him has been an ever-increasing learning curve resulting in a better understanding of complex problems. His innovativeness never ceases to amaze me.

I would like to convey my sincere thanks to my committee members Dr. Romesh Batra (Co-chair), Dr. Ali Nayfeh, Dr. Scott Hendricks, Dr. Daniel Inman and Dr. Mark Paul for their time and insight, which reflected in the overall quality of this work. They have been very supportive during my preliminary exam and the dissertation proposal and also their helpful suggestions for the improvement of the work.

My friends Milu, Madhav, Kaushik, Surya, Vivek, Preeti, Lavanya, Raja, Anil and Sreenu were very helpful during my stay in Champaign, particularly during the last few months of my Ph.D. I would like to thank them for their affection and love that made my stay memorable. Kalpana, Manish, Pranitha, Kiran, Supriya, Jaya, Siddharth, Bindu, Maria and Apoorva have been role models in their own little ways. During the part of my Ph.D that I spent in Blacksburg, my interaction with them taught me to be enthusiastic in all aspects of life. Aditi, Naveen, Rajeswari, Rahul, Ravi, Chandu and Madhav supported me all through my Ph.D by being very good friends. My heartiest thanks to all the members,

Sambit, Wonmo, Bryan, Melih and Noe for their suggestions at different phases of this dissertation. I am obliged to Dr. Xiaopeng Zhao who was a post-doctoral researcher under Dr. Harry Dankowicz for his help in coding and writing manuscripts. Finally, I would like to express my sincere gratitude to all the team members, particularly to the leader Anshu, of the TEAM-ASHA-UIUC Chicago-marathon-2006 marathon team. Running this marathon helped me to build both physical and mental stability.

I feel most indebted to my mother, who always taught me the importance of education in life. She taught me that patience and perseverance are the two tools that can take a human being to the heights of success. Her words always encouraged me to face the unpredictable hardships and pushed me forward with her love when my abilities faltered. I would like to take this opportunity to thank her for moulding me into a successful being and dedicate this dissertation to her. My father, brothers and sisters stood by me whenever I needed them the most. This appreciation would be incomplete without mentioning about my little dog "Micky", though not physically present it is always in my thoughts as my best friend.

Mrs. Joyce Smith, graduate enrollment specialist in the department of Engineering Science and Mechanics at Virginia Tech, has been of great help during my stay away from Blacksburg. She helped me in taking care of some of the academic issues that occurred during my absence at Virginia Tech. I am greatly indebted to the National Science Foundation (NSF) for providing financial support for this work.

Contents

- 1 Introduction** **1**
- 1.1 Motivation 1
- 1.2 Impact Oscillators 3
- 1.3 Research Objectives 9
- 1.4 Synopsis 10

- 2 Dynamical Systems - Concepts and Theory** **12**
- 2.1 Smooth Dynamical Systems 13
- 2.2 Hybrid Dynamical Systems 15
- 2.3 Periodic Trajectories 23
- 2.4 Quasiperiodic Trajectories 24
- 2.5 Tangential Intersections 25
- 2.5.1 Discontinuity Maps 27
- 2.5.2 Global Poincaré Sections 32
- 2.5.3 Local Approximations 34
- 2.5.4 Hybrid Dynamical Systems 36

2.6	Local Stability	37
2.6.1	Periodic Trajectories	38
2.6.2	Quasiperiodic Trajectories	39
2.6.3	Lyapunov Exponents	39
2.7	Bifurcations	42
3	Grazing Bifurcations of Co-dimension-one Invariant Tori	45
3.1	Introduction	45
3.2	Grazing Bifurcations of a Co-dimension-one Periodic Attractor	47
3.3	Grazing Bifurcations of a Co-dimension-one Torus Attractor	52
3.4	Summary	66
4	Grazing Bifurcations of Co-dimension-two Invariant Tori	68
4.1	Introduction	68
4.2	Grazing Bifurcations of a Co-dimension-two Periodic Attractor	70
4.3	Grazing Bifurcations of a Co-dimension-two Torus Attractor	74
4.4	On Square-root Instability	81
4.5	Summary	84
5	TC-HAT ($\widehat{\text{TC}}$) – A Continuation Toolbox for the Analysis of Hybrid Dynamical Systems	88
5.1	Mathematical Foundation	89
5.1.1	Problem Formulations	90

5.1.2	Solving Boundary-Value-Problems (BVP's) using Collocation Methods	93
5.1.3	Pseudo-Arclength Continuation	101
5.2	$\widehat{\text{TC}}$ Functions	102
5.2.1	Single-parameter Continuation	103
5.2.2	Two-parameter Continuation	108
5.3	Illustrations using $\widehat{\text{TC}}$	109
5.3.1	Linear Oscillator	109
5.3.2	A Nonlinear MEMS Oscillator	112
5.3.3	Periodic Orbit in a Three-dimensional State Space	115
5.3.4	Periodic Orbit in a Four-dimensional State Space	117
5.4	Summary	118
6	Conclusions and Future Recommendations	122
6.1	Future Recommendations	123
	Bibliography	125
A	$\widehat{\text{TC}}$ Makefile	131
B	$\widehat{\text{TC}}$ Constants File gc.<name>	134
C	$\widehat{\text{TC}}$ Functions File <name>.f	135
D	$\widehat{\text{TC}}$ Constants File <name> .dat	146

List of Figures

1.1	Schematic of an impact oscillator.	4
1.2	A schematic diagram showing nonimpacting and grazing orbits along with the corresponding discontinuity surface.	5
2.1	A schematic representation of the index vector and its associated vector fields, event surfaces and state jump functions.	22
2.2	The figure illustrates a two-segment periodic trajectory corresponding to the microactuator described here. The index vectors that contain the information about the vector field, the terminal event surface and the state jump function corresponding to the each segment are also shown.	23
2.3	Illustration of a quasiperiodic motion. A Poincaré section is also shown where the trajectories intersect the torus in a closed curved (shown as a dotted ellipse).	25
2.4	Schematic of the trajectories near the grazing point depicting the discontinuity-mapping approach with \mathcal{D} and \mathcal{P} (upper panel) and \mathcal{P}' and \mathcal{P} (lower panel). Gray curves correspond to the trajectories that are on the side of \mathcal{P}' for which $h_{\mathcal{P}'} > 0$	29

3.1	Grazing periodic orbit corresponding to the dynamical system given by Eq. (3.1). Here, $\mu = 1$ and the discontinuity surface $h_{\mathcal{D}}(\mathbf{x}) = 0$ can also be seen as a dotted line at $x^1 = d$	48
3.2	Bifurcation diagrams showing the penetration $\pi(\mathbf{x})$ as a function of $\mu - \mu_*$ obtained using direct numerical simulation of the original dynamical system (left panel) and the composite Poincaré map truncated at order $\frac{3}{2}$ (right panel). Excellent agreement between the two methods is evident in the figure. Also, note that the slope of the curve for $\mu > \mu_*$, even though not obvious from the figure, is different than that for $\mu < \mu_*$	50
3.3	Nontrivial eigenvalue as a function of $\mu - \mu_*$ predicted using direct numerical simulation of the original dynamical system (solid line) and the composite Poincaré map truncated at order $\frac{3}{2}$ (dotted). The agreement between the two cases is seen to deviate as $\mu - \mu_* > 0$ increases.	51
3.4	Invariant curve corresponding to the intersection of the trajectories with the Poincaré section $h_{\mathcal{P}} = 0$ for the system given in Eq. (3.15). The discontinuity surface $h_{\mathcal{D}} = 0$ is also shown(dotted line).	54
3.5	Bifurcation diagrams based on the \mathcal{P} Poincaré section obtained under small variations in the deviation $\mu_* - \mu$ using numerical simulation of the original dynamical system (upper-left panel), iteration of the full composite map (2.80) (upper-right panel), reduced composite map (3.22) (lower-left panel), and reduced map with parabolic approximation for Γ near \mathbf{x}_* (3.27) (lower-right panel). Here and in the following graphs, only points of intersection with the corresponding Poincaré section with positive penetration are shown.	55

- 3.6 Bifurcation diagrams based on the \mathcal{P} Poincaré section obtained under variations in the deviation $\mu_* - \mu$ using numerical simulation of the original dynamical system (upper-left panel), and iteration of the full composite map (2.80) (upper-right panel), the reduced composite map (3.22) (lower-left panel) and reduced map with parabolic approximation for Γ near \mathbf{x}_* (3.27) (lower-right panel). These graphs compare the accuracy of the different levels of approximation involved in predicting the impacting dynamics for larger values of $\mu_* - \mu$ than Fig. 3.5. It is to be noticed that in the above graphs the full composite Poincaré map predicts impacting dynamics that match well with numerical simulation of the original dynamical system. 56
- 3.7 Nontrivial Lyapunov exponent corresponding to the impacting motion obtained under variations in the deviation $\mu_* - \mu$ using numerical simulation of the original dynamical system (upper-left panel), and iteration of the full composite map (2.80) (upper-right panel), the reduced composite map (3.22) (lower-left panel) and reduced map with parabolic approximation for Γ near \mathbf{x}_* (3.27) (lower-right panel). Note that for small values of $\mu_* - \mu$ the Lyapunov exponent in all the above graphs oscillates about 0 indicating existence of weakly chaotic and periodic windows (cf. Fig. 3.6). It is also evident that as the approximation level increases the weakly chaotic and periodic window behavior persists for larger values of $\mu_* - \mu$ 57
- 3.8 (Upper panel and blow-ups of regions (a) and (b) in bottom panels) A comparison between the graph of the second iterate of the reduced map (3.22) (solid curve) for $\mu_* - \mu = 5 \times 10^{-5}$ and $\mu_* - \mu = 15 \times 10^{-5}$ and the projection onto the third component of the second iterate of the full composite Poincaré map (2.80) (circles) evaluated for points on the corresponding system attractor. 60

3.9	(Left panel) The difference between $f(x^3)$ and the reduced composite map (3.22) (solid curve) on a neighborhood of x_*^3 compared with an ellipse (dotted) centered at x_*^3 with half-height $f'(x_*) \rho_1$ and half-width ρ_2 , where ρ_1 and ρ_2 are given by (3.28) and (3.29) as predicted by (3.30). Similarly, in the right panel the difference between $f(f(x^3))$ and the second iterate of the reduced map on a neighborhood of x_*^3 is shown. Here, $f'(x_*^3) \approx 5.0164$ and $f'(f(x_*^3)) \approx 0.2013$.	61
3.10	The figure shows the bifurcation diagram based on the \mathcal{P}' Poincaré section using numerical simulation of the original dynamical system (left panel) and the full composite map (2.81) (right panel). The map based on the \mathcal{P}' Poincaré section appears to reproduce the actual bifurcation scenario over a larger interval in $\mu_* - \mu$ than that based on \mathcal{P} .	62
3.11	The intersection of the grazing quasiperiodic system attractor with the \mathcal{P}' section (left panel). Zero-level sets of $h_{\mathcal{D}}$ and $h_{\mathcal{D}'}$ for $\mu_* - \mu \approx 1 \times 10^{-3}$ (right panel).	63
3.12	A comparison between the graph of the third iterate of the reduced map (solid) for $\mu_* - \mu = 5 * 10^{-5}$ and $\mu_* - \mu = 15 * 10^{-5}$ and the projection onto the third component of the third iterate of the full composite Poincaré map (2.81) (circles) evaluated for points on the corresponding system attractor using arc-length parameterization (left panel). Blow-up (right panel) of the boxed part in the left panel.	64
3.13	A comparison between the graph of the third iterate using direct numerical simulation (upper-left panel), full composite mapping (upper-right panel) and the reduced map (lower-left panel) for $\mu_* - \mu = 0.025$ and evaluated for points on the corresponding impacting chaotic system attractor. The corresponding third iterate of the full composite map (lower-right panel) shows the intersection with the identity line (dashed).	65

4.1	Grazing periodic orbits projected on to the $x^1 - x^2$ plane for $m = 0.28$ (left panel) and $m = 0.39$ (right panel) corresponding to the vector field given in Eq. (4.1). In both cases, a projection of the discontinuity surface $h_{\mathcal{D}} = 0$ is also shown in the figure	71
4.2	Bifurcation diagrams showing the penetration $\pi(\mathbf{x})$ as a function of $\mu - \mu_*$ for nonimpacting and impacting motions when $m = 0.28$ obtained using numerical simulations of the original dynamical system (left panel). Right panel compares the unstable impacting orbit obtained using numerical simulation of the original dynamical system (dotted) and the composite Poincaré map (solid). It is evident that the accuracy of the prediction obtained using the composite Poincaré map deteriorates for as $(\mu - \mu_*)$ increases from 0. Here, SN in the left panel denotes a saddle-node bifurcation.	72
4.3	Bifurcation diagrams showing the penetration $\pi(\mathbf{x})$ as a function of $\mu - \mu_*$ for nonimpacting and impacting motions when $m = 0.39$ obtained using numerical simulation of the original dynamical system (left panel) and composite Poincaré map (right panel).	73
4.4	Bifurcation diagrams showing the penetration $\pi(\mathbf{x})$ as a function of $\mu - \mu_*$ for nonimpacting and impacting motions when $m = 0.39$ obtained using numerical simulation of the original dynamical system (left panel) and composite Poincaré map (right panel) for smaller deviations than shown in Fig. 4.3. Here, higher periodic orbits with one impact per period are observed that are not present for larger deviations. Indeed, for much smaller deviations than those presented in this figure, periodic orbits with periodicity > 5 can be obtained.	74

4.5	Left panel - The largest Lyapunov exponent as a function of A . Right panel - Projection of the invariant curve (intersection of the quasiperiodic trajectory with the Poincaré section $h_{\mathcal{P}} = 0$) and the discontinuity surface on to a lower dimensional space. Here, $A = 1.1$ and $\omega = 1.9$	75
4.6	Bifurcation diagram generated using direct numerical integration of the vector field for $A = 1.1$ (left panel) [46] and iterations of composite map obtained using the discontinuity-mapping approach (right panel).	77
4.7	Nontrivial Lyapunov exponent corresponding to the impacting motion for $A = 1.1$ obtained using direct numerical integration of the original dynamical system (left panel) and composite Poincaré map (right panel). These graphs are in good agreement with the bifurcation diagrams shown in Fig. 4.6 i.e., the nontrivial Lyapunov exponent oscillates between positive and negative values corresponding to the periodic and chaotic windows. Note that the positive value obtained by the nontrivial Lyapunov exponent is $\ll 1$ indicating a weakly chaotic behavior.	78
4.8	A comparison between the graph of the first iterate of the reduced map (solid) for $\mu - \mu_* = 15 * 10^{-5}$ and the projection onto the fourth component of the full composite Poincaré map (2.80) (circles) evaluated for points on the corresponding system attractor (left panel). Blow-up (right panel) of the boxed part in the left panel.	79
4.9	Bifurcation diagram obtained under variations in $\mu - \mu_*$ using direct numerical simulation (left panel) for $A = 1.25$. The right panel shows the nontrivial Lyapunov exponent corresponding to the bifurcation behavior in the left panel.	80

4.10	Comparison of the bifurcation behavior obtained under variations in $\mu - \mu_*$ using direct numerical simulation (left panel) and iteration of the full composite map (right panel) for $A = 1.25$. Note that the composite map predicts a diverging response for $\mu - \mu_*$ beyond the right edge of the diagram in qualitative agreement with the disappearance of a local attractor shown in the left panel.	81
4.11	The intersection of the system attractor with \mathcal{P} obtained using the full composite Poincaré map for $A = 1.25$ and $\mu - \mu_* = 2 \times 10^{-5}$. The fractal nature of the chaotic attractor is evident in this figure.	82
4.12	Intersection of the grazing quasiperiodic attractor with \mathcal{P} (left panel) and \mathcal{P}' (right panel) for $A = 1.5$ and $\omega = 4$	83
4.13	Bifurcation diagram generated using direct numerical integration of the vector field for $A = 1.5$ and $\omega = 4$ (left panel) and iterations of full composite map obtained using the discontinuity-mapping approach (right panel).	84
5.1	Mesh intervals corresponding to a solution trajectory. The extended mesh intervals $t_{j-2/3}$ and $t_{j-1/3}$ and the collocation points $z_{j,i}$ are also shown in the figure.	94
5.2	Lagrange basis polynomials corresponding to the mesh $[t_{j-1}, t_j]$	95
5.3	Jacobian corresponding to the linearized boundary value problem of a two-segment hybrid dynamical system. Here, any non-zero entry is represented as a black or a grey dot. Moreover, the black dots correspond to one segment and the grey dots corresponds to the other.	100
5.4	The matrix obtained from the matrix in Fig. 5.3 after a set of parallel operations corresponding to Gauss elimination.	101

5.5	A nonimpacting periodic trajectory of the linear oscillator for $\omega = 2.0$ and $\alpha = 3.0$	111
5.6	Left panel - Diagram indicating the continuation of a nonimpacting periodic trajectory corresponding to the vector field shown in the Eq. (5.56). Here, $\widehat{\text{TC}}$ detects the parameter value corresponding to a grazing incidence with the event surface $h_1 = 0$ that can be used as a starting solution to obtain a grazing curve. Right panel - Grazing curve in the $(\alpha - \omega)$ space obtained using $\widehat{\text{TC}}$. The o 's on the grazing curve correspond to the co-dimension-two bifurcation points $\xi_1 = 0$	112
5.7	Left panel - Bifurcation diagram indicating the continuation of an impacting periodic orbit as a function of α with a grazing periodic orbit as a starting solution, for $\omega = 2.0072$ and $\alpha = 3.0357$. This impacting periodic trajectory experiences a period-doubling bifurcation at $\alpha = 3.0364$ resulting in a stable impacting trajectory. Right panel - Impacting periodic trajectories corresponding to the grazing incidence (a) and period-doubling bifurcation (b) points from the left panel.	113
5.8	Left panel - Bifurcation diagram indicating the continuation of an impacting periodic trajectory as a function of α with a grazing periodic trajectory as a starting solution, for $\omega = 1.8901$ and $\alpha = 2.5797$. This impacting periodic trajectory experiences a saddle-node bifurcation at $\alpha = 1.9713$ resulting in a stable impacting trajectory. Right panel - Impacting periodic trajectories corresponding to the grazing incidence (a) and saddle-node bifurcation points (b) from the left panel.	114

5.9	Left panel - Diagram depicting the two parameter continuation of grazing trajectories, saddle-node bifurcation points and period-doubling points correspond to impacting periodic trajectories. As mentioned previously, the saddle-node and period-doubling curves intersect the grazing curve tangentially at the co-dimension-two bifurcation point corresponding to $\xi_1 = 0$	115
5.10	Valid solution to the boundary value problem with no physical significance. .	116
5.11	A nonimpacting periodic trajectory of the nonlinear mems oscillator for $\omega = 0.8$, and $V = 0.5641$	116
5.12	Grazing curve in the $(V - \omega)$ space obtained using $\widehat{\text{TC}}$ for the given nonlinear MEMS oscillator. The σ 's on the grazing curve correspond to the co-dimension-two bifurcation points $\xi_n = 0$	117
5.13	Left panel shows the bifurcation diagram corresponding to a one parameter continuation of a two-segment periodic trajectory for $\omega = 0.8$. The locus of saddle-node, period-doubling and secondary grazing bifurcations is also shown in the figure. Here, segment-1 of the two-segment periodic orbit undergoes a secondary grazing incidence with the event surface $h_{\text{front}} = 0$. A few examples of the two-segment periodic trajectories are depicted in the right panel. The dotted trajectory in the right panel indicates the periodic trajectory undergoing a secondary grazing incidence.	118
5.14	This figure presents the two parameter continuation of grazing, saddle-node and period-doubling bifurcation points corresponding to an impacting periodic trajectory. As mentioned previously, the intersection of the grazing curve and the saddle-node and period-doubling curves occur at co-dimension-two bifurcation points corresponding to $\xi_1 = 0$	119

5.15	Illustration of a procedure to create a starting solution for the continuation of a grazing trajectory of a hybrid dynamical system through $(0.7469, 0.8)$. The trajectory shown here is same as the dotted trajectory in Fig. 5.13.	120
5.16	The grazing curve corresponding to the MEMS oscillator obtained through the grazing point $(0.7469, 0.8)$	120
5.17	Left panel presents the bifurcation diagram corresponding to $m = 0.28$ where $\mu_* \approx -0.7981$. Here, an unstable impacting orbit is born in the immediate vicinity of the grazing periodic trajectory that undergoes a saddle-node bifurcation. On the contrary, the right panel shows a bifurcation diagram corresponding to $m = 0.39$ where an unstable orbit is born for μ greater than μ_* . This unstable orbit undergoes a period-doubling bifurcation to give rise to a stable impacting orbit.	121
5.18	Left panel shows the bifurcation diagram corresponding to $A = 1.25$, $\omega = 1.9$, and $\mu_* \approx -0.4940$. Here, a stable period-2 impacting orbit with one impact per period is continued as a function of the parameter μ along with the locus of the saddle-node bifurcation. Right panel shows the impacting periodic trajectories corresponding to two points of the bifurcation diagram on the left.	121

List of Tables

2.1 Lyapunov Exponents for a variety of orbitally asymptotically stable steady-state trajectories [37].	39
---	----

Chapter 1

Introduction

1.1 Motivation

Our unsatiating thirst to decipher the complexity of the world in which we live and its surroundings has resulted in the development of science. Most of the natural phenomena such as motion of the planets, flow of fluids etc., are *dynamic* processes i.e., they bring a *change with time*. The field of *Mechanics* is a result of thousands of years of insight into such processes. However, in the past four hundred years, Mechanics has taken a very rigorous mathematical form mostly due to the invention of calculus. This presented the world with a powerful tool that can predict the outcome of such processes in future time with certain accuracy. While the theory of Mechanics has been very well developed for processes with smooth transition in time from one state to the other, it is relatively unexplored in the case of systems that undergo a discontinuous change with time in terms of certain quantities that define their transition. Such cases occur very frequently in man-made mechanical systems and the emphasis of this dissertation is to study their dynamic behavior under changes in system parameters.

Many physical phenomena involving a sequence of dramatic and sudden changes in their

related quantities are typically studied using mathematical models containing some type of discontinuity in the rules governing their motion. Such systems, called *nonsmooth systems* or *hybrid dynamical systems*, appear very frequently in engineering applications. For example, the behavior of diodes and transistors in electrical circuits, control mechanisms involving switching, collisions between components in a variety of mechanical systems, friction-induced vibrations in machine tool chattering, squealing noise of rail wheels and torsional vibrations in oilwell drillstrings have been topics of research in the area of nonsmooth systems.

Even though some of the nonsmooth models can be approximated by smooth models and standard numerical integration schemes can be used to study them, the procedure is not free of disadvantages. One of the main disadvantages is that the ordinary differential equations that govern the motion resulting from smoothening are typically stiff and computationally very expensive to solve. This is because their numerical integration involves a mandatory reduction in the step sizes to very small numbers. Moreover, smoothening of vector fields in nonsmooth models eliminates the possibility of applying some of the analytical tools that would otherwise provide conceptual insights into the behavior of these systems.

The mathematical modeling of nonsmooth dynamical systems involve ordinary differential equations with discontinuous right hand sides. Depending on the type of discontinuity, these systems are categorized as follows [27]:

1. Systems in which the vector fields are continuous at a discontinuity boundary but their Jacobian is discontinuous i.e., systems with continuous but nonsmooth vector fields. Systems with purely elastic one-sided supports fall into this category.
2. Systems in which the vector fields governing the motion are discontinuous at a discontinuity boundary, called *Filippov systems*. Systems involving dry friction and viscoelastic supports fall into this category.
3. Systems involving jumps in state space resulting from impacts between various system components in a mechanical system. Impact microactuators and gear rattle are a few

examples of systems with jumps. These are also called *impact oscillators*.

This dissertation (Chapters 3 & 4) mainly deals with the qualitative changes in a variety of impact oscillators under parameter variations. Therefore, the following section is exclusively dedicated to the introduction and literature review on impact oscillators. However, the software program (Chapter 5) developed as a part of this dissertation can be used to study bifurcation analysis of general class of hybrid dynamical systems. A detailed mathematical formulation of hybrid dynamical systems that also includes impact oscillators is presented in the next chapter.

1.2 Impact Oscillators

Impacts in oscillating mechanical systems are generally caused either by interaction between system components or by their collisions with rigid obstacles. Such mechanical systems occur very frequently in engineering applications. Vibrations of helicopter rotor blades, impact microactuators, mechanical devices with loose fitting joints, gear rattle, buildings under earthquake excitation, tubes vibrating within a fluid, print hammers, dynamic behavior of off-shore equipment etc. are a few examples of impact oscillators (see also [2, 3, 15, 17, 18] for more examples).

Impacts can have detrimental effects on the desired motion of a system and contribute significantly to its wear and tear. However, in few cases such as microactuators and Braille printers, impacts are exploited for precise positioning and printing for blind, respectively. Hence, this prevalent occurrence and influence of impacts in technological situations demand a thorough investigation of dynamic behavior of impact oscillators under diverse conditions.

Fig. 1.1 shows a simple single-degree-of-freedom impact oscillator in which the motion of the mass is confined by a rigid wall at $x = d$, where x and \dot{x} are the position and velocity of the mass at any point in time. While the motion of the mass is considered smooth as

long as $x < d$, an impact occurs when $x = d$ and $\dot{x} \neq 0$. In most of the engineering applications where there is an energy loss due to impacts, the rebound velocity of the mass can be modeled using *coefficient of restitution*. Also, the time scale involved during impact is orders of magnitude less than the time scale of the regular motion. This facilitates modeling of impact as an instantaneous jump in the velocity. As most of the previous work suggests the coefficient of restitution model serves as an accurate modeling technique in the case of impact oscillators under the assumption that the time of impact is negligible.

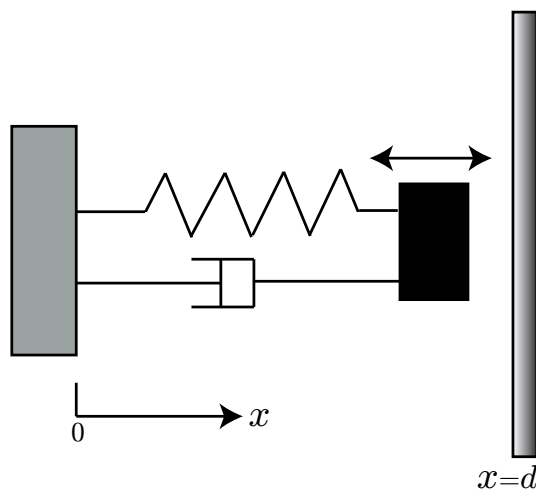


Figure 1.1: Schematic of an impact oscillator.

A transition from nonimpacting to impacting motion in an impact oscillator occurs via a zero-normal-velocity contact with a boundary, called a *grazing contact*, and the corresponding changes in its behavior are called *grazing bifurcations* [5, 6, 7, 9, 17, 20, 27, 33, 34, 35, 40, 45, 52, 53]. Fig. 1.2 shows the state space representation of a nonimpacting and a grazing trajectory along with a discontinuity surface. Here, a nonimpacting trajectory corresponds to the motion of the oscillator when its steady state motion does not interact with the constraint. Similarly, a grazing trajectory corresponds to the motion of the oscillator when its steady state motion attains a grazing contact with the constraint. A discontinuity surface is a co-dimension-one surface in state space representing the motion constraint, and its intersection with a grazing trajectory is termed as a grazing point.

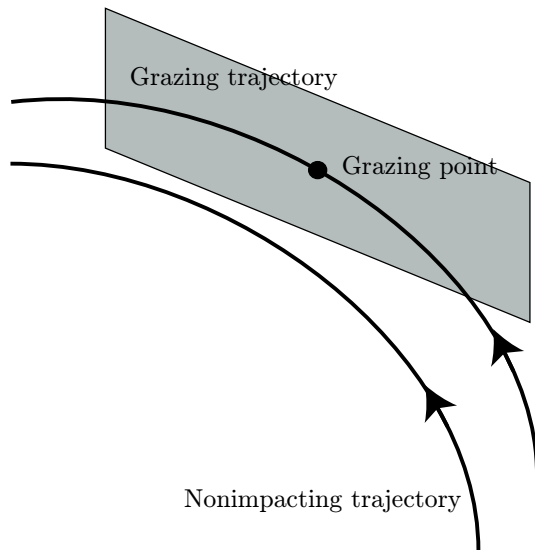


Figure 1.2: A schematic diagram showing nonimpacting and grazing orbits along with the corresponding discontinuity surface.

Grazing bifurcations are typically associated with instabilities that lead to the transition to motions with impact velocities bounded from below for values of the system parameters arbitrarily close to those at grazing, a phenomenon that is undesirable in many engineering systems. Moreover, the repulsion from the vicinity of the pre-grazing nonimpacting steady state response to a different oscillatory behavior is very rapid and without any prior indication when compared to similar bifurcations in systems without discontinuities (smooth dynamical systems). These instabilities transform the nonimpacting motion into an impacting one involving high-velocity impacts that may cause significant damage to the components and eventually lead to the failure of the mechanical system. A grazing bifurcation is called *continuous* if the impacting dynamics after the grazing contact remain in the vicinity of the original steady state motion corresponding to the grazing trajectory. It is referred as *discontinuous grazing bifurcation* otherwise.

Previously, numerical studies have reported a variety of bifurcations in impact oscillators that are typically not observed in smooth dynamical systems. Thompson & Ghaffari [42] and Thompson [43] are among the earliest researchers on impact oscillators. They

demonstrated that the dynamic behavior of impact oscillators contains an infinite sequence of period-doubling bifurcations resulting in chaos that is in quantitative agreement with the Feigenbaum scenario [16]. This study essentially focused on modeling mooring towers of offshore equipment in marine engineering. Shaw & Holmes [39] explored the impacting dynamic behavior of a periodically forced linear oscillator with a constraint. They not only confirmed the findings of Thompson & Ghaffari [42] but also modeled impacting dynamics using a discontinuous map which was shown to undergo period-doubling bifurcations followed by a complex sequence of transitions that contained long superstable periodic motions.

Foale & Bishop [19] and Foale [17] reported that the introduction of a nonlinearity into a linear oscillator in the form of an instantaneous impact rule can result in a highly complicated behavior. They attributed the radical changes in the dynamic behavior of an impact oscillator to the discontinuity in the derivative of the corresponding Poincaré map (see also Whiston [48] for detailed work on singularities in impact oscillators). Their work also demonstrated two distinct types of grazing bifurcations that are connected via a codimension-two grazing bifurcation. This characteristic of grazing bifurcations is explained with more rigor and in general class of single degree-of-freedom systems in later publications [7, 45]. In their later studies Foale & Bishop [18], using numerical techniques, suggested that grazing bifurcations are the limiting cases of typical bifurcations that are encountered in smooth dynamical systems as the impact is hardened.

Budd & Dux [3, 4] analyzed a single degree-of-freedom, periodically forced, impact oscillator when the forcing frequency is twice its natural frequency. This facilitated asymptotic estimates of the intermittent chaotic behavior that were later compared with numerical simulations. They reported that a grazing bifurcation can lead to an intermittent chaotic behavior with low velocity impacts that is followed by an irregular sequence of high velocity impacts. They also analyzed a discontinuous one-dimensional map in order to explain the existence of periodic windows in which the period of impacting solutions increases monotonically from one window to the other. Nusse *et al.* [36] reported similar bifurcation phenomenon categorized as *border-collision bifurcations*, where a fixed point of a piecewise smooth map crosses

a codimension-one discontinuity surface in state space with a change in a system parameter. They studied two-dimensional piecewise smooth maps corresponding to a variety of physical models in order to demonstrate the above discussed phenomenon.

On the experimental side of the literature on impact oscillators, Shaw [40] reported some of the earliest results on the dynamic behavior of a harmonically forced beam with one-sided amplitude constraint. He reported experimentally found complicated behavior such as multiple subharmonic resonances and period doubling sequence to chaos. The work also successfully compared the experimental results with an analytical model obtained via single mode approximation for the oscillations of the beam. Moore & Shaw [29] studied impacting dynamics of a harmonically excited pendulum. Both normal as well as inverted pendula with rigid barriers that limited the maximum amplitude from their equilibrium positions were tested. They demonstrated that in the case of the inverted pendulum, for fixed frequency and excitation amplitude, ten distinct steady-state impacting solutions exist merely by changing the initial conditions. However, the normal pendulum behaved differently for the same set of parameters. They reported that in the case of the normal pendulum impacting steady state dynamics coexist with nonimpacting steady state motion predicted from linear theory. Bishop [2] also reported qualitatively similar experimental results of an impacting beam driven near its linear resonant frequency.

Bayly & Virgin [1] performed experiments on a periodically forced, fully nonlinear impacting pendulum. In their study the amplitude of the pendulum was not constrained to small angles unlike earlier works along the same lines (Moore & Shaw [29]). They reported a variety of periodic as well as chaotic motions of the impacting pendulum that were in good agreement with numerical simulations performed in the same work. Todd & Virgin [47] studied an experimental track-cart system to demonstrate the chaotic responses between windows of periodic behavior. They also showed that the chaotic dynamics are marked by finger-like attractors in which the number of such fingers is governed by the periodicity of the previous periodic window.

The study of impact oscillators was mostly confined to numerical and experimental investigations until Nordmark [35] introduced the concept of *discontinuity mappings* (cf. [7, 46, 52, 53]) that became a powerful analytical tool to analyze these systems in the vicinity of a grazing trajectory. This methodology approximates the near-grazing impacting dynamics using a discrete dynamical system obtained solely from the conditions at the grazing contact. This discrete system can easily be simulated on a computer. This approach not only eliminates the computationally expensive task of numerically integrating the differential equations governing the motion, but also allows one to perform a local stability analysis of the impacting system near the grazing point. A rigorous mathematical formulation of the discontinuity-mapping approach is presented in Chapter 2.

In the recent past, the discontinuity-mapping approach has been successfully used to analyze the grazing bifurcations of periodic orbits and the results were found to be in excellent agreement with direct numerical simulations of the differential equations governing the impacting system. Based on this approach, Fredriksson & Nordmark [20] formulated a criterion to determine the persistence of near-grazing impacting motion following a grazing contact. Later, Dankowicz & Jerrelind [8] successfully used this criterion to develop an algorithm to control the types of bifurcations that occur at a grazing contact. Again, in the implementation of the control strategy, the discontinuity-mapping approach and numerical simulations were in good agreement.

While grazing bifurcations of periodic orbits have been documented extensively in the literature and are relatively well understood, discontinuity-induced bifurcations of quasiperiodic system attractors due to grazing contact remain largely unexplored. The first discussion of the near-grazing dynamics of a quasiperiodic attractor can be found in Nordmark [34], which contains numerical simulations of the post-grazing impacting dynamics of an originally two-frequency quasiperiodic oscillation in a three-dimensional state space. The system explored by Nordmark was later revisited by Dankowicz *et al.* [9, 10], in which a heuristic and restrictive algorithm based on the fundamental construction underlying discontinuity mappings was employed to predict the near-grazing bifurcation behavior. This analysis was

put on a more solid foundation through the work of Thota & Dankowicz [44, 46], in which the correction to the smooth flow due to near-grazing impacts was derived without any assumptions on the post-grazing dynamics (cf. Chapters 3 and 4 of this dissertation). In particular, it was argued that the dramatic loss of a local attractor that occurs commonly in the case of grazing bifurcations of periodic system attractors [52, 53] would not occur in the case of co-dimension-one quasiperiodic attractors and would be unlikely in the case of higher co-dimension attractors.

Impacting dynamics of quasiperiodic attractors have also been studied in the non-grazing context, for example, in the work by Xie & Ding [49], where a Hopf bifurcation of an impacting periodic attractor to an impacting quasiperiodic attractor are discussed. In contrast to the work by Xie & Ding [49], this dissertation emphasizes those bifurcations that depend directly on the discontinuous nature of the vector field and would not be expected in a smooth system. In particular, the work by Thota & Dankowicz [44, 46] constitute the first documented analytical study of discontinuity-induced bifurcations of co-dimension-two quasiperiodic system attractors.

The accuracy of the discontinuity-mapping approach in predicting the impacting dynamics in the vicinity of a grazing trajectory is strongly established in the abovementioned work. This dissertation will use the complete form of the approach to quasiperiodic motions and will hence extend its validity to a general class of dynamical systems.

1.3 Research Objectives

The objectives of this dissertation are to

1. Numerically and analytically investigate grazing bifurcations of co-dimension-one and -two invariant tori. The study includes understanding the changes in the stability characteristics of the system response due to grazing bifurcations and predicting the

impacting dynamics based on the conditions at the grazing contact in periodic and quasiperiodic cases.

2. Integrate the knowledge from the analytical and numerical study to develop a computational toolbox that predicts and characterizes grazing bifurcations. The toolbox developed will have the ability to perform bifurcation analysis of hybrid dynamical systems similar to the performance of AUTO 97 [13, 14] for smooth dynamical systems.

1.4 Synopsis

This dissertation is organized as follows.

Chapter 2 introduces the concept of hybrid dynamical systems, their mathematical formulation and the dynamical systems' concepts necessary in the analysis of bifurcations that occur in such systems. A detailed description of quasiperiodic oscillations, co-dimension-two bifurcations specific to impact oscillators and the calculation of Lyapunov exponents for continuous and discrete dynamical systems is presented. The discontinuity-mapping approach, a powerful technique that can be used in the local analysis of grazing bifurcations, is presented here along with its mathematical formulation. Conceptual insights to obtain local approximations of the functions involved in the discontinuity-mapping approach are provided.

Chapter 3 illustrates grazing bifurcations of co-dimension-one invariant tori. Two piecewise smooth example dynamical systems, a periodic orbit in a two-dimensional state space and a two-frequency quasiperiodic orbit in a three-dimensional state space are studied using both the discontinuity-mapping approach and direct numerical integration. The effect of the square-root term, the lowest order term in the description of the impacting dynamics, on the types of grazing bifurcations is studied. In the quasiperiodic case, a reduced formulation of the impacting dynamics is employed to analyze grazing bifurcations and the results are compared with the ones obtained using the full discontinuity mapping.

Chapter 4 reports grazing bifurcations of co-dimension-two invariant tori. Two piecewise smooth example dynamical systems, a periodic orbit in a three-dimensional state space and a two-frequency quasiperiodic orbit in a four-dimensional state space are studied using both the discontinuity-mapping approach and direct numerical integration. Here, it is noticed that the discontinuity-mapping approach is able to characterize the post-grazing asymptotic dynamics only in the case that the dynamics remain in the vicinity of the grazing trajectory. When this is not the case, the discontinuity-mapping approach is nevertheless able to predict the initial transient dynamics away from the vicinity of the grazing trajectory. Again, the above systems are studied from the perspective of the loss of the local attractor after the grazing contact. The reduced formulation of the impacting dynamics is also used to study grazing bifurcations of the two-frequency quasiperiodic orbit in the four-dimensional state space.

Chapter 5 describes the continuation toolbox $\widehat{\text{TC}}$. The tools required in the continuation process such as pseudo-arclength continuation and orthogonal collocation methods using piecewise polynomials are discussed in detail. The chapter also discusses the methodology involved in solving a Boundary Value Problem (BVP) in differential equations using collocation methods. The capabilities, basic structure and problem types of $\widehat{\text{TC}}$ are discussed using illustrations. It also presents the methodology required to compute the correct eigenvalues of periodic orbits in hybrid dynamical systems. Four piecewise-smooth dynamical systems are studied using $\widehat{\text{TC}}$ and diagrams indicating grazing bifurcations and their effects on the overall dynamics are reported.

Chapter 6 concludes the dissertation with a summary of the results obtained. Also, recommendations for future work that would enable a better understanding of grazing bifurcations of co-dimension-two or higher quasiperiodic system attractors are stated.

Chapter 2

Dynamical Systems - Concepts and Theory

Notation: The notation followed in this dissertation is as follows. Normal-faced characters, such as h and t are used to denote scalar-valued quantities. Subscripts used in conjunction with normal-faced characters, such as $h_{\mathcal{D}}$ are used to distinguish different scalar-valued quantities. Bold-faced characters, such as \mathbf{x} and \mathbf{f} are used to denote vector-valued quantities. Subscripts used in conjunction with bold-faced characters, such as \mathbf{x}_1 are used to distinguish different vectors. Superscripts used in conjunction with normal-faced characters whose bold-faced equivalents denote vectors, such as x^1 are used to denote coordinates of the corresponding vector-valued quantities. Calligraphic font type, as in \mathcal{D} and \mathcal{P} , is used to denote hypersurfaces in state space. Finally, subscripts of scalar- or vector-valued quantities preceded by a comma such as $\mathbf{f}_{,\mathbf{x}}$ are used to denote differentiation with respect to the quantity in the subscript.

2.1 Smooth Dynamical Systems

The simplest description of a continuous-in-time dynamical system relies on the introduction of a *state space* X of dimension n and an associated vector-valued function $\mathbf{f} : X \rightarrow X$ known as the *vector field*, such that \mathbf{f} is *tangential* to one-parameter curves in X corresponding to the time-evolution of the state of the dynamical system. For example, given a vector field $\mathbf{f} : \mathbb{R}^n \rightarrow \mathbb{R}^n$, this relationship to the time-evolution of the state vector $\mathbf{x} \in \mathbb{R}^n$ is described by the differential equation

$$\frac{d\mathbf{x}}{dt} = \mathbf{f}(\mathbf{x}). \quad (2.1)$$

A *solution* to the corresponding dynamical system is a curve $\mathbf{x} : \mathbb{R} \rightarrow \mathbb{R}^n$ (often called a *trajectory*) such that the corresponding tangent vector at $\mathbf{x}(t)$ (where t denotes *time*) is given by $\mathbf{f}(\mathbf{x}(t))$. If $\mathbf{x}(t_0) = \mathbf{x}_0$ is given, \mathbf{x}_0 is referred to as an *initial condition*.

The existence and uniqueness of the solution to a dynamical system for a given initial condition depends on the differentiability of the vector field \mathbf{f} .

Theorem 2.1.1 (Existence and Uniqueness Theorem) *Suppose that $\mathbf{f} : \mathbb{R}^n \rightarrow \mathbb{R}^n$ is C^1 on an open neighborhood of a point $\mathbf{x}_0 \in \mathbb{R}^n$. Then, the initial-value problem*

$$\frac{d\mathbf{x}}{dt} = \mathbf{f}(\mathbf{x}) \quad (2.2)$$

$$\mathbf{x}(t_0) = \mathbf{x}_0 \quad (2.3)$$

has a unique solution on some time interval containing t_0 [22, 41].

More generally, given sufficient smoothness of the vector field, there exists an equally smooth vector-valued function $\Phi(\mathbf{x}, t)$ called the *flow function*, such that

$$\Phi(\mathbf{x}, 0) = \mathbf{x} \quad (2.4)$$

and

$$\frac{\partial}{\partial t} \Phi(\mathbf{x}, t) = \mathbf{f}(\Phi(\mathbf{x}, t)). \quad (2.5)$$

Here, $\Phi(\mathbf{x}_0, t - t_0)$ maps an initial condition \mathbf{x}_0 at time t_0 on some trajectory to the corresponding point at time t . It follows that

$$\Phi(\mathbf{x}, t + s) = \Phi(\Phi(\mathbf{x}, s), t). \quad (2.6)$$

Typically, closed form expressions for $\Phi(\mathbf{x}, t)$ can only be obtained for very simple examples of \mathbf{f} . There is rarely, therefore, a substitute for numerical simulation in investigating the general properties of a dynamical system. In special cases, however, analysis combined with limited computation may be able to make significant and useful predictions regarding a subset of properties of a given dynamical system. For example, consider a trajectory segment based at a point \mathbf{x}_0 at $t = t_0$ for $t \in [t_0, t_0 + T]$. Then, by the smoothness of the flow function,

$$\Phi(\mathbf{x}_0 + \delta\mathbf{x}, T) \approx \Phi(\mathbf{x}_0, T) + \Phi_{,\mathbf{x}}(\mathbf{x}_0, T) \cdot \delta\mathbf{x}, \quad (2.7)$$

i.e., to lowest order, the sensitivity of the final state after elapsed time T to changes in the initial state are captured by the linear map with matrix representation $\Phi_{,\mathbf{x}}(\mathbf{x}_0, T)$ known as the *Jacobian* of the flow function.

Differentiating Eq. (2.5) with respect to \mathbf{x} and interchanging the partial derivatives on the left-hand side yields

$$\frac{\partial}{\partial t} \Phi_{,\mathbf{x}}(\mathbf{x}, t) = \mathbf{f}_{,\mathbf{x}}(\Phi(\mathbf{x}, t)) \cdot \Phi_{,\mathbf{x}}(\mathbf{x}, t) \quad (2.8)$$

known as the *first variational equation* corresponding to the given dynamical system. Moreover, from Eq. (2.4) it follows that

$$\Phi_{,\mathbf{x}}(\mathbf{x}, 0) = Id, \quad (2.9)$$

where Id denotes the $n \times n$ identity matrix.

From Eq. (2.7) it follows that, to lowest order, $\Phi_{,\mathbf{x}}(\mathbf{x}_0, T)$ maps deviations in the initial state to deviations in the final state. In particular, differentiation of Eq. (2.6) with respect to s yields

$$\mathbf{f}(\Phi(\mathbf{x}, t + s)) = \Phi_{,\mathbf{x}}(\Phi(\mathbf{x}, s), t) \cdot \mathbf{f}(\Phi(\mathbf{x}, s)) \quad (2.10)$$

or, for $s = 0$,

$$\mathbf{f}(\Phi(\mathbf{x}, t)) = \Phi_{,\mathbf{x}}(\mathbf{x}, t) \cdot \mathbf{f}(\mathbf{x}), \quad (2.11)$$

i.e., the vector field is invariant under the application of $\Phi_{,\mathbf{x}}(\mathbf{x}, t)$.

2.2 Hybrid Dynamical Systems

In this dissertation, a *hybrid dynamical system* assumes the existence of a state space X of dimension n and an associated vector-valued function $\mathbf{f}_{\mathbf{I}} : X \rightarrow X$ known as the *vector field*, parameterized by an *index vector* \mathbf{I} in some finite set \mathbb{F} . To each value of the index vector \mathbf{I} associate a smooth *event function* $h_{\mathbf{I}} : X \rightarrow \mathbb{R}$ and a smooth *state jump function* $\mathbf{g}_{\mathbf{I}} : X \rightarrow X$. Then, a *solution* to the corresponding dynamical system is a sequence $\{\mathbf{x}_j : (t_{j-1}, t_j] \rightarrow X\}_{j=1}^m$ of m smooth curves and an associated sequence $\{\mathbf{I}_j\}_{j=1}^m$, such that

$$\mathbf{I}(t) = \mathbf{I}_j, t \in (t_{j-1}, t_j] \quad (2.12)$$

and

1. The corresponding tangent vector at $\mathbf{x}_j(t)$ equals $\mathbf{f}_{\mathbf{I}_j}(\mathbf{x}_j(t))$, i.e., in the case of $X = \mathbb{R}^n$

$$\frac{d}{dt}\mathbf{x}_j(t) = \mathbf{f}_{\mathbf{I}_j}(\mathbf{x}_j(t)). \quad (2.13)$$

2. The j -th segment terminates at an intersection with the *event surface*

$$\{\mathbf{x} \mid h_{\mathbf{I}_j}(\mathbf{x}) = 0, h_{\mathbf{I}_j, \mathbf{x}}(\mathbf{x}) \cdot \mathbf{f}_{\mathbf{I}_j}(\mathbf{x}) \leq 0\}, \quad (2.14)$$

i.e.,

$$h_{\mathbf{I}_j}(\mathbf{x}_j(t_j)) = 0. \quad (2.15)$$

3. The *connectivity* between the j -th and $j + 1$ -th segments is given by the function $\mathbf{g}_{\mathbf{I}_j}$,

i.e.,

$$\mathbf{g}_{\mathbf{I}_j}(\mathbf{x}_j(t_j)) = \lim_{t \rightarrow t_{j+}^-} \mathbf{x}_{j+1}(t). \quad (2.16)$$

The sequence $\Sigma = \{\mathbf{I}_j\}_{j=1}^m$ of values of the index vector is called the solution's *signature*. Here, we allow for the possibility of infinite solution sequences and the replacement of m by ∞ .

The terminal point $\mathbf{x}_j(t_j)$ on the j -th solution segment is a *transversal event* if

$$h_{\mathbf{I}_j, \mathbf{x}}(\mathbf{x}_j(t_j)) \cdot \mathbf{f}_{\mathbf{I}_j}(\mathbf{x}_j(t_j)) < 0. \quad (2.17)$$

Consider the function

$$F(\mathbf{x}, t) = h_{\mathbf{I}_j}(\Phi_{\mathbf{I}_j}(\mathbf{x}, t)), \quad (2.18)$$

where

$$F\left(\lim_{t \rightarrow t_{j-1}^+} \mathbf{x}_j(t), t_j - t_{j-1}\right) = h_{\mathbf{I}_j}(\mathbf{x}_j(t_j)) = 0 \quad (2.19)$$

and

$$F_t\left(\lim_{t \rightarrow t_{j-1}^+} \mathbf{x}_j(t), t_j - t_{j-1}\right) = h_{\mathbf{I}_j, \mathbf{x}}(\mathbf{x}_j(t_j)) \cdot \mathbf{f}_{\mathbf{I}_j}(\mathbf{x}_j(t_j)) < 0. \quad (2.20)$$

From the implicit function theorem it follows that there exists a unique smooth function $\tau_{\mathbf{I}_j}(\mathbf{x})$ for $\mathbf{x} \approx \lim_{t \rightarrow t_{j-1}^+} \mathbf{x}_j(t)$, where

$$\tau_{\mathbf{I}_j}\left(\lim_{t \rightarrow t_{j-1}^+} \mathbf{x}_j(t)\right) = t_j - t_{j-1}, \quad (2.21)$$

and such that

$$h_{\mathbf{I}_j}(\Phi_{\mathbf{I}_j}(\mathbf{x}, \tau_{\mathbf{I}_j}(\mathbf{x}))) \equiv 0, \quad (2.22)$$

and

$$\tau_{\mathbf{I}_j, \mathbf{x}}\left(\lim_{t \rightarrow t_{j-1}^+} \mathbf{x}_j(t)\right) = -\frac{h_{\mathbf{I}_j, \mathbf{x}}(\mathbf{x}_j(t_j))}{h_{\mathbf{I}_j, \mathbf{x}}(\mathbf{x}_j(t_j)) \cdot \mathbf{f}_{\mathbf{I}_j}(\mathbf{x}_j(t_j))} \cdot \Phi_{\mathbf{I}_j, \mathbf{x}}\left(\lim_{t \rightarrow t_{j-1}^+} \mathbf{x}_j(t), t_j - t_{j-1}\right). \quad (2.23)$$

Let

$$\mathbf{P}_{\mathbf{I}_j}(\mathbf{x}) = \Phi_{\mathbf{I}_j}(\mathbf{x}, \tau_{\mathbf{I}_j}(\mathbf{x})) \quad (2.24)$$

for $\mathbf{x} \approx \lim_{t \rightarrow t_{j-1}^+} \mathbf{x}_j(t)$. Then,

$$\mathbf{P}_{\mathbf{I}_j, \mathbf{x}}\left(\lim_{t \rightarrow t_{j-1}^+} \mathbf{x}_j(t)\right) \quad (2.25)$$

$$= \left(Id - \frac{\mathbf{f}_{\mathbf{I}_j}(\mathbf{x}_j(t_j)) \cdot h_{\mathbf{I}_j, \mathbf{x}}(\mathbf{x}_j(t_j))}{h_{\mathbf{I}_j, \mathbf{x}}(\mathbf{x}_j(t_j)) \cdot \mathbf{f}_{\mathbf{I}_j}(\mathbf{x}_j(t_j))} \right) \cdot \Phi_{\mathbf{I}_j, \mathbf{x}}\left(\lim_{t \rightarrow t_{j-1}^+} \mathbf{x}_j(t), t_j - t_{j-1}\right). \quad (2.26)$$

Given a solution based at $\mathbf{x}_1(t_0)$ and the corresponding signature $\Sigma = \{\mathbf{I}_j\}_{j=1}^m$, define the *hybrid flow map* \mathbf{P}_Σ for $\mathbf{x} \approx \mathbf{x}_1(t_0)$ by the expression

$$\mathbf{P}_\Sigma(\mathbf{x}) = \mathbf{P}_{\mathbf{I}_m} \circ \mathbf{g}_{\mathbf{I}_{m-1}} \circ \mathbf{P}_{\mathbf{I}_{m-1}} \circ \cdots \circ \mathbf{g}_{\mathbf{I}_1} \circ \mathbf{P}_{\mathbf{I}_1}(\mathbf{x}). \quad (2.27)$$

In particular,

$$\begin{aligned} \mathbf{P}_{\Sigma, \mathbf{x}} \left(\lim_{t \rightarrow t_0^+} \mathbf{x}_1(t) \right) &= \mathbf{P}_{\mathbf{I}_m, \mathbf{x}} \left(\lim_{t \rightarrow t_{m-1}^+} \mathbf{x}_m(t) \right) \cdot \mathbf{g}_{\mathbf{I}_{m-1}, \mathbf{x}}(\mathbf{x}_{m-1}(t_{m-1})) \\ &\quad \cdot \mathbf{P}_{\mathbf{I}_{m-1}, \mathbf{x}} \left(\lim_{t \rightarrow t_{m-2}^+} \mathbf{x}_{m-1}(t) \right) \cdots \cdots \mathbf{g}_{\mathbf{I}_1, \mathbf{x}}(\mathbf{x}_1(t_1)) \cdot \mathbf{P}_{\mathbf{I}_1, \mathbf{x}} \left(\lim_{t \rightarrow t_0^+} \mathbf{x}_1(t) \right) \end{aligned} \quad (2.28)$$

describes the sensitivity of the terminating point on the final segment to perturbations in the initial condition. From Eq. (2.11) it follows that

$$\begin{aligned} &\mathbf{P}_{\mathbf{I}_j, \mathbf{x}} \left(\lim_{t \rightarrow t_{j-1}^+} \mathbf{x}_j(t) \right) \cdot \mathbf{f}_{\mathbf{I}_j} \left(\lim_{t \rightarrow t_{j-1}^+} \mathbf{x}_j(t) \right) \\ &= \left(Id - \frac{\mathbf{f}_{\mathbf{I}_j}(\mathbf{x}_j(t_j)) \cdot h_{\mathbf{I}_j, \mathbf{x}}(\mathbf{x}_j(t_j))}{h_{\mathbf{I}_j, \mathbf{x}}(\mathbf{x}_j(t_j)) \cdot \mathbf{f}_{\mathbf{I}_j}(\mathbf{x}_j(t_j))} \right) \cdot \Phi_{\mathbf{I}_j, \mathbf{x}} \left(\lim_{t \rightarrow t_{j-1}^+} \mathbf{x}_j(t), t_j - t_{j-1} \right) \cdot \mathbf{f}_{\mathbf{I}_j} \left(\lim_{t \rightarrow t_{j-1}^+} \mathbf{x}_j(t) \right) \\ &= \left(Id - \frac{\mathbf{f}_{\mathbf{I}_j}(\mathbf{x}_j(t_j)) \cdot h_{\mathbf{I}_j, \mathbf{x}}(\mathbf{x}_j(t_j))}{h_{\mathbf{I}_j, \mathbf{x}}(\mathbf{x}_j(t_j)) \cdot \mathbf{f}_{\mathbf{I}_j}(\mathbf{x}_j(t_j))} \right) \cdot \mathbf{f}_{\mathbf{I}_j}(\mathbf{x}_j(t_j)) \\ &= \mathbf{0}, \end{aligned} \quad (2.29)$$

i.e., to lowest order, deviations in the initial condition along the initial vector field result in no deviations in the terminating point of the final segment.

The above discussion pertains to the *a posteriori* characterization of a sequence of curves and an associated signature as a solution to a hybrid dynamical system. The question of how to generate such a solution *a priori* requires a definition of the forward dynamics of a hybrid dynamical system. In particular, associate with each value of the index vector a *index jump function* $\iota_{\mathbf{I}} : X \rightarrow 2^{\mathbb{F}}$, where $2^{\mathbb{F}}$ is the set of all subsets of \mathbb{F} . Now, given an initial state vector \mathbf{x}_0 and a set of initial index vectors $\{\mathbf{I}_{0,i}\}_{i=1}^l \in 2^{\mathbb{F}}$, apply the flows $\Phi_{\mathbf{I}_{0,i}}$ until the earliest time that the event surface corresponding to one of the event functions $h_{\mathbf{I}_{0,i}}$ is reached. Assign the corresponding curve $\mathbf{x}(t)$ and the corresponding value of the index

vector $\mathbf{I}_{0,i}$ as the first elements of the solution sequence ξ and the signature Σ . Proceed to apply the associated jump function $\mathbf{g}_{\mathbf{I}_{0,i}}$ to generate a new initial state vector and the index jump function $\iota_{\mathbf{I}_{0,i}}$ to generate a new set of initial index vectors. Repeat this construction for as many times as desired. In a practical implementation, the flows $\Phi_{\mathbf{I}_{0,i}}$ typically correspond to the same vector field.

Degenerate situations may occur if two event functions are reached simultaneously, in which case priority must be given on an ad hoc basis.

It is clear that there may not exist a solution with an initial condition \mathbf{x}_0 and a prescribed signature. This, however, is of no concern to the construction of \mathbf{P}_Σ , since this presupposes an existing trajectory with signature Σ and transversal intersections of the corresponding event surfaces.

Example: In order to elucidate the above discussed concept of a hybrid dynamical system, consider the microactuator previously studied by Zhao *et al.* [53] and Dankowicz *et al.* [7]. The actuator consists of a movable conducting element of mass m_2 connected to a frame of mass m_1 via a linear spring and damper. The frame consists of rigidly fixed stoppers that constrain the motion of the movable mass. Excitation of the actuator is provided by imposing an external voltage between the movable mass and an electrode rigidly fixed to the frame. Frictional contact between the frame and the underlying horizontal substrate is modeled using Coulomb and Amonton's friction laws during the slip and stick motions of the frame, respectively. When the excitation voltage exceeds a critical value, the movable mass collides with the stoppers resulting in an impulsive transfer of momentum and subsequent slipping motion of the frame. This behavior can be extended to repeated impacts by applying a periodically varying voltage across the electrodes, resulting in the desired displacement of the actuator.

The dynamics of the oscillator may be formulated as a hybrid dynamical systems in the following way. Denote the state vector by \mathbf{x} , where x^1 is the displacement of the frame

relative to the substrate, x^2 is the velocity of the frame relative to the substrate, x^3 is the displacement of the movable mass relative to the undeformed length of the linear spring, x^4 is the velocity of the movable mass relative to the frame, and x^5 is the instantaneous phase of the excitation. Then, the dynamics of the oscillator is governed by the vector fields

$$\mathbf{f}_{\text{stick}}(\mathbf{x}) = \begin{pmatrix} 0 \\ 0 \\ x^4 \\ \frac{1}{m_2} \left(\frac{\alpha V^2 \sin^2 x^5}{(d-x^3)^2} - cx^4 - kx^3 \right) \\ \omega \end{pmatrix}, \quad (2.30)$$

$$\mathbf{f}_{\text{slip}\pm}(\mathbf{x}) = \begin{pmatrix} x^2 \\ \frac{1}{m_1} \left(kx^3 + cx^4 - \left(\frac{\alpha V^2 \sin^2 x^5}{(d-x^3)^2} \right) \mp \mu_d N \right) \\ x^4 \\ \left(\frac{1}{m_1} + \frac{1}{m_2} \right) \left(\frac{\alpha V^2 \sin^2 x^5}{(d-x^3)^2} - cx^4 - kx^3 \right) \pm \frac{\mu_d N}{m_1} \\ \omega \end{pmatrix}, \quad (2.31)$$

where α is related to the permittivity of free space, d is the zero-voltage gap between the electrodes, k is the spring constant, c is the damping coefficient, V is the voltage applied between the electrodes, μ_d is the coefficient of dynamic friction, N is the normal reaction experienced by the frame from the ground and ω is the frequency of excitation; the event functions

$$h_{\text{front}}(\mathbf{x}) = \delta - x^4, \quad (2.32)$$

$$h_{\text{back}}(\mathbf{x}) = \delta + x^4, \quad (2.33)$$

$$h_{\text{stick}\pm}(\mathbf{x}) = \mp \frac{\alpha V^2 \sin^2 x^5}{(d-x^3)^2} \pm cx^4 \pm kx^3 + \mu_s N, \quad (2.34)$$

$$h_{\text{slip}\pm}(\mathbf{x}) = \pm x^2 \quad (2.35)$$

where μ_s is the coefficient of static friction; and the jump functions

$$\mathbf{g}_{\text{impact}}(\mathbf{x}) = \begin{pmatrix} x^1 \\ x^2 + \frac{(1+e)}{m_2+1}x^4 \\ x^3 \\ -ex^4 \\ x^5 \end{pmatrix} \quad (2.36)$$

$$\mathbf{g}_{\text{identity}}(\mathbf{x}) = \mathbf{x} \quad (2.37)$$

where e is the coefficient of restitution.

Now let

$$\mathbb{Z}_f = \{\text{stick,slip+},\text{slip-}\}, \quad (2.38)$$

$$\mathbb{Z}_h = \{\text{front,back,stick+},\text{stick-},\text{slip+},\text{slip-}\}, \quad (2.39)$$

$$\mathbb{Z}_g = \{\text{impact,identity}\}, \quad (2.40)$$

and suppose that \mathbb{F} is the subset of $\mathbb{Z}_f \times \mathbb{Z}_h \times \mathbb{Z}_g$ corresponding to the connectivity graph in Fig. 2.1 showing the relationship between a given vector field, the event functions that are monitored during forward simulation with the corresponding vector field, and the state jump function associated with a given event function. For example, $\mathbf{I} = (\text{stick,front,impact})$ corresponds to a trajectory segment governed by the vector field $\mathbf{f}_{\text{stick}}$, terminating on the event surface corresponding to h_{front} , and connected to the next trajectory segment by the state jump function $\mathbf{g}_{\text{impact}}$.

As shown in Fig. 2.1 the ten possible values of the index vectors for the given dynamical

system are

$$\begin{aligned}
\mathbf{J}_1 &= (\text{stick,front,impact}) \\
\mathbf{J}_2 &= (\text{stick,back,impact}) \\
\mathbf{J}_3 &= (\text{stick,stick+,identity}) \\
\mathbf{J}_4 &= (\text{stick,stick-,identity}) \\
\mathbf{J}_5 &= (\text{slip+,front,impact}) \\
\mathbf{J}_6 &= (\text{slip+,back,impact}) \\
\mathbf{J}_7 &= (\text{slip+,slip+,identity}) \\
\mathbf{J}_8 &= (\text{slip-,front,impact}) \\
\mathbf{J}_9 &= (\text{slip-,back,impact}) \\
\mathbf{J}_{10} &= (\text{slip-,slip-,identity})
\end{aligned} \tag{2.41}$$

As discussed earlier, the index jump function $\iota_{\mathbf{I}}(\mathbf{x})$ produces a set of index vectors required for the forward simulation after every transversal event of the trajectory. Specifically, in the case of the microactuator described here, the index jump function operates as follows.

$\iota_{\mathbf{I}} = \iota_{\mathbf{J}_1}(\mathbf{x}) = \iota_{\mathbf{J}_2}(\mathbf{x}) = \iota_{\mathbf{J}_5}(\mathbf{x}) = \iota_{\mathbf{J}_6}(\mathbf{x}) = \iota_{\mathbf{J}_8}(\mathbf{x}) = \iota_{\mathbf{J}_9}(\mathbf{x})$, where

$$\iota_{\mathbf{I}} = \begin{cases} \mathbf{J}_5, \mathbf{J}_6, \mathbf{J}_7, & h_{\text{slip}+}(\mathbf{g}_{\text{impact}}(\mathbf{x})) > 0 \\ \mathbf{J}_8, \mathbf{J}_9, \mathbf{J}_{10}, & h_{\text{slip}+}(\mathbf{g}_{\text{impact}}(\mathbf{x})) < 0 \\ \mathbf{J}_1, \mathbf{J}_2, \mathbf{J}_3, \mathbf{J}_4, & h_{\text{slip}+}(\mathbf{g}_{\text{impact}}(\mathbf{x})) = 0 \text{ and } h_{\text{stick}\pm}(\mathbf{g}_{\text{impact}}(\mathbf{x})) > 0 \\ \mathbf{J}_5, \mathbf{J}_6, \mathbf{J}_7, & h_{\text{slip}+}(\mathbf{g}_{\text{impact}}(\mathbf{x})) = 0 \text{ and } h_{\text{stick}\pm}(\mathbf{g}_{\text{impact}}(\mathbf{x})) \leq 0 \\ \mathbf{J}_8, \mathbf{J}_9, \mathbf{J}_{10}, & h_{\text{slip}+}(\mathbf{g}_{\text{impact}}(\mathbf{x})) = 0 \text{ and } h_{\text{slip}-}(\mathbf{g}_{\text{impact}}(\mathbf{x})) < \text{ or } > 0 \end{cases} \tag{2.42}$$

$$\iota_{\mathbf{J}_3}(\mathbf{x}) = \mathbf{J}_5, \mathbf{J}_6, \mathbf{J}_7 \tag{2.43}$$

$$\iota_{\mathbf{J}_4}(\mathbf{x}) = \mathbf{J}_8, \mathbf{J}_9, \mathbf{J}_{10} \tag{2.44}$$

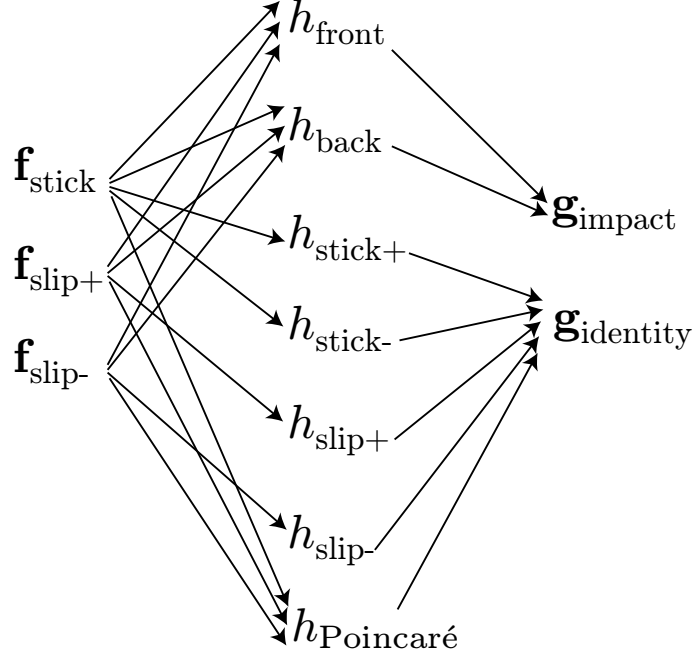


Figure 2.1: A schematic representation of the index vector and its associated vector fields, event surfaces and state jump functions.

$$\iota_{\mathbf{I}}(\mathbf{x}) = \iota_{\mathbf{J}_7}(\mathbf{x}) = \iota_{\mathbf{J}_{10}}(\mathbf{x}), \text{ where} \quad (2.45)$$

$$\iota_{\mathbf{I}} = \begin{cases} \mathbf{J}_1, \mathbf{J}_2, \mathbf{J}_3, \mathbf{J}_4, & h_{\text{slip}+}(\mathbf{g}_{\text{impact}}(\mathbf{x})) = 0 \text{ and } h_{\text{stick}\pm}(\mathbf{g}_{\text{impact}}(\mathbf{x})) > 0 \\ \mathbf{J}_5, \mathbf{J}_6, \mathbf{J}_7, & h_{\text{slip}+}(\mathbf{g}_{\text{impact}}(\mathbf{x})) = 0 \text{ and } h_{\text{stick}\pm}(\mathbf{g}_{\text{impact}}(\mathbf{x})) \leq 0 \\ \mathbf{J}_8, \mathbf{J}_9, \mathbf{J}_{10}, & h_{\text{slip}+}(\mathbf{g}_{\text{impact}}(\mathbf{x})) = 0 \text{ and } h_{\text{slip}-}(\mathbf{g}_{\text{impact}}(\mathbf{x})) < \text{ or } > 0 \end{cases} \quad (2.46)$$

Fig. 2.2 shows a two-segment periodic trajectory of the microactuator. Here, an initial condition on 1-st segment uses the index vectors $\mathbf{J}_1, \mathbf{J}_2, \mathbf{J}_3, \mathbf{J}_4$. In this case, during the forward time evolution, the first transversal intersection occurs with the event surface define by $h_{\text{front}} = 0$. Now, the jump function $\mathbf{g}_{\text{impact}}$ is applied to the terminal point to obtain an initial condition for the 2-segment. Also, the index jump function ι_1 is applied to produce a new set of index vectors $\mathbf{J}_5, \mathbf{J}_6, \mathbf{J}_7$. Similarly, the new initial condition is used for the forward time evolution with the newly produced index vectors. For the scenario shown in Fig. 2.2, the 2-nd segment terminates at the event function $h_{\text{slip}+} = 0$ and after applying $\mathbf{g}_{\text{identity}}$, the state matches the initial condition for the 1-st segment marking the trajectory as periodic.

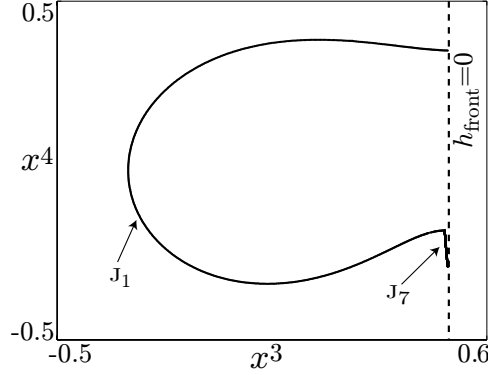


Figure 2.2: The figure illustrates a two-segment periodic trajectory corresponding to the microactuator described here. The index vectors that contain the information about the vector field, the terminal event surface and the state jump function corresponding to the each segment are also shown.

2.3 Periodic Trajectories

A *periodic trajectory* of a smooth dynamical system is a trajectory $\mathbf{x}(t)$, such that $\mathbf{x}(t+T) = \mathbf{x}(t)$ for some T and all t . Similarly, suppose that there exists a trajectory

$$\xi = \{\mathbf{x}_j : (t_{j-1}, t_j] \rightarrow X\}_{j=1}^m \quad (2.47)$$

with signature Σ of a hybrid dynamical system, such that

$$\lim_{t \rightarrow t_0^+} \mathbf{x}_1(t) = \mathbf{g}_{\mathbf{I}_m}(\mathbf{x}_m(t_m)). \quad (2.48)$$

Then, the periodic trajectory ξ^* together with its signature Σ^* is a periodic extension of ξ and Σ . Here, ξ and Σ represent a *base unit* of the periodic trajectory. Indeed, given a point $\mathbf{x}^*(t_0)$ on a periodic trajectory of a smooth dynamical system with vector field \mathbf{f} , let

$$h(\mathbf{x}) = \mathbf{f}(\mathbf{x}^*(t_0)) \cdot (\mathbf{x} - \mathbf{x}^*(t_0)). \quad (2.49)$$

The trajectory $\xi = \{\mathbf{x}^* : t \in (t_0, t_0 + T]\}$ with $\mathbf{I}(t) = \mathbf{I}^*$ is then a periodic trajectory of the hybrid dynamical system with vector field $\mathbf{f}_{\mathbf{I}^*} = \mathbf{f}$, event function $h_{\mathbf{I}^*} = h$, and state jump function $\mathbf{g}_{\mathbf{I}^*}$ equal to the identity map. The point $\mathbf{x}^*(t_0)$ is a fixed point of the corresponding

hybrid flow map \mathbf{P}_Σ and

$$\mathbf{P}_{\Sigma, \mathbf{x}}(\mathbf{x}^*(t_0)) = \left(Id - \frac{\mathbf{f}(\mathbf{x}^*(t_0)) \cdot h_{\mathbf{x}}(\mathbf{x}^*(t_0))}{h_{\mathbf{x}}(\mathbf{x}^*(t_0)) \cdot \mathbf{f}(\mathbf{x}^*(t_0))} \right) \cdot \Phi_{, \mathbf{x}}(\mathbf{x}^*(t_0), T). \quad (2.50)$$

In this case, the hybrid flow map is often referred to as a *Poincaré map* and the event surface corresponding to h is then known as a *Poincaré section*. From Eq. (2.29) it further follows that $\mathbf{f}(\mathbf{x}^*(t_0))$ is an eigenvector of the Poincaré map corresponding to the eigenvalue 0.

2.4 Quasiperiodic Trajectories

An embedded k -dimensional *torus* in the state space X of a n -dimensional dynamical system is a co-dimension- $(n - k)$ hypersurface parameterized by k angle variables. The torus is said to be *invariant* if any solution based at an initial condition on the hypersurface remains on the hypersurface for all time. As a special case, the points on a periodic trajectory constitute a one-dimensional invariant torus of the dynamical system. A trajectory is said to *densely cover* an invariant torus if any point on the torus can be approximated arbitrarily closely by some point on the trajectory. In this case, the trajectory is said to be *quasiperiodic* and can be represented by a complex Fourier series

$$\mathbf{x}(t) = \sum_{n_1, n_2, n_3, \dots, n_k}^{\infty} \mathbf{C}_{n_1, n_2, n_3, \dots, n_k} e^{i(\mathbf{n} \cdot \boldsymbol{\Omega})t} \quad (2.51)$$

where

$$\boldsymbol{\Omega} = \left[\omega_1 \quad \omega_2 \quad \omega_3 \quad \cdots \quad \omega_k \right]^T, \omega_i \in \mathbb{R}, \quad (2.52)$$

$$\mathbf{n} = \left[n_1 \quad n_2 \quad n_3 \quad \cdots \quad n_k \right], n_i \in \mathbb{Z}, \quad (2.53)$$

and such that

$$\mathbf{n} \cdot \boldsymbol{\Omega} = 0 \quad (2.54)$$

only if

$$n_1 = n_2 = n_3 = \dots = n_k = 0. \quad (2.55)$$

Consider a quasiperiodic trajectory on a k -dimensional invariant torus that intersects the Poincaré section \mathcal{P} transversely along a $k - 1$ -dimensional invariant torus, such that any point on the torus can be approximated arbitrarily closely by some point of intersection of the trajectory with \mathcal{P} (cf. Fig. 2.3). For every point \mathbf{x}^* on the intersection, the analysis in a previous section implies the existence of a unique smooth function $\tau(\mathbf{x})$ defined on a neighborhood of \mathbf{x}^* , such that $\tau(\mathbf{x})$ is the time-of-flight under the flow Φ until the next point of intersection of the quasiperiodic trajectory with \mathcal{P} given by $\mathbf{P}(\mathbf{x}) = \Phi(\mathbf{x}, \tau(\mathbf{x}))$. By uniqueness, the map \mathbf{P} can be smoothly extended to a neighborhood of the entire invariant torus. In a computational context, $\mathbf{P}(\mathbf{x})$ for some \mathbf{x} in this neighborhood of the torus may be approximated by

$$\mathbf{P}(\mathbf{x}^*) + \mathbf{P}_{,\mathbf{x}}(\mathbf{x}^*) \cdot (\mathbf{x} - \mathbf{x}^*) \quad (2.56)$$

for some nearby point \mathbf{x}^* of intersection of the quasiperiodic trajectory with \mathcal{P} .

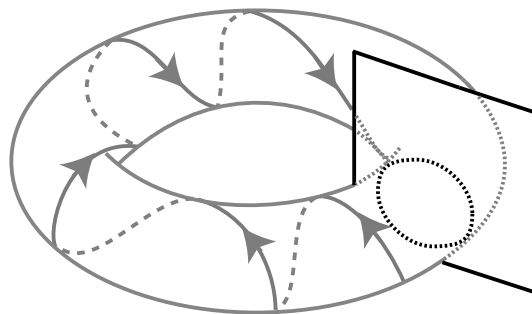


Figure 2.3: Illustration of a quasiperiodic motion. A Poincaré section is also shown where the trajectories intersect the torus in a closed curve (shown as a dotted ellipse).

2.5 Tangential Intersections

Consider a hybrid dynamical system with a single-element index space $\mathbb{F} = \{\mathbf{I}\}$, such that $\mathbf{f}_{\mathbf{I}} \stackrel{def}{=} \mathbf{f}$ governs the continuous-in-time (and space) evolution of the corresponding state vector \mathbf{x} , interrupted by discontinuous-in-space jumps governed by a smooth state jump function $\mathbf{g}_{\mathbf{I}} \stackrel{def}{=} \mathbf{g}_{\mathcal{D}}$ triggered at discrete times by the intersection of system trajectories with the event

surface \mathcal{D} corresponding to the zero-level surface of the smooth event function $h_{\mathbf{I}} \stackrel{\text{def}}{=} h_{\mathcal{D}}$. In particular, assume that the continuous-in-time dynamics apply to the region $h_{\mathcal{D}} \geq 0$, that $\mathbf{g}_{\mathcal{D}}$ maps *event-triggering states* to the region $h_{\mathcal{D}} \geq 0$, and that $\mathbf{g}_{\mathcal{D}}$ and the vector field \mathbf{f} and corresponding flow Φ can be smoothly extended to an open neighborhood of \mathcal{D} .

A point $\mathbf{x} \in \mathcal{D}$ is an event-triggering state only if

$$h_{\mathcal{P}}(\mathbf{x}) \stackrel{\text{def}}{=} h_{\mathcal{D},\mathbf{x}}(\mathbf{x}) \cdot \mathbf{f}(\mathbf{x}) \leq 0, \quad (2.57)$$

since, otherwise, it belongs to a trajectory segment of Φ that originates in $h_{\mathcal{D}} < 0$. In particular, *transversal events* correspond to those points on \mathcal{D} for which $h_{\mathcal{P}} < 0$. By continuity, it follows that the vector field is transversal to \mathcal{D} on an open neighborhood of any transversal event. By the implicit function theorem, it then follows that \mathcal{D} is a local Poincaré section in the vicinity of any transversal event, i.e., that for every trajectory of Φ on an open neighborhood of a transversal event, there exists a unique point of intersection with \mathcal{D} . In contrast, *grazing events* are those points on \mathcal{D} for which $h_{\mathcal{P}} = 0$. Trajectories of Φ near a grazing event need not intersect \mathcal{D} and may intersect in multiple points when they do. Thus, \mathcal{D} **does not** serve as a suitable local Poincaré section in the vicinity of a grazing event.

From the point of view of numerical simulation of the corresponding dynamical system, transversal events are straightforward to detect numerically and persist even in the presence of small integration errors. In contrast, grazing events are difficult to detect numerically and need not persist in the presence of small integration errors. This makes simulations involving near-grazing events error-prone and very time consuming even at reasonable accuracy.

To enable accurate detection of near-grazing events, consider the co-dimension-one surface \mathcal{P} corresponding to the zero-level surface of $h_{\mathcal{P}}$. Here, \mathcal{P} consists of local extrema in the value of $h_{\mathcal{D}}$ along system trajectories intersecting \mathcal{P} . Indeed, suppose that $\mathbf{x} \in \mathcal{P}$ and consider the function

$$\eta(t) = h_{\mathcal{D}}(\Phi(\mathbf{x}, t)). \quad (2.58)$$

It follows that

$$\dot{\eta}(0) = h_{\mathcal{D},\mathbf{x}}(\mathbf{x}) \cdot \mathbf{f}(\mathbf{x}) = h_{\mathcal{P}}(\mathbf{x}) \quad (2.59)$$

and the claim follows. Indeed, since

$$\ddot{\eta}(0) = h_{\mathcal{P},\mathbf{x}}(\mathbf{x}) \cdot \mathbf{f}(\mathbf{x}), \quad (2.60)$$

it follows that points on \mathcal{P} for which $h_{\mathcal{P},\mathbf{x}}(\mathbf{x}) \cdot \mathbf{f}(\mathbf{x}) \neq 0$ correspond to local maxima ($h_{\mathcal{P},\mathbf{x}}(\mathbf{x}) \cdot \mathbf{f}(\mathbf{x}) < 0$) or local minima ($h_{\mathcal{P},\mathbf{x}}(\mathbf{x}) \cdot \mathbf{f}(\mathbf{x}) > 0$), respectively, in the value of $h_{\mathcal{D}}$ along the corresponding system trajectories of Φ . Finally, from the transversality of the vector field with \mathcal{P} at such points, it follows that \mathcal{P} is a local Poincaré section in their vicinity and that intersections with \mathcal{P} are again straightforward to detect numerically.

Denote by \mathcal{D}^0 the (co-dimension-two) intersection $\mathcal{P} \cap \mathcal{D}$ and suppose that $a_* \stackrel{\text{def}}{=} h_{\mathcal{P},\mathbf{x}}(\mathbf{x}_*) \cdot \mathbf{f}(\mathbf{x}_*) > 0$ for some grazing event $\mathbf{x}_* \in \mathcal{D}^0$. It follows that \mathbf{x}_* is a local simple minimum in the value of $h_{\mathcal{D}}$ along a system trajectory. Moreover, ignoring the effects of $\mathbf{g}_{\mathcal{D}}$, nearby trajectories achieve **unique and guaranteed** intersections with \mathcal{P} in the vicinity of \mathbf{x}_* . For each such intersection $\mathbf{x} \in \mathcal{P}$, define the *penetration* π of the corresponding trajectory by the formula $\pi = -h_{\mathcal{D}}(\mathbf{x})$. It follows that trajectories with negative penetration pass a neighborhood of \mathbf{x}_* without intersecting \mathcal{D} , whereas trajectories with positive (zero) penetration intersect \mathcal{D} near \mathbf{x}_* at transversal (grazing) events. Indeed, having located points of intersection with \mathcal{P} for which $\pi > 0$, we may apply numerical techniques designed to locate the corresponding transversal events.

2.5.1 Discontinuity Maps

For each trajectory of Φ on an open neighborhood of a transversal event, the continuous-in-time evolution is thus guaranteed to be interrupted by a discontinuous-in-space jump governed by $\mathbf{g}_{\mathcal{D}}$. In contrast, for trajectories of Φ on an open neighborhood of a grazing event, discontinuous-in-space jumps only occur for trajectories with nonnegative penetration, a condition that requires detection of intersections with \mathcal{P} . In the case of near-grazing

trajectories, therefore, it appears desirable to locally replace the event surface \mathcal{D} (and its event function $h_{\mathcal{D}}$) and the state jump function $\mathbf{g}_{\mathcal{D}}$ with the event surface \mathcal{P} (and its event function $h_{\mathcal{P}}$) and an associated state jump function $\mathbf{g}_{\mathcal{P}}$ known as a *discontinuity map*.

For this purpose, as shown in Fig. 2.4, denote by *incoming* (*outgoing*) trajectory segments, those segments of trajectories of Φ on some neighborhood of \mathbf{x}_* that terminate on \mathcal{P} in forward (backward) time. Suppose that $\mathbf{g}_{\mathcal{D}}|_{\mathcal{D}_0}$ equals the identity and that $\mathbf{g}_{\mathcal{D}}$ maps transversal events to points on outgoing trajectory segments. It follows that the desired event map $\mathbf{g}_{\mathcal{P}}$ maps points of intersection of incoming trajectory segments with \mathcal{P} to points of intersection of the corresponding outgoing trajectory segments with \mathcal{P} . Clearly, $\mathbf{g}_{\mathcal{P}}|_{\mathcal{P} \cap \{h_{\mathcal{D}} \geq 0\}}$ equals the identity, since the corresponding incoming trajectories have nonpositive penetration and thus experience no event-triggered discontinuous jump under $\mathbf{g}_{\mathcal{D}}$. In contrast, on the set $\mathcal{P} \cap \{h_{\mathcal{D}} < 0\}$, $\mathbf{g}_{\mathcal{P}}$ accounts for the flow with Φ backward in time to the point of intersection with \mathcal{D} , the application of the event map $\mathbf{g}_{\mathcal{D}}$, and the subsequent flow with Φ backward in time to \mathcal{P} .

To obtain an analytical expression for $\mathbf{g}_{\mathcal{P}}$ on a neighborhood of \mathbf{x}_* , consider the collection of trajectory segments shown in Fig. 2.4. Here, the point $\mathbf{x}_0 \in \mathcal{P}$ is a terminal point in forward time on an incoming trajectory segment of Φ , whereas \mathbf{x}_1 is the terminal point in backward time on the corresponding outgoing trajectory segment of Φ , i.e., $\mathbf{g}_{\mathcal{P}}(\mathbf{x}_0) = \mathbf{x}_1$.

Denote by $\mathbf{x}_{in} \in \mathcal{D}$ the point of intersection of the incoming trajectory segment with \mathcal{D} and let $\mathbf{x}_{out} = \mathbf{g}_{\mathcal{D}}(\mathbf{x}_{in})$. Assuming that t is the time elapsed in the flow from \mathbf{x}_0 to \mathbf{x}_{in} and since $\mathbf{x}_{in} \in \mathcal{D}$ we have

$$h_{\mathcal{D}}(\Phi(\mathbf{x}_0, t)) = h_{\mathcal{D}}(\mathbf{x}_0) + th_{\mathcal{P}}(\mathbf{x}_0) + \frac{t^2}{2}h_{\mathcal{P},\mathbf{x}}(\mathbf{x}_0) \cdot \mathbf{f}(\mathbf{x}_0) + \mathcal{O}(t^3) = 0. \quad (2.61)$$

Since $h_{\mathcal{P}}(\mathbf{x}_0) = 0$, and $h_{\mathcal{P},\mathbf{x}}(\mathbf{x}_0) \cdot \mathbf{f}(\mathbf{x}_0) > 0$ for $\mathbf{x}_0 \approx \mathbf{x}_*$, it follows that

$$t \approx \sqrt{-\frac{2h_{\mathcal{D}}(\mathbf{x}_0)}{h_{\mathcal{P},\mathbf{x}}(\mathbf{x}_0) \cdot \mathbf{f}(\mathbf{x}_0)}} \approx \sqrt{2\frac{-h_{\mathcal{D}}(\mathbf{x}_*) - h_{\mathcal{D},\mathbf{x}}(\mathbf{x}_*) \cdot (\mathbf{x}_0 - \mathbf{x}_*)}{h_{\mathcal{P},\mathbf{x}}(\mathbf{x}_0) \cdot \mathbf{f}(\mathbf{x}_0)}}. \quad (2.62)$$

Since $h_{\mathcal{D}}(\mathbf{x}_*) = 0$, from the above equation it follows that the elapsed time from \mathbf{x}_0 to \mathbf{x}_{in} and, consequently, the position of \mathbf{x}_{in} is $\mathcal{O}\left(\sqrt{-h_{\mathcal{D},x}(\mathbf{x}_*) \cdot (\mathbf{x}_0 - \mathbf{x}_*)}\right)$.

To enable a smooth analysis in spite of the presence of this dependence on the square root of the deviation from \mathbf{x}_* , let $\tilde{\mathbf{x}}_{in}$ denote a point on the incoming trajectory segment for which $h_{\mathcal{D}}(\tilde{\mathbf{x}}_{in}) - h_{\mathcal{D}}(\mathbf{x}_0) = y^2$ for some (as-of-yet) undetermined quantity y and let $\tilde{\mathbf{x}}_{out} = \mathbf{g}_{\mathcal{D}}(\tilde{\mathbf{x}}_{in})$. Finally, denote by $\tilde{\mathbf{x}}_1$ the terminal point in backward time on the outgoing trajectory segment of Φ through $\tilde{\mathbf{x}}_{out}$. Clearly, $\tilde{\mathbf{x}}_{in} = \mathbf{x}_{in}$, $\tilde{\mathbf{x}}_{out} = \mathbf{x}_{out}$, and $\tilde{\mathbf{x}}_1 = \mathbf{x}_1$ provided that $y = \sqrt{-h_{\mathcal{D}}(\mathbf{x}_0)}$.

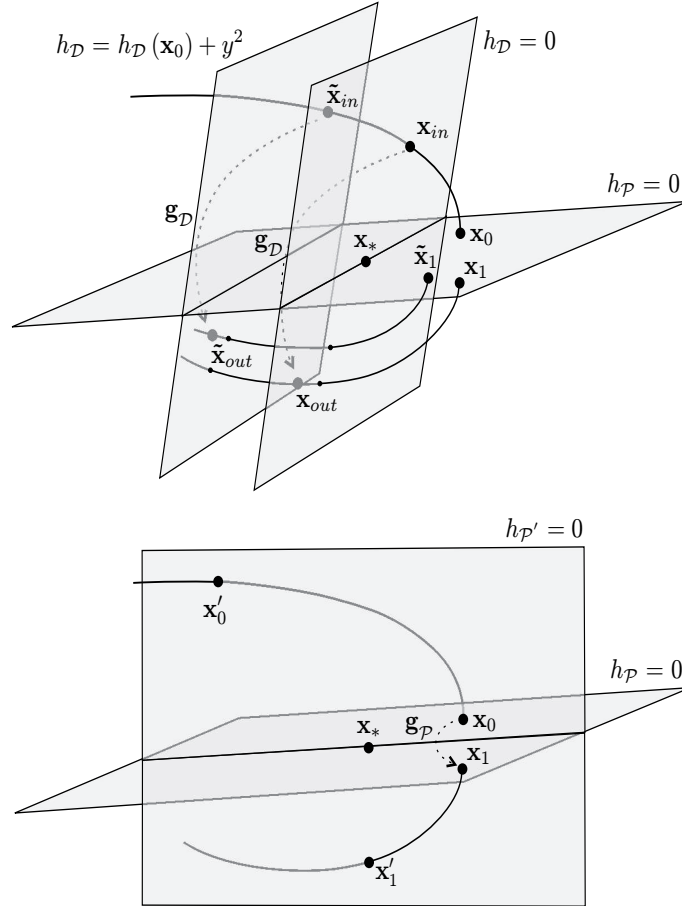


Figure 2.4: Schematic of the trajectories near the grazing point depicting the discontinuity-mapping approach with \mathcal{D} and \mathcal{P} (upper panel) and \mathcal{P}' and \mathcal{P} (lower panel). Gray curves correspond to the trajectories that are on the side of \mathcal{P}' for which $h_{\mathcal{P}'} > 0$.

To locate $\tilde{\mathbf{x}}_{in}$, $\tilde{\mathbf{x}}_{out}$, and $\tilde{\mathbf{x}}_1$ as functions of \mathbf{x}_0 and y , consider the set of vector-valued equations

$$\tilde{\mathbf{x}}_{in} - \Phi(\mathbf{x}_0, -v_1) = \mathbf{0}, \quad (2.63)$$

$$\tilde{\mathbf{x}}_{out} - \mathbf{g}_{\mathcal{D}}(\tilde{\mathbf{x}}_{in}) = \mathbf{0}, \quad (2.64)$$

$$\tilde{\mathbf{x}}_1 - \Phi(\tilde{\mathbf{x}}_{out}, -v_2) = \mathbf{0}, \quad (2.65)$$

and the accompanying pair of scalar equations

$$v_1 \sqrt{\frac{h_{\mathcal{D}}(\Phi(\mathbf{x}_0, -v_1)) - h_{\mathcal{D}}(\mathbf{x}_0) + v_1 h_{\mathcal{P}}(\mathbf{x}_0)}{v_1^2}} - y = 0, \quad (2.66)$$

$$h_{\mathcal{P}}(\tilde{\mathbf{x}}_1) = 0, \quad (2.67)$$

where v_1 and v_2 are the elapsed times from $\tilde{\mathbf{x}}_{in}$ to \mathbf{x}_0 and from $\tilde{\mathbf{x}}_1$ to $\tilde{\mathbf{x}}_{out}$, respectively (cf. [7, 8, 46, 52, 53]). Solving Eq. (2.63) for $\tilde{\mathbf{x}}_{in}$ and substituting the result into Eq. (2.66), using the fact that $h_{\mathcal{P}}(\mathbf{x}_0) = 0$, yields

$$v_1 \sqrt{\frac{h_{\mathcal{D}}(\tilde{\mathbf{x}}_{in}) - h_{\mathcal{D}}(\mathbf{x}_0)}{v_1^2}} - y = 0, \quad (2.68)$$

which for $v_1 > 0$ is consistent with the assertion that $h_{\mathcal{D}}(\tilde{\mathbf{x}}_{in}) - h_{\mathcal{D}}(\mathbf{x}_0) = y^2$.

The above set of Eqs. (2.63 – 2.67) are smooth in the unknown variables $\tilde{\mathbf{x}}_{in}$, $\tilde{\mathbf{x}}_{out}$, $\tilde{\mathbf{x}}_1$, v_1 , and v_2 on a neighborhood of $\tilde{\mathbf{x}}_{in} = \tilde{\mathbf{x}}_{out} = \tilde{\mathbf{x}}_1 = \mathbf{x}_*$ and $v_1 = v_2 = 0$ as per Eq. (2.61). Moreover, the corresponding Jacobian matrix evaluated at $\tilde{\mathbf{x}}_{in} = \tilde{\mathbf{x}}_{out} = \tilde{\mathbf{x}}_1 = \mathbf{x}_*$ and $v_1 = v_2 = 0$ is nonsingular and is given by

$$\begin{pmatrix} Id & \mathbf{0} & \mathbf{0} & \mathbf{f} & \mathbf{0} \\ -\mathbf{g}_{\mathcal{D},\mathbf{x}} & Id & \mathbf{0} & \mathbf{0} & \mathbf{0} \\ \mathbf{0} & -Id & Id & \mathbf{0} & \mathbf{f} \\ \mathbf{0} & \mathbf{0} & \mathbf{0} & \alpha & \mathbf{0} \\ \mathbf{0} & \mathbf{0} & h_{\mathcal{P},\mathbf{x}} & \mathbf{0} & \mathbf{0} \end{pmatrix}, \quad (2.69)$$

where $\alpha = \sqrt{\frac{a_*}{2}}$, bold-faced $\mathbf{0}$'s correspond to either matrices or (row- and column-)vectors with all zero elements. The determinant of the above matrix equals $-\sqrt{\frac{a_*^3}{2}} \neq 0$, thus

establishing through the implicit function theorem unique smooth functions $\tilde{\mathbf{X}}_{in}(\mathbf{x}_0, y)$, $\tilde{\mathbf{X}}_{out}(\mathbf{x}_0, y)$, $\tilde{\mathbf{X}}_1(\mathbf{x}_0, y)$, $\Upsilon_1(\mathbf{x}_0, y)$ and $\Upsilon_2(\mathbf{x}_0, y)$ on a neighborhood of $\mathbf{x}_0 = \mathbf{x}_*$ and $y = 0$, such that the above equations are satisfied identically by $\tilde{\mathbf{x}}_{in} = \tilde{\mathbf{X}}_{in}(\mathbf{x}_0, y)$, $\tilde{\mathbf{x}}_{out} = \tilde{\mathbf{X}}_{out}(\mathbf{x}_0, y)$, $\tilde{\mathbf{x}}_1 = \tilde{\mathbf{X}}_1(\mathbf{x}_0, y)$, $v_1 = \Upsilon_1(\mathbf{x}_0, y)$, and $v_2 = \Upsilon_2(\mathbf{x}_0, y)$. Thus, in conclusion, for $h_{\mathcal{D}}(\mathbf{x}_0) < 0$, the discontinuity map is given by

$$\mathbf{g}_{\mathcal{P}}(\mathbf{x}_0) = \tilde{\mathbf{X}}_1\left(\mathbf{x}_0, \sqrt{-h_{\mathcal{D}}(\mathbf{x}_0)}\right). \quad (2.70)$$

Suppose that \mathcal{P}' is the event surface corresponding to an event function $h_{\mathcal{P}'}$, such that

$$h_{\mathcal{P}'}(\mathbf{x}_*) = 0 \quad (2.71)$$

and

$$h_{\mathcal{P}', \mathbf{x}}(\mathbf{x}_*) \cdot \mathbf{f}(\mathbf{x}_*) < 0 \quad (2.72)$$

and refer again to Fig. 2.4. Here, the points \mathbf{x}'_0 and \mathbf{x}'_1 are the unique intersections with \mathcal{P}' of the incoming and outgoing trajectory segments of Φ through \mathbf{x}_0 and \mathbf{x}_1 , respectively. Finally, $\tilde{\mathbf{x}}'_1$ is the unique intersection with \mathcal{P}' of the outgoing trajectory segment of Φ through $\tilde{\mathbf{x}}_1$. The associated discontinuity map $\mathbf{g}_{\mathcal{P}'}$ now accounts for the flow with Φ forward in time to the point of intersection with \mathcal{P} , the application of $\mathbf{g}_{\mathcal{P}}$, and the subsequent flow with Φ back to \mathcal{P}' . Indeed, consider the addition of the equations

$$\mathbf{x}_0 - \Phi(\mathbf{x}'_0, \sigma_1) = \mathbf{0}, \quad (2.73)$$

$$\tilde{\mathbf{x}}'_1 - \Phi(\tilde{\mathbf{x}}_1, \sigma_2) = \mathbf{0}, \quad (2.74)$$

$$h_{\mathcal{P}}(\mathbf{x}_0) = 0, \quad (2.75)$$

$$h_{\mathcal{P}'}(\tilde{\mathbf{x}}'_1) = 0, \quad (2.76)$$

to Eqs. (2.63-2.67), where now σ_1 and σ_2 are the elapsed times from \mathbf{x}'_0 to \mathbf{x}_0 and from $\tilde{\mathbf{x}}_1$ to $\tilde{\mathbf{x}}'_1$, respectively.

Again, the corresponding set of equations is smooth in the unknown variables \mathbf{x}_0 , $\tilde{\mathbf{x}}_{in}$, $\tilde{\mathbf{x}}_{out}$, $\tilde{\mathbf{x}}_1$, $\tilde{\mathbf{x}}'_1$, v_1 , v_2 , σ_1 , and σ_2 on a neighborhood of $\mathbf{x}_0 = \tilde{\mathbf{x}}_{in} = \tilde{\mathbf{x}}_{out} = \tilde{\mathbf{x}}_1 = \tilde{\mathbf{x}}'_1 = \mathbf{x}_*$ and

$v_1 = v_2 = \sigma_1 = \sigma_2 = 0$. The Jacobian matrix of these set of equations is then given by

$$\begin{pmatrix} -Id & Id & \mathbf{0} & \mathbf{0} & \mathbf{0} & \mathbf{f} & \mathbf{0} & \mathbf{0} & \mathbf{0} \\ \mathbf{0} & -\mathbf{g}_{\mathcal{D},\mathbf{x}} & Id & \mathbf{0} & \mathbf{0} & \mathbf{0} & \mathbf{0} & \mathbf{0} & \mathbf{0} \\ \mathbf{0} & \mathbf{0} & -Id & Id & \mathbf{0} & \mathbf{0} & \mathbf{f} & \mathbf{0} & \mathbf{0} \\ \mathbf{0} & \mathbf{0} & \mathbf{0} & \mathbf{0} & \mathbf{0} & \alpha & 0 & 0 & 0 \\ \mathbf{0} & \mathbf{0} & \mathbf{0} & h_{\mathcal{P},\mathbf{x}} & \mathbf{0} & 0 & 0 & 0 & 0 \\ Id & \mathbf{0} & \mathbf{0} & \mathbf{0} & \mathbf{0} & \mathbf{0} & \mathbf{0} & -\mathbf{f} & 0 \\ \mathbf{0} & \mathbf{0} & \mathbf{0} & -Id & Id & \mathbf{0} & \mathbf{0} & \mathbf{0} & -\mathbf{f} \\ h_{\mathcal{P},\mathbf{x}} & \mathbf{0} & \mathbf{0} & \mathbf{0} & \mathbf{0} & 0 & 0 & 0 & 0 \\ \mathbf{0} & \mathbf{0} & \mathbf{0} & \mathbf{0} & h_{\mathcal{P}',\mathbf{x}} & 0 & 0 & 0 & 0 \end{pmatrix}, \quad (2.77)$$

and its determinant equals

$$-(h_{\mathcal{P}',\mathbf{x}}(\mathbf{x}_*) \cdot \mathbf{f}(\mathbf{x}_*)) \sqrt{\frac{a_*^5}{2}} \neq 0. \quad (2.78)$$

Thus, the implicit function theorem guarantees the existence of unique smooth functions $\mathbf{X}_0(\mathbf{x}'_0)$, $\tilde{\mathbf{X}}_{in}(\mathbf{x}'_0, y)$, $\tilde{\mathbf{X}}_{out}(\mathbf{x}'_0, y)$, $\tilde{\mathbf{X}}_1(\mathbf{x}'_0, y)$, $\tilde{\mathbf{X}}'_1(\mathbf{x}'_0, y)$, $\Upsilon_1(\mathbf{x}'_0, y)$, $\Upsilon_2(\mathbf{x}'_0, y)$, $\Sigma_1(\mathbf{x}'_0, y)$, and $\Sigma_2(\mathbf{x}'_0, y)$ on a neighborhood of $\mathbf{x}'_0 = \mathbf{x}_*$ and $y = 0$, such that the complete set of equations is satisfied identically by $\mathbf{x}_0 = \mathbf{X}_0(\mathbf{x}'_0)$, $\tilde{\mathbf{x}}_{in} = \tilde{\mathbf{X}}_{in}(\mathbf{x}'_0, y)$, $\tilde{\mathbf{x}}_{out} = \tilde{\mathbf{X}}_{out}(\mathbf{x}'_0, y)$, $\tilde{\mathbf{x}}_1 = \tilde{\mathbf{X}}_1(\mathbf{x}'_0, y)$, $\tilde{\mathbf{x}}'_1 = \tilde{\mathbf{X}}'_1(\mathbf{x}'_0, y)$, $v_1 = \Upsilon_1(\mathbf{x}'_0, y)$, $v_2 = \Upsilon_2(\mathbf{x}'_0, y)$, $\sigma_1 = \Sigma_1(\mathbf{x}'_0, y)$, and $\sigma_2 = \Sigma_2(\mathbf{x}'_0, y)$.

Now let $h_{\mathcal{D}'}(\mathbf{x}') \stackrel{\text{def}}{=} h_{\mathcal{D}}(\mathbf{X}_0(\mathbf{x}'))$ for $\mathbf{x}' \in \mathcal{P}'$ in the vicinity of \mathbf{x}_* . It then follows that, for $h_{\mathcal{D}'}(\mathbf{x}'_0) \geq 0$, the corresponding discontinuity map equals the identity, while for $h_{\mathcal{D}'}(\mathbf{x}'_0) < 0$,

$$\mathbf{g}_{\mathcal{P}'}(\mathbf{x}'_0) = \tilde{\mathbf{X}}'_1 \left(\mathbf{x}'_0, \sqrt{-h_{\mathcal{D}}(\mathbf{X}_0(\mathbf{x}'_0))} \right). \quad (2.79)$$

2.5.2 Global Poincaré Sections

In the case when \mathbf{x}_* is an isolated grazing event (with $a_* > 0$) along a periodic trajectory of the dynamical system, then the local Poincaré section \mathcal{P} is a Poincaré section for the flow Φ on a neighborhood of the periodic trajectory. The corresponding smooth *global Poincaré*

map $\mathbf{P}_{\text{smooth}} : \mathcal{P} \rightarrow \mathcal{P}$ (or $\mathbf{P}'_{\text{smooth}} : \mathcal{P}' \rightarrow \mathcal{P}'$) describes the dynamics of trajectories in the vicinity of the periodic trajectory when ignoring any transversal events near \mathbf{x}^* by means of the time-history of their discrete intersections with \mathcal{P} (or \mathcal{P}'). A global Poincaré map $\mathbf{P} : \mathcal{P} \rightarrow \mathcal{P}$ (or $\mathbf{P}' : \mathcal{P}' \rightarrow \mathcal{P}'$) that accurately accounts for transversal events in the vicinity of \mathbf{x}_* can then be directly constructed by composing the smooth global Poincaré map and the corresponding discontinuity maps,

$$\mathbf{P} = \mathbf{P}_{\text{smooth}} \circ \mathbf{g}_{\mathcal{P}} \quad (2.80)$$

or

$$\mathbf{P}' = \mathbf{P}'_{\text{smooth}} \circ \mathbf{g}_{\mathcal{P}'}. \quad (2.81)$$

Suppose, instead, that \mathbf{x}_* is an isolated grazing event (with $a_* > 0$) along a quasiperiodic trajectory of the dynamical system that lies in its entirety in $h_{\mathcal{D}} > 0$ away from \mathbf{x}_* . Then, although \mathcal{P} is a local Poincaré section for trajectory segments in the vicinity of \mathbf{x}_* , it is certainly conceivable that it fails to be a global Poincaré section through the existence of points of tangentiality of the vector field along the corresponding invariant torus with \mathcal{P} . The previous analysis still applies, however, if a separate Poincaré section \mathcal{P}' can be found that is everywhere transversal to the torus. For example, when the vector field \mathbf{f} is periodic in a phase variable $\theta \in \mathcal{S}^1$, such that $\dot{\theta} > 0$, a constant-phase section may be constructed through \mathbf{x}_* that will be everywhere transversal to the corresponding flow Φ .

The derivation of the discontinuity map $\mathbf{g}_{\mathcal{P}}$ (or $\mathbf{g}_{\mathcal{P}'}$) only ensures its existence on some neighborhood of the grazing event. In the case of a periodic trajectory of Φ , this poses no difficulty to the practical simulation of the dynamical system using compositions of the global Poincaré map and the discontinuity map since only local behavior in the vicinity of the grazing trajectory is sought. In contrast, in the case of a quasiperiodic grazing trajectory, it is possible to be close to the quasiperiodic trajectory after the application of $\mathbf{P}_{\text{smooth}}$ and yet be away from \mathbf{x}_* . In this case, an ad hoc *a priori* choice of neighborhood about \mathbf{x}_* is introduced, such that $\mathbf{g}_{\mathcal{P}}$ is automatically assumed to be the identity for points outside of this neighborhood. *A posteriori* verification is then made to ensure that recurrent trajectories

that pass through this neighborhood do not involve events outside of this neighborhood not already present for the grazing trajectory.

2.5.3 Local Approximations

The two sets of smooth functions $\tilde{\mathbf{X}}_{in}(\mathbf{x}_0, y)$, $\tilde{\mathbf{X}}_{out}(\mathbf{x}_0, y)$, $\tilde{\mathbf{X}}_1(\mathbf{x}_0, y)$, $\Upsilon_1(\mathbf{x}_0, y)$ and $\Upsilon_2(\mathbf{x}_0, y)$ or $\mathbf{X}_0(\mathbf{x}'_0)$, $\tilde{\mathbf{X}}_{in}(\mathbf{x}'_0, y)$, $\tilde{\mathbf{X}}_{out}(\mathbf{x}'_0, y)$, $\tilde{\mathbf{X}}_1(\mathbf{x}'_0, y)$, $\tilde{\mathbf{X}}'_1(\mathbf{x}'_0, y)$, $\Upsilon_1(\mathbf{x}'_0, y)$, $\Upsilon_2(\mathbf{x}'_0, y)$, $\Sigma_1(\mathbf{x}'_0, y)$, and $\Sigma_2(\mathbf{x}'_0, y)$ are implicitly defined by the set of equations (2.63-2.67, 2.73-2.76). It is possible to compute arbitrary partial derivatives of these functions with respect their argument evaluated at $\mathbf{x}_0 = \mathbf{x}'_0 = \mathbf{x}_*$ and $y = 0$ by using implicit differentiation of the defining equations and demanding that all partial derivatives of the corresponding left-hand sides must vanish. Taylor's theorem may then be employed to obtain polynomial approximations to these functions in the deviation from $\mathbf{x}_0 = \mathbf{x}'_0 = \mathbf{x}_*$ and $y = 0$. Using Eqs. (2.70) and (2.79), similar (yet typically non-differentiable due to the presence of the square-root) approximations may be obtained for \mathbf{g}_P and $\mathbf{g}_{P'}$ in terms of the deviation from \mathbf{x}_* .

For example, consider the function

$$\begin{aligned} E(\mathbf{x}_0, y) &= E^{(1)}(\mathbf{x}_0, y, \Upsilon_1(\mathbf{x}_0, y)) \\ &= \Upsilon_1(\mathbf{x}_0, y) \sqrt{\frac{h_{\mathcal{D}}(\Phi(\mathbf{x}_0, -\Upsilon_1(\mathbf{x}_0, y))) - h_{\mathcal{D}}(\mathbf{x}_0) + \Upsilon_1(\mathbf{x}_0, y) h_{\mathcal{P}}(\mathbf{x}_0)}{\Upsilon_1^2(\mathbf{x}_0, y)}} - y \end{aligned} \quad (2.82)$$

(cf. Eq. (2.66)). Equating with 0 all the partial derivatives of $E(\mathbf{x}_0, y)$ with respect to \mathbf{x}_0 and y evaluated at $\mathbf{x}_0 = \mathbf{x}_*$ and $y = 0$ it follows that

$$\begin{aligned} \Upsilon_{1,x}(\mathbf{x}_*, 0) &= \mathbf{0}, \\ \Upsilon_{1,y}(\mathbf{x}_*, 0) &= \sqrt{\frac{2}{a_*}} \end{aligned} \quad (2.83)$$

and thus

$$\Upsilon_1(\mathbf{x}_0, y) = \sqrt{\frac{2}{a_*}} y + \mathcal{O}(2), \quad (2.84)$$

where $\mathcal{O}(2)$ refers to terms that are at least quadratic in y and/or $\mathbf{x}_0 - \mathbf{x}_*$ and similarly below. Substitution into Eq. (2.63) yields

$$\begin{aligned}\tilde{\mathbf{X}}_{in}(\mathbf{x}_0, y) &= \Phi(\mathbf{x}_0, -\Upsilon_1(\mathbf{x}_0, y)) \\ &= \Phi(\mathbf{x}_*, 0) + \Phi_{,\mathbf{x}}(\mathbf{x}_*, 0) \cdot (\mathbf{x}_0 - \mathbf{x}_*) - \mathbf{f}(\mathbf{x}_*) \Upsilon_1(\mathbf{x}_0, y) + \mathcal{O}(2) \\ &= \mathbf{x}_* - \sqrt{\frac{2}{a_*}} \mathbf{f}(\mathbf{x}_*) y + (\mathbf{x}_0 - \mathbf{x}_*) + \mathcal{O}(2)\end{aligned}\quad (2.85)$$

Substitution into Eq. (2.64) yields

$$\begin{aligned}\tilde{\mathbf{X}}_{out}(\mathbf{x}_0, y) &= \mathbf{g}_D(\tilde{\mathbf{X}}_{in}(\mathbf{x}_0, y)) \\ &= \mathbf{g}_D(\mathbf{x}_*) + \mathbf{g}_{D,\mathbf{x}}(\mathbf{x}_*) \cdot (\tilde{\mathbf{X}}_{in}(\mathbf{x}_0, y) - \mathbf{x}_*) + \mathcal{O}(2)\end{aligned}\quad (2.86)$$

$$= \mathbf{x}_* - \mathbf{g}_{D,\mathbf{x}}(\mathbf{x}_*) \cdot \mathbf{f}(\mathbf{x}_*) \sqrt{\frac{2}{a_*}} y + \mathbf{g}_{D,\mathbf{x}}(\mathbf{x}_*) \cdot (\mathbf{x}_0 - \mathbf{x}_*) + \mathcal{O}(2)\quad (2.87)$$

Now consider the function

$$E(\mathbf{x}_0, y) = E^{(2)}(\tilde{\mathbf{X}}_{out}(\mathbf{x}_0, y), \Upsilon_2(\mathbf{x}_0, y)) = h_{\mathcal{P}}\left(\Phi\left(\tilde{\mathbf{X}}_{out}(\mathbf{x}_0, y), -\Upsilon_2(\mathbf{x}_0, y)\right)\right)\quad (2.88)$$

(cf. Eqs. (2.65) and (2.67)). Equating with 0 all the partial derivatives of $E(\mathbf{x}_0, y)$ with respect to \mathbf{x}_0 and y evaluated at $\mathbf{x}_0 = \mathbf{x}_*$ and $y = 0$ it follows that

$$\Upsilon_{2,\mathbf{x}}(\mathbf{x}_*, 0) = \frac{1}{a_*} h_{\mathcal{P},\mathbf{x}}(\mathbf{x}_*) \cdot \mathbf{g}_{D,\mathbf{x}}(\mathbf{x}_*),\quad (2.89)$$

$$\Upsilon_{2,y}(\mathbf{x}_*, 0) = -\sqrt{\frac{2}{a_*^3}} h_{\mathcal{P},\mathbf{x}}(\mathbf{x}_*) \cdot \mathbf{g}_{D,\mathbf{x}}(\mathbf{x}_*) \cdot \mathbf{f}(\mathbf{x}_*)\quad (2.90)$$

and thus

$$\Upsilon_2(\mathbf{x}_0, y) = \frac{1}{a_*} h_{\mathcal{P},\mathbf{x}}(\mathbf{x}_*) \cdot \mathbf{g}_{D,\mathbf{x}}(\mathbf{x}_*) \cdot (\mathbf{x}_0 - \mathbf{x}_*) - \sqrt{\frac{2}{a_*^3}} h_{\mathcal{P},\mathbf{x}}(\mathbf{x}_*) \cdot \mathbf{g}_{D,\mathbf{x}}(\mathbf{x}_*) \cdot \mathbf{f}(\mathbf{x}_*) y + \mathcal{O}(2).\quad (2.91)$$

Substitution into Eq. (2.65) yields

$$\begin{aligned}
\tilde{\mathbf{X}}_1(\mathbf{x}_0, y) &= \Phi\left(\tilde{\mathbf{X}}_{out}(\mathbf{x}_0, y), -\Upsilon_2(\mathbf{x}_0, y)\right) \\
&= \Phi(\mathbf{x}_*, 0) + \Phi_{,\mathbf{x}}(\mathbf{x}_*, 0)\left(\tilde{\mathbf{X}}_{out}(\mathbf{x}_0, y) - \mathbf{x}_*\right) - \mathbf{f}(\mathbf{x}_*)\Upsilon_2(\mathbf{x}_0, y) + \mathcal{O}(2) \\
&= \mathbf{x}_* + \left(\text{Id} - \frac{1}{a_*}\mathbf{f}(\mathbf{x}_*) \cdot h_{\mathcal{P},\mathbf{x}}(\mathbf{x}_*)\right) \left(\begin{bmatrix} \mathbf{g}_{\mathcal{D},\mathbf{x}}(\mathbf{x}_*) \cdot (\mathbf{x}_0 - \mathbf{x}_*) \\ -\sqrt{\frac{2}{a_*}} \cdot \mathbf{g}_{\mathcal{D},\mathbf{x}}(\mathbf{x}_*) \cdot \mathbf{f}(\mathbf{x}_*) y \end{bmatrix}\right) + \mathcal{O}(2).
\end{aligned} \tag{2.92}$$

By the smoothness of the global Poincaré map $\mathbf{P}_{\text{smooth}}$ polynomial approximations of $\mathbf{P}_{\text{smooth}}$ near any arbitrary point \mathbf{x} on its domain of definition may be obtained through the numerical solution of the associated variational equations (to whatever order necessary) along the trajectory through \mathbf{x} until the subsequent intersection with \mathcal{P} . In the case of local analysis in the vicinity of a periodic trajectory of Φ , the natural choice of \mathbf{x} is the unique intersection of the trajectory with \mathcal{P} . In contrast, in the case of a quasiperiodic trajectory of Φ , every neighborhood of a point of intersection with \mathcal{P} contains infinitely many additional points of intersection and no obvious choice of \mathbf{x} exists about which a local approximation should be derived. Possible schemes for making such choices, such as using the nearest point on the grazing trajectory, need to be balanced against the computational expense associated with each scheme.

2.5.4 Hybrid Dynamical Systems

In the case of a hybrid dynamical system, suppose, for example, that the j -th segment on a solution trajectory achieves grazing contact at a point \mathbf{x}_* with an event surface corresponding to an event function $h_{\mathbf{I}}$, where $\mathbf{I} \in \iota_{j-1}(\mathbf{x}_{j-1}(t_{j-1}))$ and $\mathbf{f}_{\mathbf{I}} = \mathbf{f}_{\mathbf{I}_j}$. Then, under suitable conditions, it is possible to replace the j -th segment and j -th index vector, with two segments $\mathbf{x}_{j'}$ and $\mathbf{x}_{j''}$ with index vectors $\mathbf{I}_{j'}$ and $\mathbf{I}_{j''}$, such that $h_{\mathbf{I}_{j'}} = h_{\mathbf{I},\mathbf{x}} \cdot \mathbf{f}_{\mathbf{I}}$, $h_{\mathbf{I}_{j''}} = h_{\mathbf{I}_j}$, $\mathbf{f}_{\mathbf{I}_{j'}} = \mathbf{f}_{\mathbf{I}_{j''}} = \mathbf{f}_{\mathbf{I}_j}$, $\mathbf{g}_{\mathbf{I}_{j''}} = \mathbf{g}_{\mathbf{I}_j}$ and where $\mathbf{g}_{\mathbf{I}_{j'}}$ is the discontinuity mapping obtained through the above construction. A hybrid flow map \mathbf{P}_{Σ} may again be constructed, but due to the

nondifferentiability of $\mathbf{g}_{\mathbf{I}_j'}$, the derivative $\mathbf{P}_{\Sigma, \mathbf{x}}$ no longer exists. Nevertheless, local analysis is possible through composition of series expansions as discussed above. An example of this construction may be found in Zhao *et al.* [53].

2.6 Local Stability

The stability of a solution trajectory corresponding to a given dynamical system is characterized by the behavior of its neighboring trajectories. In particular, a solution $\mathbf{x}(t)$ of a continuous-in-time dynamical system is said to be *stable in the Lyapunov sense* on the interval $[t_0, \infty)$ if for every $\epsilon > 0$, there exists a $\delta(\epsilon) > 0$, such that any other solution $\tilde{\mathbf{x}}(t)$ for which $\|\mathbf{x}(t_0) - \tilde{\mathbf{x}}(t_0)\| < \delta(\epsilon)$ satisfies $\|\mathbf{x}(t) - \tilde{\mathbf{x}}(t)\| < \epsilon$ for all $t \geq t_0$. Similarly, a solution \mathbf{x}_i of a discrete-in-time dynamical system is said to be *stable in the Lyapunov sense* on the interval $[k, \infty)$ if for every $\epsilon > 0$, there exists a $\delta(\epsilon) > 0$, such that any other solution $\tilde{\mathbf{x}}_i$ for which $\|\mathbf{x}_k - \tilde{\mathbf{x}}_k\| < \delta(\epsilon)$ satisfies $\|\mathbf{x}_i - \tilde{\mathbf{x}}_i\| < \epsilon$ for all $i \geq k$.

A solution that is not Lyapunov stable is said to be *unstable in the Lyapunov sense*. On the other hand, if in addition to being Lyapunov stable,

$$\lim_{t \rightarrow \infty} \|\mathbf{x}(t) - \tilde{\mathbf{x}}(t)\| = 0 \quad (2.93)$$

in the case of continuous-in-time dynamics or

$$\lim_{i \rightarrow \infty} \|\mathbf{x}_i - \tilde{\mathbf{x}}_i\| = 0 \quad (2.94)$$

in the case of discrete-in-time dynamics, the solution is said to be *asymptotically stable in the Lyapunov sense*.

A weaker definition of stability is that of *orbital stability* (or *stability in the Poincaré sense*). The solution $\mathbf{x}(t)$ of a continuous-in-time dynamical system is said to be orbitally stable on the interval $[t_0, \infty)$ if for every $\epsilon > 0$, there exists a $\delta(\epsilon) > 0$, such that any other solution $\tilde{\mathbf{x}}(t)$ for which $d(\tilde{\mathbf{x}}(t_0), \mathbf{x}([t_0, \infty))) < \delta(\epsilon)$ satisfies $d(\tilde{\mathbf{x}}(t), \mathbf{x}([t_0, \infty))) < \epsilon$ for all

$t \geq t_0$. Here, $d(\mathbf{y}, \mathbf{x}([t_0, \infty)))$ denotes the shortest distance between a point \mathbf{y} and the trajectory $\mathbf{x}(t)$. Similarly, a solution \mathbf{x}_i of a discrete-in-time dynamical system is said to be orbitally stable on the interval $[k, \infty)$ if for every $\epsilon > 0$, there exists a $\delta(\epsilon) > 0$, such that any other solution $\tilde{\mathbf{x}}_i$ for which $d(\tilde{\mathbf{x}}_k, \mathbf{x}_{[k, \infty)}) < \delta(\epsilon)$ satisfies $d(\tilde{\mathbf{x}}_i, \mathbf{x}_{[k, \infty)}) < \epsilon$ for all $i \geq k$.

A solution that is not orbitally stable is said to be *orbitally unstable*. On the other hand, if in addition to being orbitally stable,

$$\lim_{t \rightarrow \infty} d(\tilde{\mathbf{x}}(t), \mathbf{x}([t_0, \infty))) = 0 \quad (2.95)$$

in the case of continuous-in-time dynamics or

$$\lim_{i \rightarrow \infty} d(\tilde{\mathbf{x}}_i, \mathbf{x}_{[k, \infty)}) = 0 \quad (2.96)$$

in the case of discrete-in-time dynamics, the solution is said to be *orbitally asymptotically stable*.

2.6.1 Periodic Trajectories

Consider a periodic trajectory of a smooth/hybrid dynamical system with the corresponding hybrid flow map \mathbf{P}_Σ . Suppose that \mathbf{x}_* is the corresponding fixed point of \mathbf{P}_Σ , i.e., $\mathbf{P}_\Sigma(\mathbf{x}_*) = \mathbf{x}_*$. Then, the periodic trajectory is orbitally stable if and only if the fixed point \mathbf{x}_* is stable in the Lyapunov sense for the hybrid flow map. In particular, the fixed point \mathbf{x}_* is asymptotically stable in the Lyapunov sense if all eigenvalues of $\mathbf{P}_{\Sigma, \mathbf{x}}(\mathbf{x}_*)$ lie within the unit circle in the complex plane. In this case, the corresponding periodic trajectory is orbitally asymptotically stable and said to be a *limit cycle*. On the other hand, if at least one eigenvalue of $\mathbf{P}_{\Sigma, \mathbf{x}}(\mathbf{x}_*)$ lies outside the unit circle, then the fixed point is unstable in the Lyapunov sense and the periodic trajectory is orbitally unstable.

2.6.2 Quasiperiodic Trajectories

Consider quasiperiodic trajectory on a k -dimensional invariant torus and suppose that the trajectory intersects a suitable defined event surface transversely along a $k - 1$ -dimensional invariant torus of the corresponding Poincaré map \mathbf{P} . Then, the quasiperiodic trajectory is orbitally stable if and only if the $k - 1$ -dimensional invariant torus is orbitally stable for the Poincaré map \mathbf{P} and likewise for orbitally asymptotically stable.

2.6.3 Lyapunov Exponents

Lyapunov Exponents, also known as characteristic exponents, measure the average rate of local expansion or contraction of the deviation between a reference trajectory and any nearby trajectories. They are asymptotic quantities and describe the exponential rate at which a perturbation to a given trajectory of a system grows or decays with time [32]. Lyapunov exponents can be used to distinguish between a variety of steady state solutions such as equilibrium points, periodic trajectories, quasiperiodic trajectories, and chaotic motions. Table 2.1 shows Lyapunov exponents for a variety of orbitally stable steady state trajectories when the dynamical system is n -dimensional.

Table 2.1: Lyapunov Exponents for a variety of orbitally asymptotically stable steady-state trajectories [37].

Steady State	Flow	Lyapunov Exponents	Fractal Dimension
Periodic	circle	$\begin{pmatrix} \lambda_1 = 0 \\ 0 > \lambda_2 \geq \dots \geq \lambda_n \end{pmatrix}$	1
K-periodic	K-torus	$\begin{pmatrix} \lambda_1 = \dots \lambda_K = 0 \\ 0 > \lambda_{K+1} \geq \dots \geq \lambda_n \end{pmatrix}$	K
Chaotic	cantor-like	$\lambda_1 > 0; \sum \lambda_i < 0$	non-integer

Lyapunov Exponents for Discrete-in-time Dynamical Systems

Denote by \mathbf{x}_i , $i \in [k, \infty)$ a reference trajectory of a discrete-in-time dynamical system with map \mathbf{P} , i.e., $\mathbf{x}_{i+1} = \mathbf{P}(\mathbf{x}_i)$. Then, the j -th Lyapunov exponent of the reference trajectory under iterates of \mathbf{P} is defined as

$$\mu_j = \lim_{i \rightarrow \infty} \left| \lambda_j \left((\mathbf{P}^i)_{,\mathbf{x}}(\mathbf{x}_k) \right) \right|^{\frac{1}{i}}, \quad (2.97)$$

where $\lambda_j \left((\mathbf{P}^i)_{,\mathbf{x}}(\mathbf{x}_k) \right)$ is the j -th eigenvalue of the Jacobian of the i -th iterate of the map \mathbf{P} evaluated at \mathbf{x}_k , provided the limit exists [37]. In particular, for a fixed point \mathbf{x}_* of \mathbf{P} ,

$$(\mathbf{P}^i)_{,\mathbf{x}}(\mathbf{x}_*) = (\mathbf{P}_{,\mathbf{x}}(\mathbf{x}_*))^i \quad (2.98)$$

and thus

$$\lambda_j \left((\mathbf{P}^i)_{,\mathbf{x}}(\mathbf{x}_k) \right) = (\lambda_j(\mathbf{P}_{,\mathbf{x}}(\mathbf{x}_*)))^i. \quad (2.99)$$

It follows that

$$\mu_j = |\lambda_j(\mathbf{P}_{,\mathbf{x}}(\mathbf{x}_*))|. \quad (2.100)$$

Lyapunov Exponents for Continuous-in-time Dynamical Systems

Denote by $\mathbf{x}(t)$, $t \in [t_0, \infty)$ a reference trajectory of a continuous-in-time dynamical system with flow Φ , i.e., $\mathbf{x}(t) = \Phi(\mathbf{x}(t_0), t - t_0)$. Then, the j -th Lyapunov exponent of the reference trajectory under the flow Φ is defined as

$$\mu_j = \lim_{t \rightarrow \infty} \ln |\lambda_j(\Phi_{,\mathbf{x}}(\mathbf{x}(t_0), t - t_0))|^{\frac{1}{t}}, \quad (2.101)$$

where $\lambda_j(\Phi_{,\mathbf{x}}(\mathbf{x}(t_0), t - t_0))$ is the j -th eigenvalue of the Jacobian of the flow evaluated at $\mathbf{x}(t_0)$ and time t , provided the limit exists [37]. In particular, for a periodic trajectory of period T ,

$$\Phi_{,\mathbf{x}}(\mathbf{x}(t_0), kT) = (\Phi_{,\mathbf{x}}(\mathbf{x}(t_0), T))^k \quad (2.102)$$

and thus

$$\lambda_j(\Phi_{,\mathbf{x}}(\mathbf{x}(t_0), kT)) = (\lambda_j(\Phi_{,\mathbf{x}}(\mathbf{x}(t_0), T)))^k. \quad (2.103)$$

It follows that

$$\mu_j = \frac{1}{T} \ln |\lambda_j(\Phi_{,\mathbf{x}}(\mathbf{x}(t_0), T))|. \quad (2.104)$$

Even though Eq. (2.101) defines the Lyapunov exponents for continuous-in-time dynamical systems, using it to evaluate them in the case of chaotic systems becomes problematic. In such cases at least one of the Lyapunov exponents is positive, making $\Phi_{,\mathbf{x}}(\mathbf{x}(t_0), t - t_0)$ growing without bound as $t \rightarrow \infty$. This will lead to serious numerical problems in the integration of variational equations [37]. Hence, an alternative procedure to compute all the Lyapunov exponents using their fundamental definition from Eq.(2.101) is discussed below .

Consider the orthogonal matrix U_0 and let

$$V_{k+1} = \Phi_{,\mathbf{x}}(\mathbf{x}(t_0), \tau) \cdot U_k, \quad (2.105)$$

$$U_{k+1} = \mathbf{GS}(V_{k+1}), \quad (2.106)$$

where U_{k+1} is obtained from V_{k+1} through a column-by-column Gram-Schmidt orthogonalization. Let M_j^k be the magnitude of the j -th column of V_k . Then [32],

$$\lambda_j = \lim_{K \rightarrow \infty} \frac{1}{K\tau} \sum_{k=1}^K \ln M_j^k. \quad (2.107)$$

Lyapunov Exponents for Hybrid Dynamical Systems

Denote by ξ and Σ a reference trajectory and corresponding signature of a hybrid dynamical system. Let $\Sigma_{\uparrow i} = \{\mathbf{I}_1, \dots, \mathbf{I}_i\}$ be the subset of the first i elements of the signature. Then, the j -th Lyapunov exponent of the reference trajectory under the hybrid flow map \mathbf{P}_Σ is defined as

$$\mu_j = \lim_{i \rightarrow \infty} |\lambda_j(\mathbf{P}_{\Sigma_{\uparrow i}, \mathbf{x}}(\mathbf{x}_1(t_0)))|^{\frac{1}{i}}. \quad (2.108)$$

An alternative definition in terms of the flows $\Phi_{\mathbf{I}}$ is given by Eq. (2.101), where for

$t \in (t_{j-1}, t_j]$, $\Phi_{\mathbf{x}}(\mathbf{x}(t_0), t - t_0)$ is replaced with

$$\begin{aligned} & \Phi_{\mathbf{I}_j, \mathbf{x}}(\mathbf{g}_{\mathbf{I}_{j-1}}(\mathbf{x}_{j-1}(t_{j-1})), t - t_{j-1}) \\ & \cdot \left(\left[\begin{array}{c} \mathbf{g}_{\mathbf{I}_{j-1}, \mathbf{x}}(\mathbf{x}_{j-1}(t_{j-1})) \\ + \frac{(\mathbf{f}_{\mathbf{I}_j}(\mathbf{g}_{\mathbf{I}_{j-1}}(\mathbf{x}_{j-1}(t_{j-1}))) - \mathbf{g}_{\mathbf{I}_{j-1}, \mathbf{x}}(\mathbf{x}_{j-1}(t_{j-1})) \cdot \mathbf{f}_{\mathbf{I}_{j-1}}(\mathbf{x}_{j-1}(t_{j-1}))) \cdot h_{\mathbf{I}_{j-1}, \mathbf{x}}(\mathbf{x}_{j-1}(t_{j-1}))}{h_{\mathbf{I}_{j-1}, \mathbf{x}}(\mathbf{x}_{j-1}(t_{j-1})) \cdot \mathbf{f}_{\mathbf{I}_{j-1}}(\mathbf{x}_{j-1}(t_{j-1}))} \end{array} \right] \right) \\ & \cdot \Phi_{\mathbf{I}_{j-1}, \mathbf{x}}(\mathbf{g}_{\mathbf{I}_{j-2}}(\mathbf{x}_{j-2}(t_{j-2})), t_{j-1} - t_{j-2}), \end{aligned} \quad (2.109)$$

for $j \geq 3$, with

$$\begin{aligned} & \Phi_{\mathbf{I}_2, \mathbf{x}}(\mathbf{g}_{\mathbf{I}_1}(\mathbf{x}_1(t_1)), t - t_1) \\ & \cdot \left(\left[\begin{array}{c} \mathbf{g}_{\mathbf{I}_1, \mathbf{x}}(\mathbf{x}_1(t_1)) \\ + \frac{(\mathbf{f}_{\mathbf{I}_2}(\mathbf{g}_{\mathbf{I}_1}(\mathbf{x}_1(t_1))) - \mathbf{g}_{\mathbf{I}_1, \mathbf{x}}(\mathbf{x}_1(t_1)) \cdot \mathbf{f}_{\mathbf{I}_1}(\mathbf{x}_1(t_1))) \cdot h_{\mathbf{I}_1, \mathbf{x}}(\mathbf{x}_1(t_1))}{h_{\mathbf{I}_1, \mathbf{x}}(\mathbf{x}_1(t_1)) \cdot \mathbf{f}_{\mathbf{I}_1}(\mathbf{x}_1(t_1))} \end{array} \right] \right) \\ & \cdot \Phi_{\mathbf{I}_1, \mathbf{x}}(\mathbf{x}_1(t_0), t_1 - t_0) \end{aligned} \quad (2.110)$$

for $j = 2$, and by $\Phi_{\mathbf{I}_1, \mathbf{x}}(\mathbf{x}_1(t_0), t - t_0)$ for $j = 1$ (cf. Müller [30]).

2.7 Bifurcations

Structurally stable features of dynamical systems are those that are expected to persist on open sets in suitable spaces of vector fields. For example, as is well-known for smooth systems, conditions of hyperbolicity guarantee the persistence and retained stability characteristics of equilibria or periodic orbits under small variations in system parameters [22]. The loss of structural stability has implications both in terms of model uncertainty as well as, for example, in detecting and designing against catastrophic system failure [51].

When structural stability is lost on hypersurfaces of one dimension smaller than the dimension of the parameter space, one speaks of *co-dimension-one bifurcations*, namely changes in system features that can be observed under variations in a single system parameter. Saddle-node, period-doubling, secondary Hopf etc. are a few examples of co-dimension-one bifurcations.

Similarly, *co-dimension-two bifurcations* are those that would generally occur only under suitable simultaneous variations of two system parameters. As has been extensively explored over the past decades [21, 22], the associated co-dimension-two surfaces in parameter space serve as *organizing centers* for co-dimension-one bifurcations. Indeed, co-dimension-one bifurcation surfaces are often found emanating from the co-dimension-two surfaces in ways that are characteristic of some associated degeneracy at the corresponding point of origin in parameter space. Degenerate saddle-node and period-doublings and bifurcations involving cusps are example of these bifurcations.

In hybrid dynamical systems, as discussed in Chapter 1, the presence of a discontinuity surface in the associated state space, e.g., corresponding to the occurrence of impact, naturally induces a variety of co-dimension-one bifurcations. As was the case for smooth dynamical systems, a study of co-dimension-two grazing bifurcations would thus be expected to provide an understanding of the relationship between these different bifurcation scenarios. It would also lead to insight into the dynamical characteristics of impact oscillators away from the co-dimension-one grazing bifurcation surfaces.

As shown above, stability of a grazing periodic trajectory when ignoring the effects of the state function can to lowest-order be determined by the eigenvalues of the matrix $\mathbf{P}_{\text{smooth},\mathbf{x}}(\mathbf{x}_*)$. In contrast, as shown by Fredriksson and Nordmark [20], assuming that the grazing periodic trajectory is asymptotically stable when ignoring the state jump function, the stability properties of the grazing periodic trajectory in the presence of the state jump function is determined by the geometry of the sequence of vectors

$$\mathbf{v}_n = \mathbf{P}_{\text{smooth},\mathbf{x}}^n(\mathbf{x}_*) \cdot \beta, \quad (2.111)$$

where

$$\beta = \left(Id - \frac{1}{a_*} \mathbf{f}(\mathbf{x}_*) \cdot h_{\mathcal{D},\mathbf{x}}(\mathbf{x}_*) \right) \cdot \mathbf{g}_{\mathcal{D},\mathbf{x}}(\mathbf{x}_*) \cdot \mathbf{f}(\mathbf{x}_*). \quad (2.112)$$

Indeed, necessary conditions for the stability of the grazing periodic trajectory are that the sequence $\xi_n = h_{\mathcal{D},\mathbf{x}}(\mathbf{x}_*) \cdot \mathbf{v}_n$, $n = 1, \dots$ be positive and that this remains true when replacing $\mathbf{P}_{\text{smooth},\mathbf{x}}^n(\mathbf{x}_*)$ with any nearby matrix. Here, for small deviations from \mathbf{x}_* in the direction of

negative values of $h_{\mathcal{D}}$, the discontinuity mapping results in a large stretching in a direction given by the image of the vector β under the Jacobian $\mathbf{P}_{\text{smooth},\mathbf{x}}(\mathbf{x}_*)$. The positiveness of ξ thus implies that every trajectory that remains in the vicinity of the grazing periodic trajectory achieves at most one intersection with \mathcal{D} in the vicinity of \mathbf{x}_* . Therefore, in parameter space, $\xi_n = 0$ points correspond to co-dimension-two bifurcations that dictate the occurrence of qualitatively different grazing bifurcations.

Along with the co-dimension-two bifurcation points discussed above, impact oscillators also exhibit two other types of co-dimension-two bifurcations in the case of grazing periodic orbits. Specifically, if a parameter set corresponding to a grazing contact of a periodic orbit also happens to be a parameter set at which the same periodic orbit undergoes a saddle-node bifurcation then that set corresponds to a *grazing-fold* co-dimension-two bifurcation point. Similarly, if a parameter set corresponding to a grazing contact of a periodic orbit also happens to be a parameter set at which the same periodic orbit undergoes a period-doubling bifurcation then that set corresponds to a *grazing-flip* co-dimension-two bifurcation point.

Chapter 3

Grazing Bifurcations of Co-dimension-one Invariant Tori

Note: Parts of this chapter are reprinted from P. Thota and H. Dankowicz, “Continuous and discontinuous grazing bifurcations in impacting oscillators ”, *Physica D* 214 187–197 Copyright (2006) and P. Thota and H. Dankowicz, “Analysis of grazing bifurcations of quasiperiodic system attractors ”, *Physica D*, 220(2), pp. 163 – 174 Copyright (2006), with permission from Elsevier.

3.1 Introduction

Bifurcations in dynamical systems characterized by the disappearance of an attractor in the vicinity of an originally attracting motion under parameter variations are quite frequent in physical systems. Such qualitative changes are naturally of concern to engineering system designers since they might lead to steady state solutions *far away* from the desired motion. In smooth dynamical systems, examples of such bifurcations are the saddle-node or cyclic-fold bifurcations as well as subcritical pitchfork, period-doubling, and Hopf bifurcations. In

impact oscillators, such discontinuous changes in system response have been found to be associated with transitions between nonimpacting and impacting motion via grazing bifurcations. While the ‘instability’ associated with such loss of a local attractor is relatively weak in the smooth case (cf. the slow dynamics near a ghost solution in the saddle-node case or near the unstable limit cycle following a Neimark-Hopf bifurcation), in the impacting case, the dynamics are typically rapidly repelled from the neighborhood of the grazing motion.

The purpose of this chapter is to closely examine the conditions under which a local attractor persists near (not necessarily periodic) grazing trajectories corresponding to co-dimension-one invariant tori. Two example piecewise smooth dynamical systems are studied in the vicinity of a parameter value corresponding to grazing contact, establishing the phenomenology associated with grazing bifurcations in impacting systems. A local analysis based on the discontinuity-mapping approach is employed to derive a normal-form description of the dynamics near the grazing trajectory.

As discussed in Chapter 1, the discontinuity-mapping approach was used by Fredriksson & Nordmark [20] to establish conditions for the persistence or disappearance of a local attractor in the vicinity of a grazing *periodic* trajectory in terms of properties of the vector field, impact surface, and impact map in the vicinity of the point of grazing contact. However, no such conditions have been formulated in the past in the case of grazing bifurcations of quasiperiodic system attractors. One of the main goals of this dissertation is to lay the foundation for the construction of such conditions in the quasiperiodic case.

Previous studies [20] of grazing periodic trajectories state that the catastrophic loss of a local attractor and strong instability characteristic of grazing bifurcations are directly associated with the repeated application of a square-root term that appears to lowest order in the normal-form expansion for the discontinuity mapping. In this chapter the effect of the square-root term is studied in a general setting of grazing bifurcations of co-dimension-one invariant tori. Also, the results obtained from applying the discontinuity-mapping approach to the two examples are compared with those from direct numerical simulation of the original

dynamical system.

Note: In Chapters 3 and 4, the normal-form expansion for $\mathbf{g}_{\mathcal{P}}$ is presented to different orders of truncation for different dynamical systems. The order to which it is truncated is based on the analysis performed for each system.

3.2 Grazing Bifurcations of a Co-dimension-one Periodic Attractor

Consider the dynamical system governed by the vector field

$$\mathbf{f}(\mathbf{x}) = \begin{pmatrix} x^2 \\ -x^1 - x^2 \left((x^1)^2 - \mu \right) \end{pmatrix}, \quad (3.1)$$

event function $h_{\mathcal{D}}(\mathbf{x}) = d - x^1$ and jump function

$$\mathbf{g}_{\mathcal{D}}(\mathbf{x}) = \begin{pmatrix} x^1 \\ -rx^2 \end{pmatrix}, \quad (3.2)$$

where $d, r > 0$ and μ are system parameters. In particular, for $r = 0.8$, $d \approx 2.0086\dots$, and $\mu = \mu_* = 1$, numerical integration shows the existence of a point $\mathbf{x}_* = \begin{pmatrix} d & 0 \end{pmatrix}^T$ corresponding to the intersection of a periodic trajectory with \mathcal{D}^0 , such that $a_* = d > 0$. Fig. 3.1 shows a grazing periodic trajectory corresponding to $\mu = \mu_* = 1$.

Applying the discontinuity-mapping methodology from the previous chapter to the dynamical system discussed in Eq. (3.1) and truncating the expansion at order $\frac{3}{2}$, we have

$$\mathbf{g}_{\mathcal{P}}(\mathbf{x}) = \mathbf{x}_* + \begin{cases} \begin{pmatrix} \mathbf{x} - \mathbf{x}_* \\ r^2(x^1 - d) + r^2\sqrt{\frac{2}{d}}(d^2 - \mu_*)\left(\frac{2}{3} + r\right)(x^1 - d)^{\frac{3}{2}} \end{pmatrix} & d - x^1 \geq 0 \\ 0 & d - x^1 < 0 \end{cases} \quad (3.3)$$

A notable feature of $\mathbf{g}_{\mathcal{P}}(\mathbf{x})$ in this case is the absence of a square-root term to lowest order. As will be seen in the later parts of this dissertation, this feature plays an important

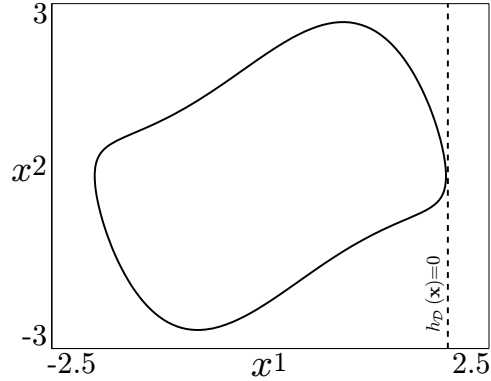


Figure 3.1: Grazing periodic orbit corresponding to the dynamical system given by Eq. (3.1). Here, $\mu = 1$ and the discontinuity surface $h_{\mathcal{D}}(\mathbf{x}) = 0$ can also be seen as a dotted line at $x^1 = d$.

role in the dynamics of the impacting motion. Indeed, not only the presence of a square-root term but also its orientation has serious implications on the stability characteristics of the ensuing impacting motion.

It follows that, to order $\frac{3}{2}$, the composite Poincaré map corresponding to the Poincaré section $\mathcal{P} = \{\mathbf{x} \mid h_{\mathcal{P}}(\mathbf{x}) \stackrel{\text{def}}{=} -x^2 = 0\}$ is given by

$$\begin{aligned} \mathbf{P}(\mathbf{x}) &= \mathbf{x}_* + \mathbf{P}_{\text{smooth},\mu}(\mathbf{x}_*)(\mu - \mu_*) \\ &+ \mathbf{P}_{\text{smooth},\mathbf{x}}(\mathbf{x}_*) \cdot \begin{cases} \begin{pmatrix} \mathbf{x} - \mathbf{x}_* & d - x^1 \geq 0 \\ r^2(x^1 - d) + r^2\sqrt{\frac{2}{d}}(d^2 - \mu_*)(x^1 - d)^{\frac{3}{2}} & d - x^1 < 0 \\ 0 \end{pmatrix} \end{cases}, \end{aligned} \quad (3.4)$$

where

$$\mathbf{P}_{\text{smooth},\mathbf{x}}(\mathbf{x}_*) = \begin{pmatrix} * & * \\ 0 & 0 \end{pmatrix} \text{ and } \mathbf{P}_{\text{smooth},\mu} = \begin{pmatrix} * \\ 0 \end{pmatrix} \quad (3.5)$$

and $*$ refers to a nonzero entry.

It follows that, to lowest order, a fixed point $\mathbf{x}_{\text{fp-imp}} = (x_{\text{fp}}^1, 0)^T$ of $\mathbf{P}(\mathbf{x})$ corresponding to an impacting periodic trajectory can be obtained as follows. Since $\mathbf{x}_{\text{fp-imp}}$ is the fixed point

of the map \mathbf{P} , its first component x_{fp}^1 satisfies

$$x_{\text{fp}}^1 = x_*^1 + \mathbf{P}_{\text{smooth},1}^1(\mathbf{x}_*) [r^2 (x_{\text{fp}}^1 - x_*^1)] + P_{\text{smooth},\mu}^1(\mathbf{x}_*) (\mu - \mu_*). \quad (3.6)$$

After algebraic manipulation, we have

$$x_{\text{fp}}^1 = d + \frac{P_{\text{smooth},\mu}^1(\mathbf{x}_*) (\mu - \mu_*)}{1 - r^2 \mathbf{P}_{\text{smooth},1}^1(\mathbf{x}_*)},$$

and the fixed point $\mathbf{x}_{\text{fp-imp}}$ is given by

$$\mathbf{x}_{\text{fp-imp}} = \begin{pmatrix} d + \frac{P_{\text{smooth},\mu}^1(\mathbf{x}_*) (\mu - \mu_*)}{1 - r^2 \mathbf{P}_{\text{smooth},1}^1(\mathbf{x}_*)} \\ 0 \end{pmatrix} \quad (3.7)$$

if

$$\frac{P_{\text{smooth},\mu}^1(\mathbf{x}_*) (\mu - \mu_*)}{1 - r^2 \mathbf{P}_{\text{smooth},1}^1(\mathbf{x}_*)} > 0. \quad (3.8)$$

Similarly, a fixed point $\mathbf{x}_{\text{fp-nonimp}}$ of $\mathbf{P}(\mathbf{x})$ corresponding to a nonimpacting periodic trajectory is given by

$$\mathbf{x}_{\text{fp-nonimp}} = \begin{pmatrix} d + \frac{P_{\text{smooth},\mu}^1(\mathbf{x}_*) (\mu - \mu_*)}{1 - P_{\text{smooth},1}^1(\mathbf{x}_*)} \\ 0 \end{pmatrix} \quad (3.9)$$

if

$$\frac{P_{\text{smooth},\mu}^1(\mathbf{x}_*) (\mu - \mu_*)}{1 - P_{\text{smooth},1}^1(\mathbf{x}_*)} \leq 0. \quad (3.10)$$

Here, we see that for a particular value of μ , the expressions $(1 - r^2 P_{\text{smooth},1}^1(\mathbf{x}_*))$ and $(1 - P_{\text{smooth},1}^1(\mathbf{x}_*))$ must have the same sign for only one of the fixed points ($\mathbf{x}_{\text{fp-imp}}$ or $\mathbf{x}_{\text{fp-nonimp}}$) to exist. Opposite signs for $(1 - r^2 P_{\text{smooth},1}^1(\mathbf{x}_*))$ and $(1 - P_{\text{smooth},1}^1(\mathbf{x}_*))$ indicate co-existence of impacting and nonimpacting fixed points or absence of both fixed points marking the grazing bifurcation discontinuous for a particular value of μ .

Hence, a discontinuous bifurcation results when

$$(1 - r^2 P_{\text{smooth},1}^1(\mathbf{x}_*)) (1 - P_{\text{smooth},1}^1(\mathbf{x}_*)) < 0 \quad (3.11)$$

while

$$(1 - r^2 P_{\text{smooth},1}^1(\mathbf{x}_*)) (1 - P_{\text{smooth},1}^1(\mathbf{x}_*)) > 0 \quad (3.12)$$

guarantees a continuous grazing bifurcation. For the numerical example discussed in Section 3.2, we have

$$(1 - r^2 P_{\text{smooth},1}^1(\mathbf{x}_*)) (1 - P_{\text{smooth},1}^1(\mathbf{x}_*)) = 0.9986, \quad (3.13)$$

As shown in Fig. 3.2, for $\mu \approx \mu_*$, direct numerical integration (left panel) and application of the composite map (right panel) show the existence of a unique locally attracting periodic trajectory emanating from and in the immediate vicinity of the grazing periodic trajectory with negative penetration for $\mu < \mu_*$ and positive penetration for $\mu > \mu_*$. Indeed, to lowest order the penetration is a linear function of the deviation $\mu - \mu_*$ although a more careful study shows that the slope is different for $\mu > \mu_*$ than for $\mu < \mu_*$. Hence, the bifurcation is in agreement with the definition of a *continuous grazing bifurcation*.

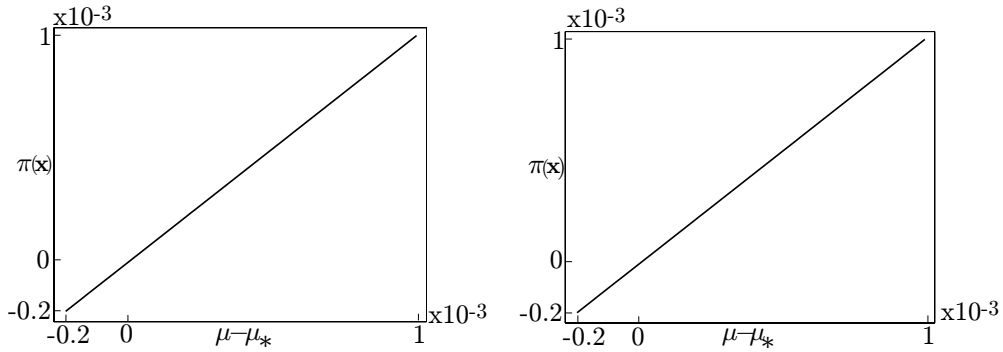


Figure 3.2: Bifurcation diagrams showing the penetration $\pi(\mathbf{x})$ as a function of $\mu - \mu_*$ obtained using direct numerical simulation of the original dynamical system (left panel) and the composite Poincaré map truncated at order $\frac{3}{2}$ (right panel). Excellent agreement between the two methods is evident in the figure. Also, note that the slope of the curve for $\mu > \mu_*$, even though not obvious from the figure, is different than that for $\mu < \mu_*$.

Linear theory can be applied to study the stability of the fixed points of the impacting motion given by Eq. (3.7). In order for the impacting motion to be stable, the eigenvalues of the Jacobian of the composite Poincaré map evaluated at those fixed points must lie within the unit circle in the complex plane. The Jacobian of the composite Poincaré map, including

the variations in the parameter μ , has the form

$$\mathbf{P}_{,\mathbf{x}}(\mathbf{x}_*) = \begin{pmatrix} \lambda_1 & * & * \\ 0 & 0 & 0 \\ 0 & 0 & 1 \end{pmatrix} \quad (3.14)$$

where $\lambda_1 = 0.000859r^2 \left(1 + \sqrt{\frac{2}{d}}(d^2 - \mu_*)(1 + \frac{3r}{2})(\mathbf{x}_{\text{fp-imp}}^1 - d)^{\frac{1}{2}}\right)$ is the nontrivial eigenvalue.

Fig. 3.3 shows the variation of λ_1 under changes in μ obtained from the composite Poincaré map (dotted line) and in close agreement with the results of direct numerical integration (solid line). In particular, we observe a discrete jump in the eigenvalue at $\mu = \mu_*$ and a square-root type behavior for $\mu > \mu_*$ as follows from the presence of the order $\frac{3}{2}$ term in the composite Poincaré map (Eq. (3.4)).

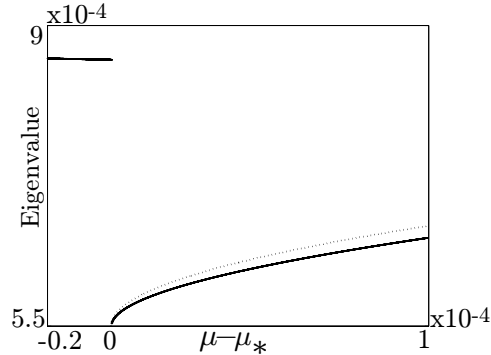


Figure 3.3: Nontrivial eigenvalue as a function of $\mu - \mu_*$ predicted using direct numerical simulation of the original dynamical system (solid line) and the composite Poincaré map truncated at order $\frac{3}{2}$ (dotted). The agreement between the two cases is seen to deviate as $\mu - \mu_* > 0$ increases.

Here, due to the absence of the square-root term the dynamics are governed by a piecewise linear map. In such cases the persistence of a local attractor can be analyzed using the theory of *border-collision bifurcations* where a fixed point of a linear map crosses a boundary into a region where the dynamics are governed by another linear map. Hassouneh *et al.* [23]

studied such bifurcations and concluded that even when both linear maps have locally asymptotically stable fixed points in their respective regions of validity, the system could have unbounded solutions at the point where the fixed point grazes the boundary. This occurs due to the reduction of the basin of attraction corresponding to each of the fixed points to a single point in state space at the parameter value corresponding to the grazing contact.

3.3 Grazing Bifurcations of a Co-dimension-one Torus Attractor

As a second example, consider the dynamical system given by the vector field

$$\mathbf{f}(\mathbf{x}) = \begin{pmatrix} x^2 \\ -x^1 - cx^2 \left((x^1)^2 - 1 \right) + A \cos x^3 \\ \omega \end{pmatrix} \quad (3.15)$$

in terms of the state vector

$$\mathbf{x} = \begin{pmatrix} x^1 & x^2 & x^3 \end{pmatrix}^T \in \mathbb{R}^2 \times \mathbb{S}^1, \quad (3.16)$$

the event function $h_{\mathcal{D}}(\mathbf{x}) = \mu - x^1$ (and, consequently, $h_{\mathcal{P}}(\mathbf{x}) = -x^2$), and associated jump map

$$\mathbf{g}_{\mathcal{D}}(\mathbf{x}) = \begin{pmatrix} x^1 \\ -rx^2 \\ x^3 \end{pmatrix}, \quad (3.17)$$

where $c, A, \omega, r > 0$ and μ are system parameters. In particular, for $c = 0.1$, $A = 0.75$, $\omega = 1.505$, $r = 0.8$, and $\mu = \mu_* = 2.4053 \dots$, numerical integration shows the existence of a grazing event at $\mathbf{x}_* = \begin{pmatrix} 2.4053 \dots & 0 & 2.9235 \dots \end{pmatrix}^T$ corresponding to the tangential intersection of a quasiperiodic trajectory with \mathcal{D}^0 , such that $a_* = x_*^1 - A \cos x_*^3 > 0$.

To linear order and with four significant digits, the discontinuity map corresponding to $\mathcal{P} = \{\mathbf{x} \mid h_{\mathcal{P}}(\mathbf{x}) = 0\}$ obtained using the methodology from the previous chapter takes the

form

$$\mathbf{g}_{\mathcal{P}}(\mathbf{x}) = \mathbf{x}_* + \begin{cases} \begin{pmatrix} \mathbf{x} - \mathbf{x}_*, \\ -0.3600(x^1 - \mu) + (x^1 - x_*^1) \\ 0 \end{pmatrix}, & \mu - x^1 \geq 0 \\ \begin{pmatrix} -2.1628\sqrt{x^1 - \mu} + (x^3 - x_*^3) - 0.2689(x^1 - \mu) \end{pmatrix}, & \mu - x^1 < 0 \end{cases} \quad (3.18)$$

As shown in Fig. 3.4, the intersection of the quasiperiodic trajectory with \mathcal{P} is an invariant curve Γ given by $x^1 = \gamma(x^3)$ for $x^3 \in \mathbb{S}^1$. For every point $\mathbf{x} \in \mathcal{P}$ in the vicinity of this curve, define the projection

$$\pi_{\Gamma}(\mathbf{x}) = \begin{pmatrix} \gamma(x^3) \\ 0 \\ x^3 \end{pmatrix}. \quad (3.19)$$

The smooth Poincaré map $\mathbf{P}_{\text{smooth}}$ can then be approximated on a neighborhood of Γ by the following linear approximation

$$\mathbf{P}_{\text{smooth}}(\mathbf{x}) = \mathbf{P}_{\text{smooth}}(\pi_{\Gamma}(\mathbf{x})) + \mathbf{P}_{\text{smooth},1}(\pi_{\Gamma}(\mathbf{x}))(x^1 - \gamma(x^3)), \quad (3.20)$$

where

$$\mathbf{P}_{\text{smooth},1}(\pi_{\Gamma}(\mathbf{x})) = \begin{pmatrix} * \\ 0 \\ * \end{pmatrix} \quad (3.21)$$

and $*$ refers to nontrivial entries. For purposes of simulation of the composite Poincaré map γ , $\mathbf{P}_{\text{smooth}}(\pi_{\Gamma}(\mathbf{x}))$, and $\mathbf{P}_{\text{smooth},1}(\pi_{\Gamma}(\mathbf{x}))$ are approximated by evaluating these at a finite subset of points on Γ and subsequently using interpolation to extend these results to the entire curve Γ .

An example of the predictive power of the approximate composite Poincaré map derived here can be seen in Figs. 3.5 and 3.6. Also, Fig. 3.7 shows the corresponding Lyapunov exponents for the bifurcation diagrams shown in Fig. 3.6. Clearly, for larger deviations in the value of μ away from μ_* , the approximate composite Poincaré map fails to adequately capture the asymptotic system response, although the predicted bifurcation diagram still

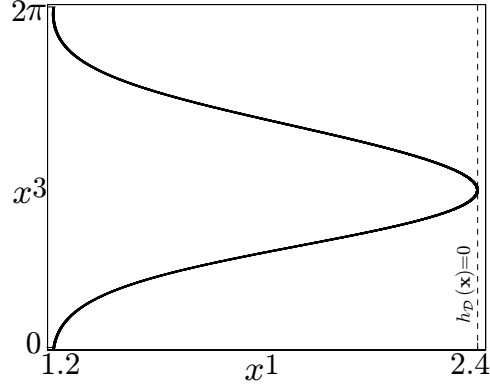


Figure 3.4: Invariant curve corresponding to the intersection of the trajectories with the Poincaré section $h_{\mathcal{P}} = 0$ for the system given in Eq. (3.15). The discontinuity surface $h_{\mathcal{D}} = 0$ is also shown(dotted line).

retains some features of the original system. To lowest-order in the deviation from \mathbf{x}_* , $\mathbf{g}_{\mathcal{P}}(\mathbf{x}) - \mathbf{x}_*$ is tangential to Γ . Moreover, by the invariance of Γ , this property persists to lowest-order under application of $\mathbf{P}_{\text{smooth}}$. Since the lowest-order term is proportional to the square-root in the deviation of \mathbf{x} from \mathbf{x}_* , it follows that the tangential dynamics in a direction along Γ dominate those in directions away from Γ , for which the dynamics are to lowest order linear. Under the assumption that a recurrent attractor persists in the immediate vicinity of the grazing quasiperiodic trajectory under small variations in system parameter values, it appears reasonable to consider a reduced composite Poincaré map to describe the tangential dynamics alone.

To this end, consider the composition

$$x^3 \mapsto (\mathbf{P}_{\text{smooth}} \circ \pi_{\Gamma} \circ \mathbf{g}_{\mathcal{P}})^3 \begin{pmatrix} \gamma(x^3) \\ 0 \\ x^3 \end{pmatrix}, \quad (3.22)$$

where the superscript on the right-hand side refers to the third component of the vector-

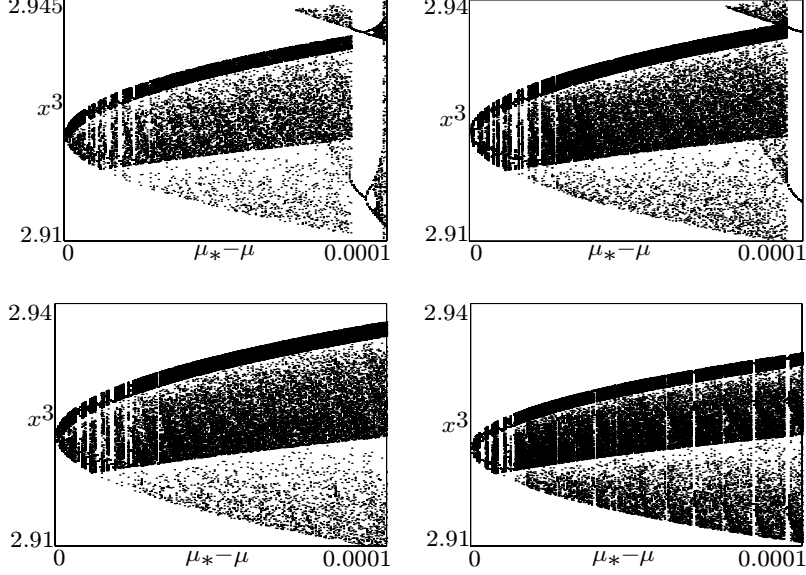


Figure 3.5: Bifurcation diagrams based on the \mathcal{P} Poincaré section obtained under small variations in the deviation $\mu_* - \mu$ using numerical simulation of the original dynamical system (upper-left panel), iteration of the full composite map (2.80) (upper-right panel), reduced composite map (3.22) (lower-left panel), and reduced map with parabolic approximation for Γ near \mathbf{x}_* (3.27) (lower-right panel). Here and in the following graphs, only points of intersection with the corresponding Poincaré section with positive penetration are shown.

valued map. For $\mathbf{x} \in \Gamma$ near \mathbf{x}_* , we have

$$\begin{aligned} \gamma(x^3) &\approx \gamma(x_*^3) + \gamma'(x_*^3)(x^3 - x_*^3) + \frac{1}{2}\gamma''(x_*^3)(x^3 - x_*^3)^2 \\ &= x_*^3 + \frac{1}{2}\gamma''(x_*^3)(x^3 - x_*^3)^2, \end{aligned} \quad (3.23)$$

since $\gamma'(x_*^3) = 0$ follows from the tangential contact of Γ with \mathcal{D} . Under the assumption that $\gamma''(x_*^3) < 0$,

$$h_{\mathcal{D}}(\mathbf{x}) < 0$$

for $\mathbf{x} \in \Gamma$ as long as

$$x_*^3 - \sqrt{2 \frac{\mu_* - \mu}{|\gamma''(x_*^3)|}} \approx x_{\min}^3 < x^3 < x_{\max}^3 \approx x_*^3 + \sqrt{2 \frac{\mu_* - \mu}{|\gamma''(x_*^3)|}} \quad (3.24)$$

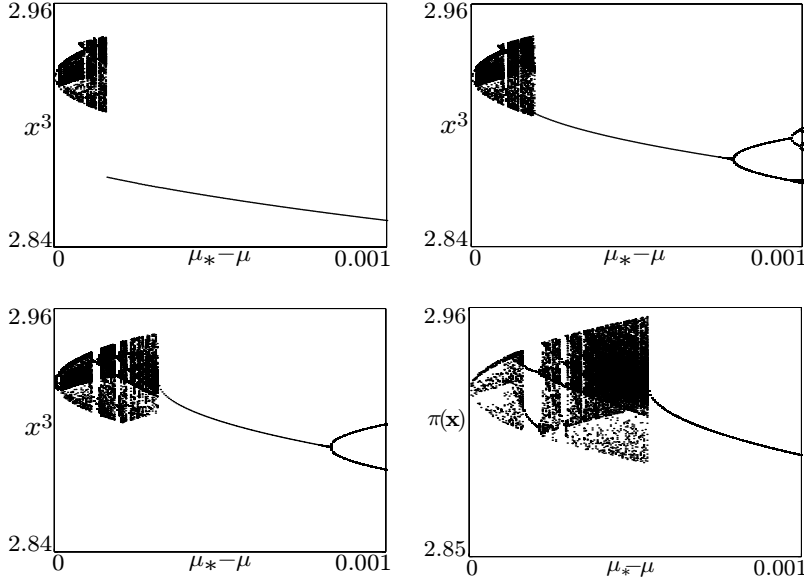


Figure 3.6: Bifurcation diagrams based on the \mathcal{P} Poincaré section obtained under variations in the deviation $\mu_* - \mu$ using numerical simulation of the original dynamical system (upper-left panel), and iteration of the full composite map (2.80) (upper-right panel), the reduced composite map (3.22) (lower-left panel) and reduced map with parabolic approximation for Γ near \mathbf{x}_* (3.27) (lower-right panel). These graphs compare the accuracy of the different levels of approximation involved in predicting the impacting dynamics for larger values of $\mu_* - \mu$ than Fig. 3.5. It is to be noticed that in the above graphs the full composite Poincaré map predicts impacting dynamics that match well with numerical simulation of the original dynamical system.

and $\mu < \mu_*$. In this case, substituting Eq. (3.23) into Eq. (3.18) and considering the third component, we have

$$\begin{aligned}
 (\mathbf{g}_{\mathcal{P}})^3(\mathbf{x}) &= x_*^3 - 2.1628\sqrt{x^1 - \mu} + x^3 - x_*^3 \\
 &= x^3 - 2.1628\sqrt{\mu_* + \frac{1}{2}\gamma''(x_*^3)(x^3 - x_*^3)^2 - \mu} \\
 &= x^3 - 2.1628\sqrt{\mu_* - \mu} \sqrt{1 - \frac{(x^3 - x_*^3)^2}{\frac{2(\mu_* - \mu)}{|\gamma''(x_*^3)|}}}, \tag{3.25}
 \end{aligned}$$

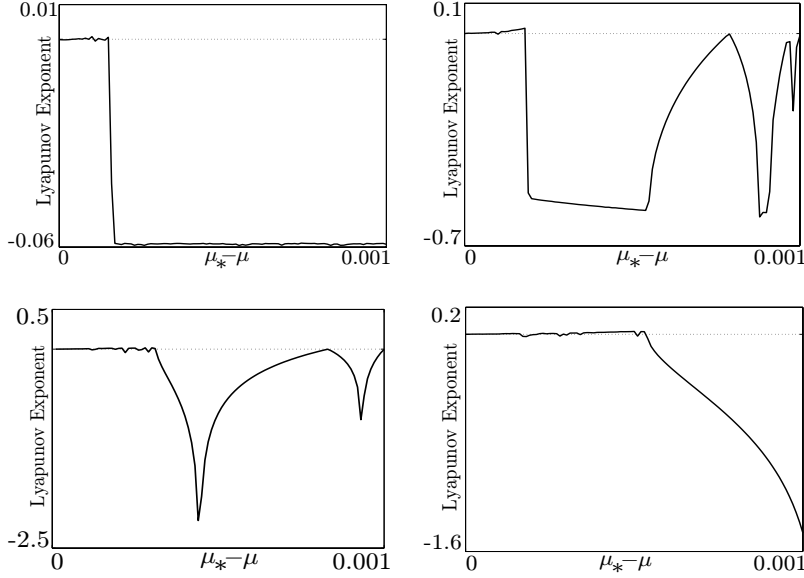


Figure 3.7: Nontrivial Lyapunov exponent corresponding to the impacting motion obtained under variations in the deviation $\mu_* - \mu$ using numerical simulation of the original dynamical system (upper-left panel), and iteration of the full composite map (2.80) (upper-right panel), the reduced composite map (3.22) (lower-left panel) and reduced map with parabolic approximation for Γ near \mathbf{x}_* (3.27) (lower-right panel). Note that for small values of $\mu_* - \mu$ the Lyapunov exponent in all the above graphs oscillates about 0 indicating existence of weakly chaotic and periodic windows (cf. Fig. 3.6). It is also evident that as the approximation level increases the weakly chaotic and periodic window behavior persists for larger values of $\mu_* - \mu$.

whereas $\mathbf{g}_{\mathcal{P}}$ is the identity for all other $\mathbf{x} \in \Gamma$. Let

$$f(x^3) = (\mathbf{P}_{\text{smooth}})^3 \begin{pmatrix} \gamma(x^3) \\ 0 \\ x^3 \end{pmatrix}. \quad (3.26)$$

Then, to lowest order the reduced map (3.22) is given by

$$x^3 \mapsto \begin{cases} f(x^3), & x^3 \notin (x_{\min}^3, x_{\max}^3) \\ f\left(x^3 - \rho_1 \sqrt{1 - \frac{(x^3 - x_*^3)^2}{\rho_2^2}}\right), & x^3 \in [x_{\min}^3, x_{\max}^3] \end{cases} \quad (3.27)$$

where

$$\rho_1 = 2.1628\sqrt{(\mu_* - \mu)} \quad (3.28)$$

and

$$\rho_2 = \sqrt{\frac{2(\mu_* - \mu)}{|\gamma''(x_*^3)|}}. \quad (3.29)$$

For numerical simulation purposes, $\gamma''(x_*^3)$ is approximate by the curvature of a parabola fitted to Γ in the vicinity of the grazing point \mathbf{x}_* .

Fig. 3.8 shows a comparison between the graph of the second iterate of the reduced composite map (3.22) for two different values of $\mu_* - \mu$ and the projection onto the third component of the second iterate of the full composite Poincaré map (2.80) evaluated for points on the corresponding system attractor. In both cases, the correction to the graph of the smooth function $f(f(x^3))$ is localized near x_*^3 and $f(x_*^3)$.

As shown in the upper panel of Fig. 3.9, for the first iterate, the correction to the graph of the smooth function $f(x^3)$ is localized near x_*^3 and the difference,

$$\begin{aligned} d &\stackrel{\text{def}}{=} f\left(x^3 - \rho_1 \sqrt{1 - \frac{(x^3 - x_*^3)^2}{\rho_2^2}}\right) - f(x^3) \\ &\approx f(x^3) - f'(x_*^3) \rho_1 \sqrt{1 - \frac{(x^3 - x_*^3)^2}{\rho_2^2}} - f(x^3) \\ &= -f'(x_*^3) \rho_1 \sqrt{1 - \frac{(x^3 - x_*^3)^2}{\rho_2^2}} \end{aligned} \quad (3.30)$$

for $x^3 \approx x_*^3$ takes the form of a semi-ellipse with half-height $f'(x_*^3) \rho_1$ and half-width ρ_2 both proportional to $\sqrt{\mu_* - \mu}$. However, in the case of the second iterate, the correction to the graph of the smooth function $f(f(x^3))$ is localized near x_*^3 and $f(x_*^3)$ and the difference

(using Eq.(3.30) and series expansions),

$$\begin{aligned}
d &= f \left(f \left(x^3 - \rho_1 \sqrt{1 - \frac{(x^3 - x_*^3)^2}{\rho_2^2}} \right) \right) - f(f(x^3)) \\
&\approx f \left(f(x^3) - f'(x_*^3) \rho_1 \sqrt{1 - \frac{(x^3 - x_*^3)^2}{\rho_2^2}} \right) - f(f(x^3)) \\
&\approx f(f(x^3)) - f'(f(x_*^3)) f'(x_*^3) \rho_1 \sqrt{1 - \frac{(x^3 - x_*^3)^2}{\rho_2^2}} - f(f(x^3)) \\
&= -f'(f(x_*^3)) f'(x_*^3) \rho_1 \sqrt{1 - \frac{(x^3 - x_*^3)^2}{\rho_2^2}} \tag{3.31}
\end{aligned}$$

for $x^3 \approx x_*^3$ takes the form of a semi-ellipse, as shown in Fig. 3.9 (right panel), with half-height $f'(f(x_*^3)) f'(x_*^3) \rho_1$ and half-width ρ_2 both proportional to $\sqrt{\mu_* - \mu}$. In the derivation of the above Eq. (3.31) it is assumed that an application of f to points in the vicinity of the grazing point results in $f(x^3)$ that are far away from grazing and no correction is needed to apply the Poincaré map to these resulting points.

From the upper panel of Fig. 3.8, it follows that for some critical value of $\mu_* - \mu$, a tangential intersection occurs between the graph of the reduced composite map and the identity line, corresponding to the birth of a pair of period-2 orbits of the reduced composite map in a saddle-node bifurcation. Although the reduced composite map only approximately captures the near-grazing dynamics (note, e.g., its failure to predict the extra branch of the correction obtained for $\mu_* - \mu = 15 \times 10^{-5}$), it is nevertheless able to provide qualitative insight into the bifurcation behavior of the original dynamical system (see, e.g., the birth of a period-2 orbit for $\mu_* - \mu \approx 2 \times 10^{-4}$ in Fig. 3.6).

Finally, consider the constant-phase Poincaré section $\mathcal{P}' = \{\mathbf{x} \mid x^3 = x_*^3\}$. Then, to linear order and with four significant digits, the discontinuity map corresponding to \mathcal{P}' obtained

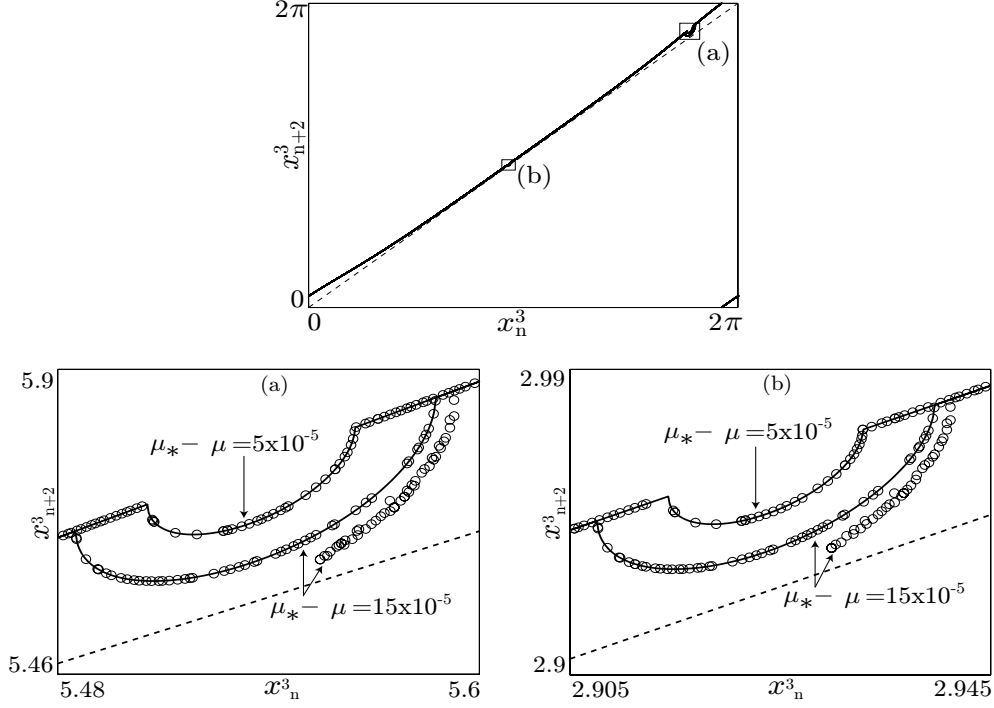


Figure 3.8: (Upper panel and blow-ups of regions (a) and (b) in bottom panels) A comparison between the graph of the second iterate of the reduced map (3.22) (solid curve) for $\mu_* - \mu = 5 \times 10^{-5}$ and $\mu_* - \mu = 15 \times 10^{-5}$ and the projection onto the third component of the second iterate of the full composite Poincaré map (2.80) (circles) evaluated for points on the corresponding system attractor.

using the methodology in Chapter 2 takes the form

$$\mathbf{g}_{\mathcal{P}'}(\mathbf{x}) = \mathbf{x}_* + \begin{cases} \begin{pmatrix} \mathbf{x} - \mathbf{x}_*, \\ -2.5998(x^1 - \mu) \\ -4.5089\sqrt{x^1 + 0.1593(x^2)^2 - \mu} \\ +1.2985(x^1 - \mu) + x^2 \\ 0 \end{pmatrix}, & h_{\mathcal{D}}(\mathbf{X}_0(\mathbf{x})) \geq 0 \\ \begin{pmatrix} \mathbf{x} - \mathbf{x}_*, \\ -2.5998(x^1 - \mu) \\ -4.5089\sqrt{x^1 + 0.1593(x^2)^2 - \mu} \\ +1.2985(x^1 - \mu) + x^2 \\ 0 \end{pmatrix}, & h_{\mathcal{D}}(\mathbf{X}_0(\mathbf{x})) < 0 \end{cases} \quad (3.32)$$

Bifurcation diagrams obtained under variations in $\mu_* - \mu$ using numerical simulation of the original dynamical system (left panel) and the composite map (2.81) (right panel) are shown in Fig. 3.10. This appears to indicate that better fidelity over a larger range of values of μ is possible using the Poincaré section \mathcal{P}' than with \mathcal{P} .

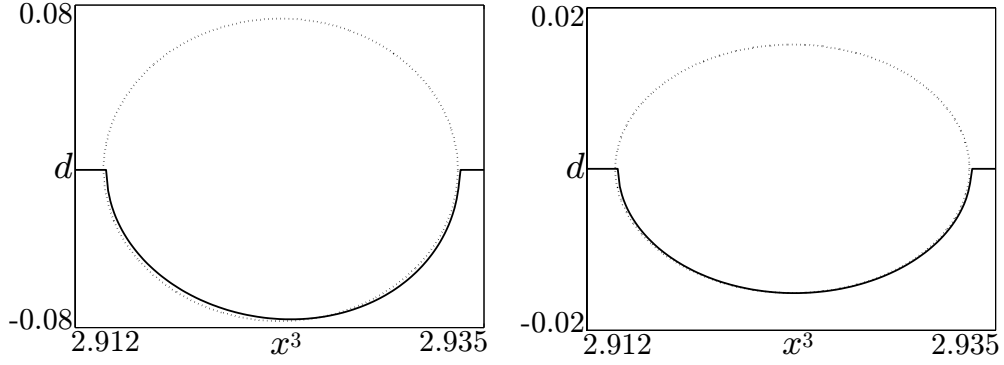


Figure 3.9: (Left panel) The difference between $f(x^3)$ and the reduced composite map (3.22) (solid curve) on a neighborhood of x_*^3 compared with an ellipse (dotted) centered at x_*^3 with half-height $f'(x_*^3)\rho_1$ and half-width ρ_2 , where ρ_1 and ρ_2 are given by (3.28) and (3.29) as predicted by (3.30). Similarly, in the right panel the difference between $f(f(x^3))$ and the second iterate of the reduced map on a neighborhood of x_*^3 is shown. Here, $f'(x_*^3) \approx 5.0164$ and $f'(f(x_*^3)) \approx 0.2013$.

The intersection of the grazing quasiperiodic trajectory with \mathcal{P}' is a closed invariant curve Γ' , shown in Fig. 3.11 (left panel), parameterized in a one-to-one fashion by $\begin{pmatrix} x^1 & x^2 \end{pmatrix}^T = \gamma(t)$ for $t \in [-\pi, \pi)$. For every point $\mathbf{x} \in \mathcal{P}'$ in the vicinity of this curve, define the projection $\pi'_{\Gamma'}(\mathbf{x})$ from \mathbf{x} to some point on Γ' , for example the closest point in some chosen metric. The smooth Poincaré map $\mathbf{P}'_{\text{smooth}}$ can then be approximated on a neighborhood of Γ' by the following linear approximation

$$\mathbf{P}'_{\text{smooth}}(\mathbf{x}) = \mathbf{P}'_{\text{smooth}}(\pi'_{\Gamma'}(\mathbf{x})) + \mathbf{P}'_{\text{smooth},\mathbf{x}}(\pi'_{\Gamma'}(\mathbf{x})) \cdot (\mathbf{x} - \pi'_{\Gamma'}(\mathbf{x})). \quad (3.33)$$

For purposes of simulation of the composite Poincaré map, γ , $\mathbf{P}'_{\text{smooth}}(\pi'_{\Gamma'}(\mathbf{x}))$, and $\mathbf{P}'_{\text{smooth},\mathbf{x}}(\pi'_{\Gamma'}(\mathbf{x}))$ are approximated by evaluating these at a finite subset of points on Γ' and subsequently using interpolation to extend these results to the entire curve Γ' .

We may again consider the reduction to a reduced composite Poincaré map as per the

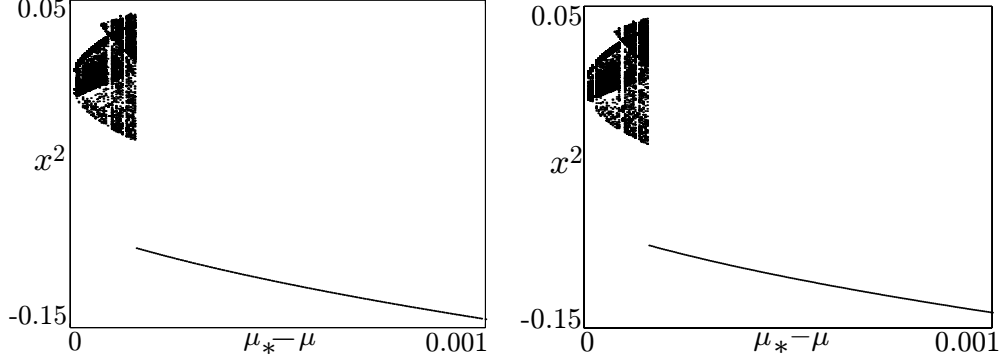


Figure 3.10: The figure shows the bifurcation diagram based on the \mathcal{P}' Poincaré section using numerical simulation of the original dynamical system (left panel) and the full composite map (2.81) (right panel). The map based on the \mathcal{P}' Poincaré section appears to reproduce the actual bifurcation scenario over a larger interval in $\mu_* - \mu$ than that based on \mathcal{P} .

expression

$$t \longmapsto \gamma^{-1} \circ \mathbf{P}'_{\text{smooth}} \circ \pi'_{\Gamma'} \circ \mathbf{g}_{\mathcal{P}'} \begin{pmatrix} \gamma^1(t) \\ \gamma^2(t) \\ x_*^3 \end{pmatrix} \quad (3.34)$$

since, to lowest-order in the deviation from \mathbf{x}_* , $\mathbf{g}_{\mathcal{P}'}(\mathbf{x}) - \mathbf{x}_*$ is tangential to Γ' . In particular, suppose that the parameterization is chosen such that $\gamma^2(t) = t$ near \mathbf{x}_* and let

$$\pi'_{\Gamma'}(\mathbf{x}) = \begin{pmatrix} \gamma^1(x^2) \\ x^2 \\ x_*^3 \end{pmatrix} \quad (3.35)$$

for $\mathbf{x} \approx \mathbf{x}_*$. Then, for t near 0, we have

$$\gamma(t) \approx \begin{pmatrix} x_*^1 + \frac{t^2}{2} \ddot{\gamma}^1(0) \\ t \end{pmatrix}, \quad (3.36)$$

since $\dot{\gamma}^1(0) = 0$ follows from the tangential contact of Γ' with \mathcal{D} and where $\ddot{\gamma}^1(0) < 0$. Moreover, for $\mu \lesssim \mu_*$, $h_{\mathcal{D}}(\mathbf{X}_0(\Gamma')) \approx \mu - x^1 - \frac{\alpha}{2}(x^2)^2 < 0$ where $0 < \alpha < -\ddot{\gamma}^1(0)$ (cf. the right panel of Fig. 3.11) for

$$-\sqrt{2 \frac{\mu_* - \mu}{|\ddot{\gamma}^1(0) + \alpha|}} \approx t_{\min} < t < t_{\max} \approx \sqrt{2 \frac{\mu_* - \mu}{|\ddot{\gamma}^1(0) + \alpha|}}. \quad (3.37)$$

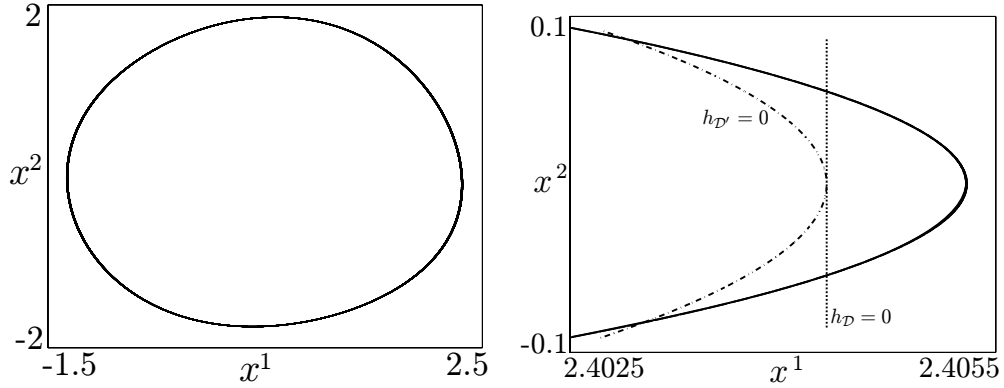


Figure 3.11: The intersection of the grazing quasiperiodic system attractor with the \mathcal{P}' section (left panel). Zero-level sets of $h_{\mathcal{D}}$ and $h_{\mathcal{D}'}$ for $\mu_* - \mu \approx 1 \times 10^{-3}$ (right panel).

Let

$$f(t) = \gamma^{-1} \circ \mathbf{P}'_{\text{smooth}} \begin{pmatrix} \gamma^1(t) \\ \gamma^2(t) \\ x_*^3 \end{pmatrix}. \quad (3.38)$$

Then, to lowest order the reduced map is given by

$$t \mapsto \begin{cases} f(t), & t \notin (t_{\min}, t_{\max}) \\ f\left(t - \rho_1 \sqrt{1 - \frac{t^2}{\rho_2^2}}\right), & t \in (t_{\min}, t_{\max}) \end{cases} \quad (3.39)$$

where

$$\rho_1 = 4.5089 \sqrt{(\mu_* - \mu)} \quad (3.40)$$

and

$$\rho_2 = \sqrt{\frac{2(\mu_* - \mu)}{|\gamma''(0) + \alpha|}}. \quad (3.41)$$

Again, in the first return map the correction takes the form of an ellipse with half-height $f'(0) \rho_1$ and half-width ρ_2 . Indeed, the analysis in Dankowicz *et al.* [9, 10] arrived at precisely these conclusions through a heuristic argument and without the *a priori* introduction of $\mathbf{g}_{\mathcal{P}'}$.

Fig. 3.12 shows a comparison between the graph of the third iterate of the reduced composite map (3.34) for two different values of μ and the projection onto the third component of the third iterate of the full composite Poincaré map (2.81) evaluated for points

on the corresponding system attractor. Similar conclusions as those discussed in the case of the reduced composite map (3.22) can again be drawn. Indeed, as shown in the lower right panel of Fig. 3.6, the reduced composite map appears to capture the projected dynamics with high accuracy even though it apparently fails to predict the extra branch that appears for $\mu_* - \mu = 15 \times 10^{-5}$ (cf. right panel of Fig. 3.12).

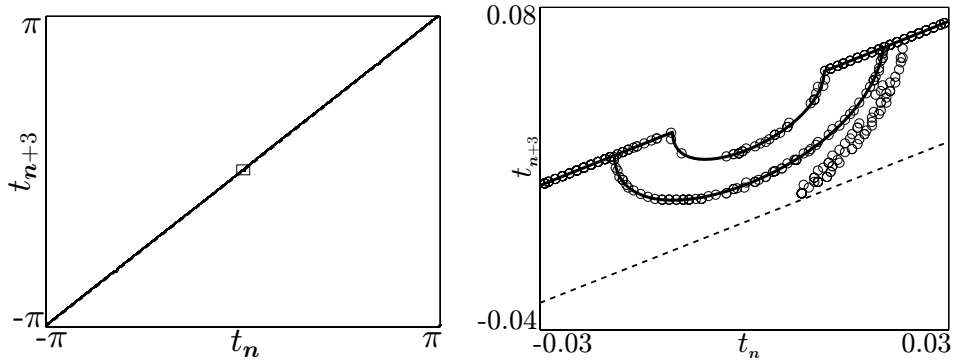


Figure 3.12: A comparison between the graph of the third iterate of the reduced map (solid) for $\mu_* - \mu = 5 * 10^{-5}$ and $\mu_* - \mu = 15 * 10^{-5}$ and the projection onto the third component of the third iterate of the full composite Poincaré map (2.81) (circles) evaluated for points on the corresponding system attractor using arc-length parameterization (left panel). Blow-up (right panel) of the boxed part in the left panel.

For small values of $\mu_* - \mu$, the impacting attractor is weakly chaotic in the sense described by Dankowicz *et al.* [9], i.e, the impacting motion is largely torus-covering and the largest Lyapunov exponent is positive, but small (~ 0.02). The analysis presented in Dankowicz *et al.* [9] using a heuristic reduced composite map also predicts the presence of strong chaos (localized attractor with largest Lyapunov exponent distinctly positive) for $\mu_* - \mu \approx 0.025$. Fig. 3.13 shows the intersection of the system attractor obtained using direct numerical simulation of the original differential equations, iteration of the full composite Poincaré map (2.81), and iteration of the reduced composite map (3.34). It is clear that, although the reduced map is able to capture the coarse structure of the attractor, it predicts an infinitely thin attractor. In contrast, the full composite map is able to resolve the attractor into several distinct branches as shown in the magnified insets.

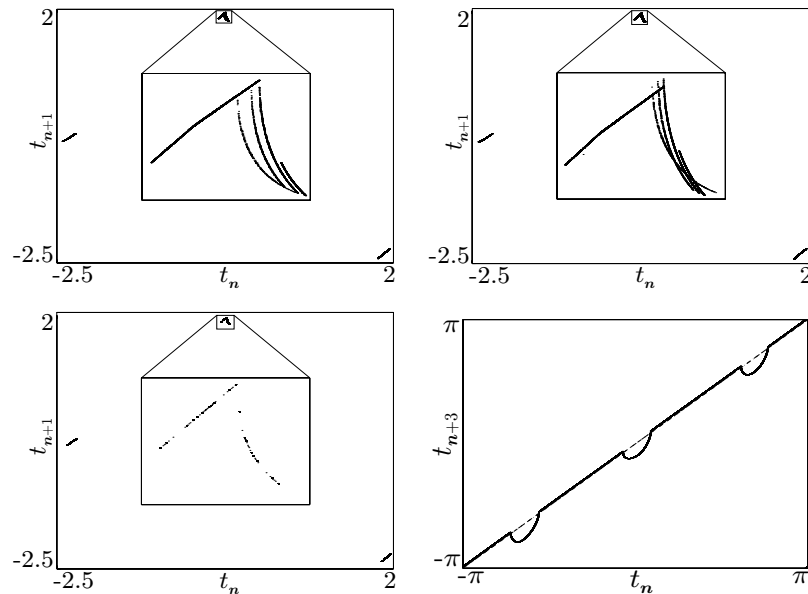


Figure 3.13: A comparison between the graph of the third iterate using direct numerical simulation (upper-left panel), full composite mapping (upper-right panel) and the reduced map (lower-left panel) for $\mu_* - \mu = 0.025$ and evaluated for points on the corresponding impacting chaotic system attractor. The corresponding third iterate of the full composite map (lower-right panel) shows the intersection with the identity line (dashed).

In the case of a quasiperiodic motion on a co-dimension-one invariant torus, the stretching caused by the square-root term remains, to lowest order, tangential to the torus for all forward iterates of the Poincaré map. Moreover, the number of iterates required to return to a small neighborhood of the grazing point goes to infinity as the size of the neighborhood shrinks. Thus, assuming that the invariant torus is normally attracting in the absence of impacts, the destabilizing effects of impacts are expected to be dominated by the stabilizing effects of the linearized dynamics in the transverse directions to the torus. This argues for the persistence of a near-grazing attractor that limits on the grazing quasiperiodic trajectory as the system parameters approach their values at grazing.

As will be seen in the next chapter, in the case of co-dimension-two (or higher) quasiperiodic attractors, the square-root term is typically no longer tangential to the invariant

torus. Even in this case, however, the stabilizing effects of the linear dynamics away from the torus are expected to result in the persistence of a local attractor, at least for some nonzero deviation from the grazing bifurcation point.

3.4 Summary

This chapter illustrated grazing bifurcation scenarios in the case of co-dimension-one invariant tori. In particular, grazing bifurcations of a periodic trajectory in a two-dimensional state space and a quasiperiodic trajectory in a three-dimensional state space were studied. Moreover, the effects of the square-root term originating in the local description of the impacting dynamics on such bifurcations was discussed. A rigorous application of the full discontinuity-mapping approach to an originally quasiperiodic attractor has been achieved. The illustrations presented in this chapter also manifest a general phenomenon in the study of impacting dynamics of co-dimension-one invariant tori.

The local description of impacting dynamics in the case of a periodic trajectory in a two-dimensional state space is to lowest order linear in the deviation from the grazing trajectory. This implies that the instabilities caused by the singular nature of the square-root term are absent possibly leading to a *continuous grazing bifurcation*. In the example discussed, the approximate expressions for the fixed points corresponding to the nonimpacting and impacting periodic trajectories form the basis for a criterion that dictates whether the grazing bifurcation is continuous or discontinuous. Using the discontinuity-mapping approach, eigenvalues corresponding to the impacting periodic trajectory are also computed that are in good agreement with the ones obtained from the numerical simulation of the original dynamical system. The presence of an order $\frac{3}{2}$ term in the local description of the impacting dynamics induces a square-root type behavior in the eigenvalues for positive deviations away from the grazing incidence. Even though the transition from nonimpacting to impacting motion with a change of parameter is, in the sense mentioned earlier, continuous in nature, the

eigenvalues experience a discrete jump during the transition via a grazing contact. However, the absolute values of the eigenvalues immediately before and after the jump are bounded above unlike more drastic cases that will be discussed in the next chapter.

The impacting dynamics of an originally co-dimension-one quasiperiodic attractor following a grazing incidence are more complicated than its periodic counterpart because of the presence of a square-root term in the composite Poincaré map. However, its presence in the dynamics only in the tangential direction to the torus facilitates an unrestricted local bifurcation analysis of the post-grazing dynamics in the vicinity of the grazing contact. Here, under the assumption that the grazing quasiperiodic trajectory is stable, it can be concluded that the smooth dynamics stabilize the trajectory for sufficiently small perturbations away from the grazing point.

Bifurcation diagrams obtained using various levels of approximations of the composite Poincaré map suggest a continuous transition from nonimpacting to impacting motion marking the grazing bifurcation continuous for the given system parameters. Windows of weakly chaotic and periodic motion are present for small, positive deviations from the parameter corresponding to the grazing contact followed by periodic motion for larger deviations. This behavior is supported with the computation of the nontrivial Lyapunov exponent for each case. It is also shown that the correction to the return map describing the smooth dynamics, due to the presence of discontinuities takes the form of a semi-ellipse whose semi-major and semi-minor axes can be accurately computed from conditions at the grazing contact.

Chapter 4

Grazing Bifurcations of Co-dimension-two Invariant Tori

Note: Parts of this chapter are reprinted from P. Thota, H. Dankowicz, “Analysis of grazing bifurcations of quasiperiodic system attractors ”, *Physica D*, 220(2), pp. 163 – 174 Copyright (2006), with permission from Elsevier.

4.1 Introduction

The purpose of this chapter is to formulate and closely examine the conditions under which a local attractor persists near (not necessarily periodic) grazing trajectories corresponding to co-dimension-two invariant tori. Two example piecewise smooth dynamical systems, a periodic trajectory in a three-dimensional state space and a two-frequency quasiperiodic trajectory in a four-dimensional state space, are employed in an effort to formulate such conditions. In both cases, as was done in the previous chapter, a local analysis based on the discontinuity-mapping approach is employed to derive a normal-form description of the dynamics near a grazing trajectory. Also, the results obtained from applying the

discontinuity-mapping approach to the two examples are compared with those from direct numerical simulation of the original dynamical system.

This chapter presents the application of the discontinuity-mapping approach to the study of near-grazing bifurcations of originally quasiperiodic, co-dimension-two system attractors. It also establishes an exact formulation for the discontinuity-mapping methodology under the assumption that a Poincaré section can be found that is everywhere transversal to the grazing attractor. Even though the implementation of the Poincaré section \mathcal{P}' was an alternative approach (at least in the example studied) in the analysis of grazing bifurcations of co-dimension-one quasiperiodic system attractors, it becomes mandatory in certain cases of co-dimension-two quasiperiodic attractors. Similar to the co-dimension-one quasiperiodic case, the accuracy of the reduced maps corresponding to the application of projection methods to the composite Poincaré map is studied.

Once again, the qualitative changes in the system dynamics that occur due to the onset of an impacting motion from a nonimpacting one are studied from the perspective of *the loss of a local attractor*. Such dramatic changes whose origin lies in the presence and orientation of a square-root term in the normal-form for the impacting motion near a grazing contact are emphasized in the analysis presented here. Particularly, the direction of application of such instabilities becomes more prominent and influential in co-dimension-two or higher system attractors. The results obtained are extrapolated to understand grazing bifurcations of a general class of co-dimension-two system attractors.

4.2 Grazing Bifurcations of a Co-dimension-two Periodic Attractor

Consider the dynamical system governed by the vector field ([38] and [31])

$$\mathbf{f}(\mathbf{x}) = \begin{pmatrix} mx^1 - x^2 - x^1x^3 \\ mx^2 + x^1 \\ -x^3 + (x^2)^2 + (x^1)^2x^3 \end{pmatrix}, \quad (4.1)$$

event function $h_{\mathcal{D}}(\mathbf{x}) = x^1 - \mu$ (and, consequently, $h_{\mathcal{P}}(\mathbf{x}) = mx^1 - x^2 - x^1x^3$) and state jump function

$$\mathbf{g}_{\mathcal{D}}(\mathbf{x}) = \begin{pmatrix} x^1 \\ (m - x^3)x^1 - r(x^2 - x^1(m - x^3)) \\ x^3 \end{pmatrix}, \quad (4.2)$$

where $m, r > 0$ and μ are system parameters. In particular, for $r = 0.8$, $m = 0.28$, and $\mu = \mu_* = -0.7981 \dots$, numerical integration shows the existence of a point

$$\mathbf{x}_* = \begin{pmatrix} -0.7981 \dots & 0.2747 \dots & 0.6242 \dots \end{pmatrix}^T \quad (4.3)$$

corresponding to the intersection of a periodic trajectory (Refer to Fig. 4.1-left panel) with \mathcal{D}^0 , such that $a_* > 0$. Similarly, for $r = 0.8$, $m = 0.39$, and $\mu = \mu_* = -0.8271 \dots$, numerical integration shows the existence of a point

$$\mathbf{x}_* = \begin{pmatrix} -0.8271 \dots & -0.0722 \dots & 0.3026 \dots \end{pmatrix}^T \quad (4.4)$$

corresponding to the intersection of a periodic trajectory (Refer to Fig. 4.1-right panel) with \mathcal{D}^0 .

Using the discontinuity-mapping methodology discussed in Chapter 2, to lowest order, the discontinuity mapping takes the form

$$\mathbf{D}(\mathbf{x}) = \mathbf{x}_* + \begin{cases} \begin{pmatrix} \mathbf{x} - \mathbf{x}_* \\ 0 \end{pmatrix} & x^1 - \mu \geq 0 \\ \begin{pmatrix} 0.3961\sqrt{\mu - x^1} \\ 0.4962\sqrt{\mu - x^1} \end{pmatrix} & x^1 - \mu < 0 \end{cases} \quad (4.5)$$

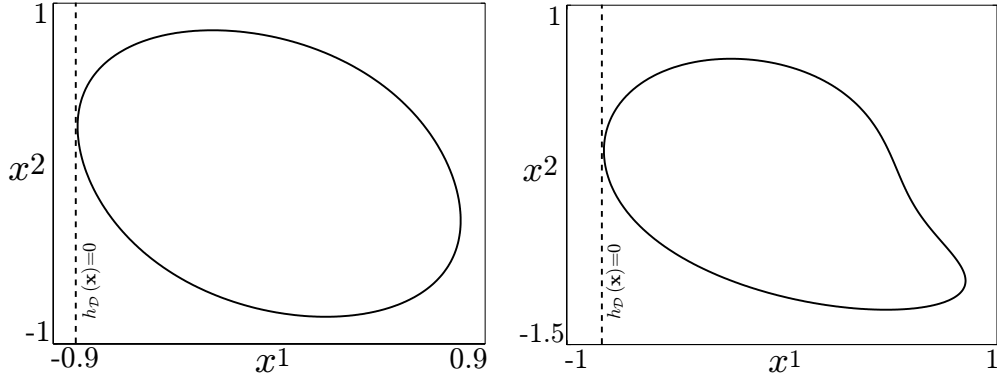


Figure 4.1: Grazing periodic orbits projected on to the $x^1 - x^2$ plane for $m = 0.28$ (left panel) and $m = 0.39$ (right panel) corresponding to the vector field given in Eq. (4.1). In both cases, a projection of the discontinuity surface $h_{\mathcal{D}} = 0$ is also shown in the figure

when $r = 0.8$ and $m = 0.28$ and

$$\mathbf{D}(\mathbf{x}) = \mathbf{x}_* + \begin{cases} \begin{pmatrix} \mathbf{x} - \mathbf{x}_* \\ 0 \\ 0.2153\sqrt{\mu - x^1} \\ 0.2603\sqrt{\mu - x^1} \end{pmatrix} & x^1 - \mu \geq 0 \\ \begin{pmatrix} \mathbf{x} - \mathbf{x}_* \\ 0 \\ 0.2153\sqrt{\mu - x^1} \\ 0.2603\sqrt{\mu - x^1} \end{pmatrix} & x^1 - \mu < 0 \end{cases} \quad (4.6)$$

when $r = 0.8$ and $m = 0.39$.

As shown in the left panel of Fig. 4.2, for $m = 0.28$ direct numerical integration shows the existence of a unique locally attracting periodic trajectory emanating from and in the immediate vicinity of the grazing periodic trajectory with negative penetration for $\mu < \mu_*$. Indeed, as seen in the right panel, for small deviations this behavior is captured by the composite Poincaré map. However, for $\mu > \mu_*$, there does not exist a periodic trajectory emanating from and in the immediate vicinity of the grazing trajectory. Instead, the system dynamics experience a distinct jump to an impacting periodic trajectory with a penetration that remains distinct from zero as $\mu \rightarrow \mu_*$. Indeed, the periodic impacting trajectory that appears for $\mu \gtrsim \mu_*$ also persists for $\mu \lesssim \mu_*$, such that an impacting and a nonimpacting periodic attractor coexist for some interval prior to the initial grazing contact of the nonimpacting trajectory. The figure also shows that the impacting periodic attractor

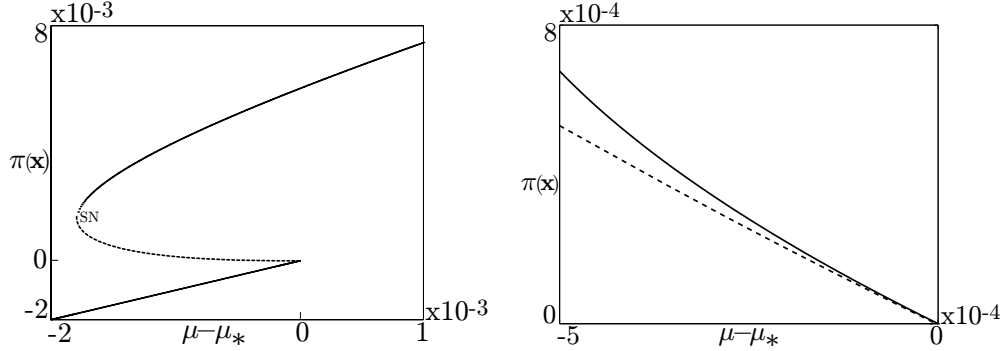


Figure 4.2: Bifurcation diagrams showing the penetration $\pi(\mathbf{x})$ as a function of $\mu - \mu_*$ for nonimpacting and impacting motions when $m = 0.28$ obtained using numerical simulations of the original dynamical system (left panel). Right panel compares the unstable impacting orbit obtained using numerical simulation of the original dynamical system (dotted) and the composite Poincaré map (solid). It is evident that the accuracy of the prediction obtained using the composite Poincaré map deteriorates for as $(\mu - \mu_*)$ increases from 0. Here, SN in the left panel denotes a saddle-node bifurcation.

that exists for $\mu \lesssim \mu_*$ disappears in a saddle node bifurcation. Since, in this case, there does not exist a one-parameter family of system attractors emanating from the grazing trajectory, we refer to this transition from nonimpacting to impacting motions as a *discontinuous grazing bifurcation*.

In contrast, a *continuous grazing bifurcation* occurs for $m = 0.39$, $\mu_* = -0.8271 \dots$ and $r = 0.8$ as shown in Figs. 4.3 and 4.4. In this case, for $\mu > \mu_*$, there exists an impacting trajectory emanating from and in the immediate vicinity of the grazing trajectory making the bifurcation continuous. Also, a reverse period-adding scenario, one of the signatures of grazing bifurcations, is seen in the figures. Here, as one approaches the parameter corresponding to the grazing contact from the impacting side, the periodicity of the impacting motion increases monotonically leading to an infinite period orbit at grazing. Figs. 4.3 and 4.4 also show bifurcation diagrams obtained for $m = 0.39$ using an approximation of the composite Poincaré map that agrees both qualitatively and quantitatively with that obtained through

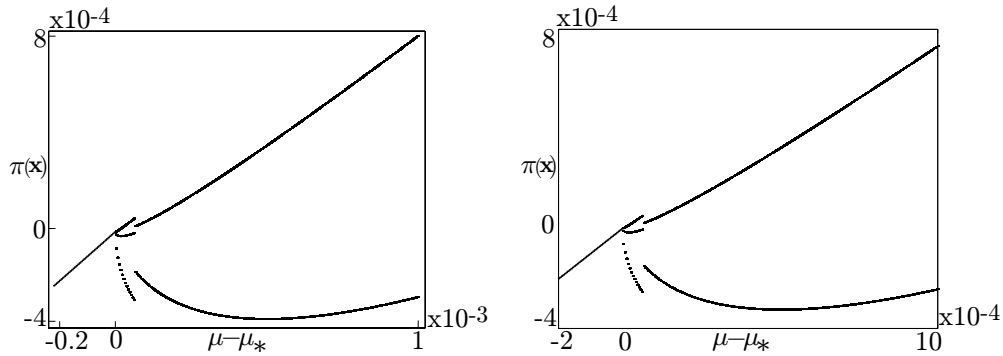


Figure 4.3: Bifurcation diagrams showing the penetration $\pi(\mathbf{x})$ as a function of $\mu - \mu_*$ for nonimpacting and impacting motions when $m = 0.39$ obtained using numerical simulation of the original dynamical system (left panel) and composite Poincaré map (right panel).

direct numerical integration.

Using definition (2.7), it is observed that $\xi_1 = -0.02306\dots < 0$ for $m = 0.28$ resulting in a discontinuous bifurcation. In contrast, when $m = 0.39$, ξ_n is positive for $n < 100$ suggesting a continuous grazing bifurcation. These observations are confirmed by the bifurcation diagrams shown in Figs. 4.2 and 4.3. These qualitatively different grazing bifurcations are related by a *co-dimension-two grazing bifurcation point* for which $\xi_1 = 0$. A comprehensive study of co-dimension-two grazing bifurcation points in single-degree-of-freedom, linear and nonlinear, impact oscillators have been documented by Thota *et al.* [45], and Dankowicz & Zhao [7].

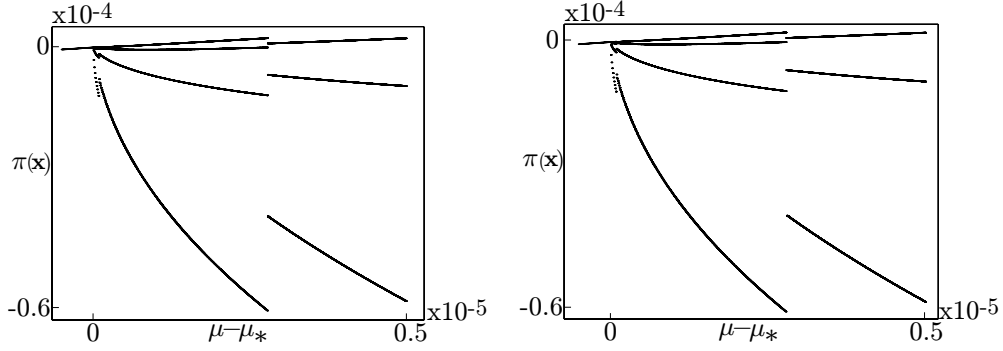


Figure 4.4: Bifurcation diagrams showing the penetration $\pi(\mathbf{x})$ as a function of $\mu - \mu_*$ for nonimpacting and impacting motions when $m = 0.39$ obtained using numerical simulation of the original dynamical system (left panel) and composite Poincaré map (right panel) for smaller deviations than shown in Fig. 4.3. Here, higher periodic orbits with one impact per period are observed that are not present for larger deviations. Indeed, for much smaller deviations than those presented in this figure, periodic orbits with periodicity > 5 can be obtained.

4.3 Grazing Bifurcations of a Co-dimension-two Torus Attractor

As a second example, consider the dynamical system corresponding to the vector field (a forced version of the vector field studied in the previous section)

$$\mathbf{f}(\mathbf{x}) = \begin{pmatrix} mx^1 - x^2 - x^1 x^3 \\ mx^2 + x^1 + A \cos x^4 \\ -x^3 + (x^2)^2 + (x^1)^2 x^3 \\ \omega \end{pmatrix} \quad (4.7)$$

in terms of the state vector

$$\mathbf{x} = \begin{pmatrix} x^1 & x^2 & x^3 & x^4 \end{pmatrix}^T \in \mathbb{R}^3 \times \mathbb{S}^1, \quad (4.8)$$

the event function $h_{\mathcal{D}}(\mathbf{x}) = x^1 - \mu$ (and, consequently, $h_{\mathcal{P}}(\mathbf{x}) = mx^1 - x^2 - x^1x^3$), and associated event map

$$\mathbf{g}_{\mathcal{D}}(\mathbf{x}) = \begin{pmatrix} x^1 \\ (m - x^3)x^1 - r(x^2 - x^1(m - x^3)) \\ x^3 \\ x^4 \end{pmatrix}, \quad (4.9)$$

where $r, m, A, \omega > 0$ and μ are system parameters. When ignoring the effects of the event map $\mathbf{g}_{\mathcal{D}}$, the asymptotic response of this dynamical system exhibits periodic, quasiperiodic, and chaotic motions for different values of A . As an example, Fig. 4.5 (left panel) shows the largest Lyapunov exponent of the system under variations in the value of A for $r = 0.8$, $m = 0.28$, $\omega = 1.9$. In particular, for $A \in (1, 1.252)$, the dynamical system exhibits quasiperiodic motion with two incommensurate frequencies and for values of A greater than 1.252, the system dynamics change to a periodic motion with period-1.

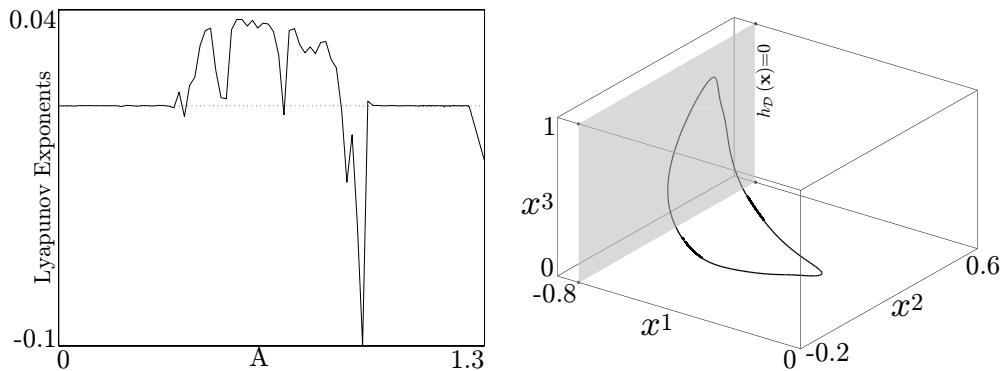


Figure 4.5: Left panel - The largest Lyapunov exponent as a function of A . Right panel - Projection of the invariant curve (intersection of the quasiperiodic trajectory with the Poincaré section $h_{\mathcal{P}} = 0$) and the discontinuity surface on to a lower dimensional space. Here, $A = 1.1$ and $\omega = 1.9$.

In particular, for $r = 0.8$, $m = 0.28$, $A = 1.1$, $\omega = 1.9$, and $\mu = \mu_* = -0.7297\dots$, numerical integration shows the existence of a grazing event at

$$\mathbf{x}_* = \left(-0.7297 \dots \quad 0.3633 \dots \quad 0.7779 \dots \quad 3.0088 \dots \right)^T \quad (4.10)$$

corresponding to the tangential intersection of a quasiperiodic trajectory with \mathcal{D}^0 , such that $a_* > 0$. To lowest order and with four significant digits, the discontinuity mapping corresponding to \mathcal{P} takes the form

$$\mathbf{g}_{\mathcal{P}}(\mathbf{x}) = \mathbf{x}_* + \begin{cases} \mathbf{x} - \mathbf{x}_*, & x^1 - \mu \geq 0 \\ \begin{pmatrix} 0 \\ 0.3457 \sqrt{\mu - x^1} \\ 0.4738 \sqrt{\mu - x^1} \\ -3.8858 \sqrt{\mu - x^1} \end{pmatrix}, & x^1 - \mu < 0 \end{cases}, \quad (4.11)$$

As shown in Fig. 4.5(right panel), the intersection of the quasiperiodic trajectory with \mathcal{P} is an invariant curve Γ given by $(x^1, x^2, x^3)^T = \gamma(x^4)$ for $x^4 \in \mathbb{S}^1$. For every point $\mathbf{x} \in \mathcal{P}$ in the vicinity of this curve, we again define the projection

$$\pi_{\Gamma}(\mathbf{x}) = \begin{pmatrix} \gamma(x^4) \\ x^4 \end{pmatrix} \quad (4.12)$$

and approximate the smooth Poincaré map $\mathbf{P}_{\text{smooth}}$ on a neighborhood of Γ by the linear approximation

$$\mathbf{P}_{\text{smooth}}(\mathbf{x}) = \mathbf{P}_{\text{smooth}}(\pi_{\Gamma}(\mathbf{x})) + \mathbf{P}_{\text{smooth},\mathbf{x}}(\pi_{\Gamma}(\mathbf{x}))(\mathbf{x} - \pi_{\Gamma}(\mathbf{x})). \quad (4.13)$$

The expressions for $\mathbf{g}_{\mathcal{P}}(\mathbf{x})$ and $\mathbf{P}_{\text{smooth}}(\mathbf{x})$ are combined to obtain a composite Poincaré map. Again, the Poincaré map $\mathbf{P}_{\text{smooth}}(\mathbf{x})$ is evaluated at finite number of points on the invariant curve Γ and then interpolated to the entire curve.

Fig. 4.6 shows the bifurcation behavior under variations in $\mu - \mu_*$ obtained using direct numerical simulation (left panel) and iterations of the full composite map (2.80) (right panel). It is evident that the discontinuity-mapping approach captures both the qualitative and quantitative features of the impacting dynamics accurately even for larger deviations. Also,

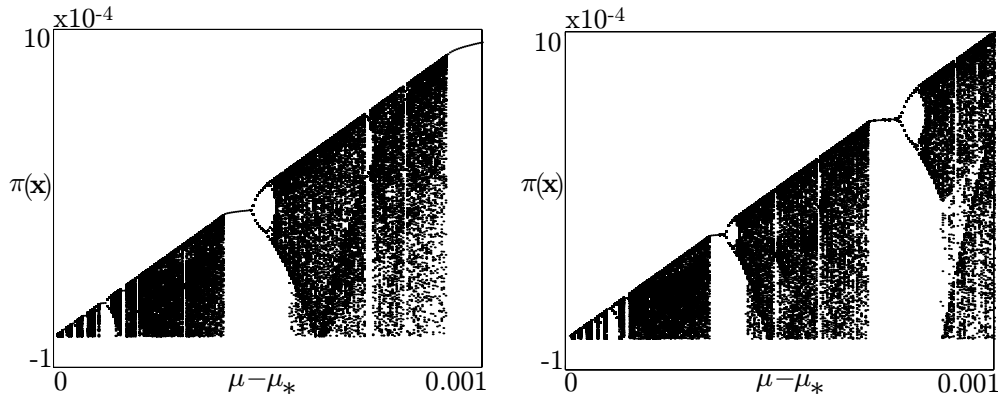


Figure 4.6: Bifurcation diagram generated using direct numerical integration of the vector field for $A = 1.1$ (left panel) [46] and iterations of composite map obtained using the discontinuity-mapping approach (right panel).

Fig. 4.7 shows the nontrivial Lyapunov exponent corresponding to the bifurcation diagrams discussed in Fig. 4.6.

Following the methodology in the previous chapter, it is again possible to derive a reduced composite map that attempts to capture the tangential dynamics along the attractor, provided that the attractor is closely approximated by the original invariant curve. Fig. 4.8 shows a comparison between the graph of the first return map for the impacting quasiperiodic system using direct numerical simulation and the corresponding reduced composite map. It is evident that the reduced map fails to predict the qualitative behavior of the impacting system even for smaller penetrations. The reason for the failure can be explained using the geometry of the original system attractor and the form of the discontinuity mapping $\mathbf{g}_{\mathcal{P}}$. In contrast to the case of the forced van-der-Pol oscillator studied in the previous chapter, the higher co-dimension of the grazing attractor and the presence of square-root terms in $\mathbf{g}_{\mathcal{P}}$ that is transversal to Γ implies that the tangential dynamics no longer dominate the normal dynamics and the latter cannot be neglected.

Whereas the bifurcation behavior observed in the above case is continuous in the sense that a local attractor persists near Γ for relatively large deviations of μ from μ_* , this is no

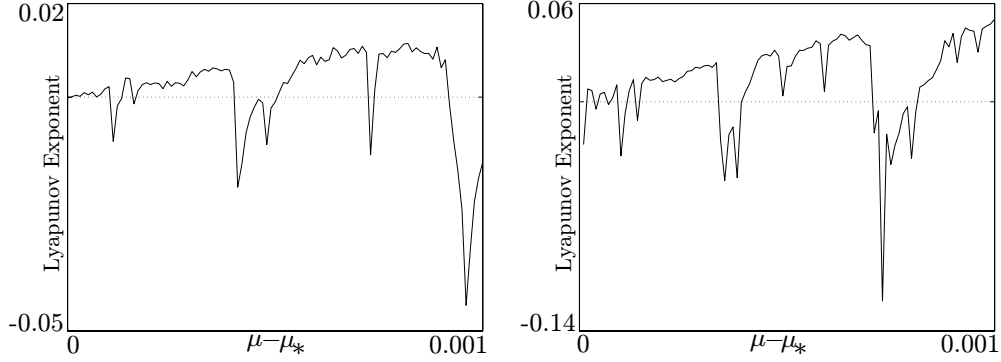


Figure 4.7: Nontrivial Lyapunov exponent corresponding to the impacting motion for $A = 1.1$ obtained using direct numerical integration of the original dynamical system (left panel) and composite Poincaré map (right panel). These graphs are in good agreement with the bifurcation diagrams shown in Fig. 4.6 i.e., the nontrivial Lyapunov exponent oscillates between positive and negative values corresponding to the periodic and chaotic windows. Note that the positive value obtained by the nontrivial Lyapunov exponent is $\ll 1$ indicating a weakly chaotic behavior.

longer the case for $A = 1.25$ and $\mu_* = -0.4940\dots$, for which a grazing event occurs at

$$\mathbf{x}_* = \left(-0.4940\dots \quad 0.0946\dots \quad 0.4716\dots \quad 3.2188\dots \right)^T \quad (4.14)$$

corresponding to the tangential intersection of a two-frequency quasiperiodic trajectory with \mathcal{D}^0 . To lowest order and with four significant digits, the discontinuity-mapping corresponding to \mathcal{P} takes the form

$$\mathbf{g}_{\mathcal{P}}(\mathbf{x}) = \mathbf{x}_* + \begin{cases} \mathbf{x} - \mathbf{x}_*, & x^1 - \mu \geq 0 \\ \begin{pmatrix} 0 \\ 0.3519\sqrt{\mu - x^1} \\ 0.7123\sqrt{\mu - x^1} \\ -3.8947\sqrt{\mu - x^1} \end{pmatrix}, & x^1 - \mu < 0 \end{cases}, \quad (4.15)$$

In this case a jump occurs from a local chaotic attractor to a distant periodic orbit for $\mu - \mu_* \approx 3.7 \times 10^{-5}$, as shown in Fig. 4.9 (left panel) (cf. Fig. 4.10). Although the

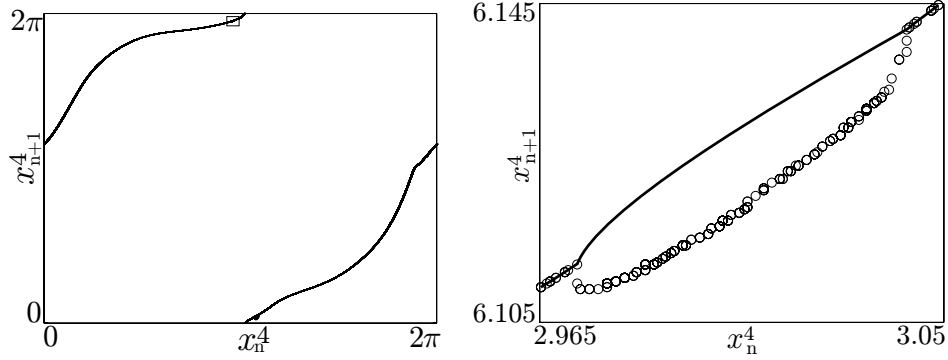


Figure 4.8: A comparison between the graph of the first iterate of the reduced map (solid) for $\mu - \mu_* = 15 * 10^{-5}$ and the projection onto the fourth component of the full composite Poincaré map (2.80) (circles) evaluated for points on the corresponding system attractor (left panel). Blow-up (right panel) of the boxed part in the left panel.

composite Poincaré map is able to predict this loss of a local attractor, it is unable to capture the resultant periodic motion as this occurs far away from the grazing event. This effectively discontinuous bifurcation scenario resembles the grazing bifurcation scenario obtained for the periodic orbit found for $A = 1.253$ and possibly originates in the closeness of the quasiperiodic attractor to this periodic orbit (the quasiperiodic attractor is born in a Hopf bifurcation near $A \approx 1.252$). Moreover, the expressions for the discontinuity mappings given by Eq. (4.15) and Eq. (4.11) for $A = 1.25$ and $A = 1.1$ are similar to each other in terms of their numerical and stretching characteristics eliminating the possibility of the orientation of the square-root term as a cause for the qualitatively different impacting motion in the two cases ($A = 1.1$ and $A = 1.25$).

Fig. 4.11 shows the fractal nature of the attractor obtained using the full composite Poincaré map for $A = 1.25$ and $\mu - \mu_* = 2 \times 10^{-5}$. The correlation dimension [41] for this chaotic attractor has also been calculated as ≈ 1.2 using 12500 points. This attractor is weakly chaotic in the sense described by Dankowicz *et al.* [9] i.e, torus-covering with largest Lyapunov exponent positive but very small ($\ll 1$).

Now consider the case when $r = 0.8$, $m = 0.28$, $A = 1.5$, $\omega = 4$, and $\mu = \mu_* =$

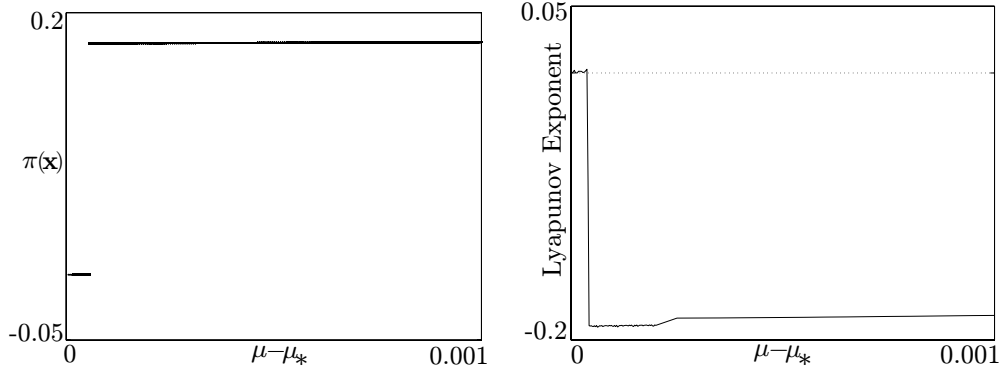


Figure 4.9: Bifurcation diagram obtained under variations in $\mu - \mu_*$ using direct numerical simulation (left panel) for $A = 1.25$. The right panel shows the nontrivial Lyapunov exponent corresponding to the bifurcation behavior in the left panel.

$-0.8548\dots$, for which numerical integration shows the existence of a grazing event at

$$\mathbf{x}_* = \left(-0.8548\dots \quad 0.2897\dots \quad 0.6189\dots \quad 2.9317\dots \right)^T \quad (4.16)$$

corresponding to the tangential intersection of a quasiperiodic trajectory with \mathcal{D}^0 . As shown in the left panel of Fig. 4.12, the intersection of the system attractor with \mathcal{P} is a discontinuous curve with terminal points corresponding to non-transversal intersections with \mathcal{P} . In contrast, the right panel of Fig. 4.12 shows a closed invariant curve Γ' corresponding to the intersection of the system attractor with $\mathcal{P}' = \{\mathbf{x} \mid x^4 = x_*^4\}$.

To lowest order and with four significant digits, the discontinuity mapping corresponding to \mathcal{P}' takes the form

$$\mathbf{g}_{\mathcal{P}'}(\mathbf{x}) = \mathbf{x}_* + \begin{cases} \begin{pmatrix} \mathbf{x} - \mathbf{x}_* \\ 0 \\ -3.7499 \sqrt{\mu - x^1} \\ 0 \\ 0 \end{pmatrix} & h_{\mathcal{D}}(\mathbf{X}_0(\mathbf{x})) \geq 0 \\ \begin{pmatrix} \mathbf{x} - \mathbf{x}_* \\ 0 \\ -3.7499 \sqrt{\mu - x^1} \\ 0 \\ 0 \end{pmatrix} & h_{\mathcal{D}}(\mathbf{X}_0(\mathbf{x})) < 0 \end{cases} \quad (4.17)$$

Fig. 4.13 shows the bifurcation behavior under variations in $\mu - \mu_*$ obtained using direct numerical simulation (left panel) and iterations of the composite map (2.81) (right panel).

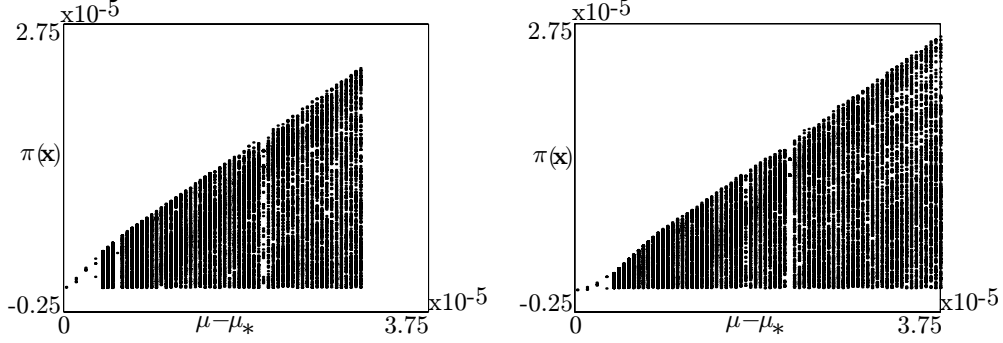


Figure 4.10: Comparison of the bifurcation behavior obtained under variations in $\mu - \mu_*$ using direct numerical simulation (left panel) and iteration of the full composite map (right panel) for $A = 1.25$. Note that the composite map predicts a diverging response for $\mu - \mu_*$ beyond the right edge of the diagram in qualitative agreement with the disappearance of a local attractor shown in the left panel.

An interesting feature of the discontinuity mapping given by Eq. (4.17), corresponding to the Poincaré section \mathcal{P}' , is that the stretching resulting from the square-root term is present only along the x^2 component of the state vector making the dynamics seemingly simple and yet, retaining the complexity of the impacting motion in all its characteristics.

4.4 On Square-root Instability

The lowest nontrivial term in the expansion of $\mathbf{g}_{\mathcal{P}}$ in the deviation of \mathbf{x} from \mathbf{x}_* is of the form

$$\beta \sqrt{-h_{\mathcal{D},\mathbf{x}}(\mathbf{x}_*) \bullet (\mathbf{x} - \mathbf{x}_*)}, \quad (4.18)$$

where β is given by the Eq. (2.112). Since

$$h_{\mathcal{P},\mathbf{x}}(\mathbf{x}_*) \bullet \mathbf{f}(\mathbf{x}_*) = a_*, \quad h_{\mathcal{D},\mathbf{x}}(\mathbf{x}_*) \bullet \mathbf{f}(\mathbf{x}_*) = 0, \quad (4.19)$$

and since $\mathbf{g}_{\mathcal{D},\mathbf{x}}(\mathbf{x}_*)$ maps vectors tangential to \mathcal{D} to vectors tangential to \mathcal{D} , it follows that

$$h_{\mathcal{P},\mathbf{x}}(\mathbf{x}_*) \bullet \beta = 0, \quad (4.20)$$

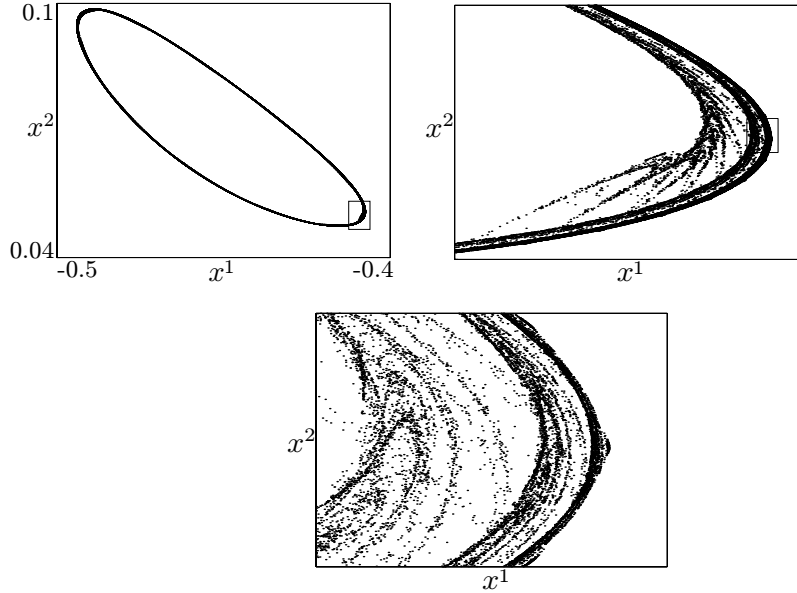


Figure 4.11: The intersection of the system attractor with \mathcal{P} obtained using the full composite Poincaré map for $A = 1.25$ and $\mu - \mu_* = 2 \times 10^{-5}$. The fractal nature of the chaotic attractor is evident in this figure.

and

$$h_{\mathcal{D}, \mathbf{x}}(\mathbf{x}_*) \bullet \beta = 0, \quad (4.21)$$

i.e., β is tangential to $\mathcal{P} \cap \mathcal{D} = \mathcal{D}^0$. In particular, in a two-dimensional state space, it follows that $\beta = \mathbf{0}$. Similarly, in the case of grazing contact of a co-dimension-one invariant quasiperiodic torus with a discontinuity surface, it follows that β is tangential to the torus at the point of grazing contact, whereas this need not be the case for co-dimension-two or higher tori.

The presence of the square-root term results in a significant stretching $\mathbf{P}(\mathbf{x}) - \mathbf{P}(\mathbf{x}_*)$ of a small initial deviation $\mathbf{x} - \mathbf{x}_*$. This stretching occurs in the direction given by the image of the vector β under the Jacobian $\mathbf{P}_{\text{smooth}, \mathbf{x}}(\mathbf{x}_*)$ of the smooth Poincaré map. The accumulated effect of such stretching over subsequent iterations is likely to result in the disappearance of a local attractor in the immediate vicinity of the grazing attractor for $\mu > \mu_*$.

For a periodic grazing trajectory, such that $\mathbf{P}(\mathbf{x}_*) = \mathbf{x}_*$, a necessary condition for a

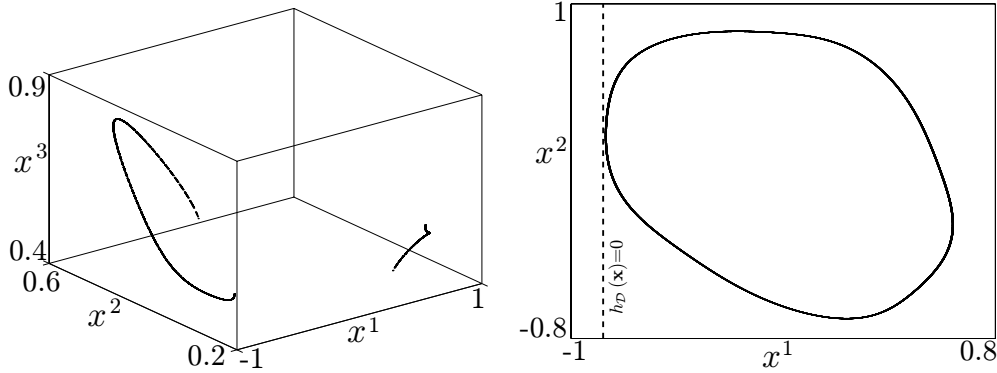


Figure 4.12: Intersection of the grazing quasiperiodic attractor with \mathcal{P} (left panel) and \mathcal{P}' (right panel) for $A = 1.5$ and $\omega = 4$.

continuous grazing bifurcation as long as $\beta \neq \mathbf{0}$ have been formulated by Fredriksson & Nordmark [20]. In particular, they argue that a family of local attractors emanating from and in the immediate vicinity of the grazing trajectory and parameterized by μ exists if and only if there is no upper bound on the number of iterates between impacts on any neighborhood of the grazing trajectory as $\mu \rightarrow \mu_*$ and the map $\mathbf{P}(\mathbf{x})$ is smooth about the point \mathbf{x}_* . In particular, for a periodic trajectory, the number of iterates between impacts when $\mu = \mu_*$ is given by the smallest integer n for which

$$\xi_n \stackrel{\text{def}}{=} h_{\mathcal{D},\mathbf{x}}(\mathbf{x}_*) \bullet \underbrace{\mathbf{P}_{\text{smooth},\mathbf{x}}(\mathbf{x}_*) \bullet \cdots \bullet \mathbf{P}_{\text{smooth},\mathbf{x}}(\mathbf{x}_*)}_{n \text{ times}} \bullet \beta < 0. \quad (4.22)$$

If, instead, $\beta = \mathbf{0}$, e.g., in the case of a grazing periodic trajectory in a two-dimensional state space, then the lowest-order term in the expansion of \mathbf{P} for $\mathbf{x} \approx \mathbf{x}_*$ is linear in $\mathbf{x} - \mathbf{x}_*$. The persistence of a local attractor can then be deduced from a study of a piecewise linear map and the bifurcations associated with such a grazing trajectory fall into the class of border-collision bifurcations [23, 36, 50].

For a grazing quasiperiodic orbit on a co-dimension-one invariant torus, the invariance of the torus under $\mathbf{P}_{\text{smooth}}$ implies that all forward images of β under the Jacobian of $\mathbf{P}_{\text{smooth}}$ will remain tangential to the torus. Thus, the stretching of trajectories that occurs due to the square-root term will be restricted to directions parallel to the surface of the torus,

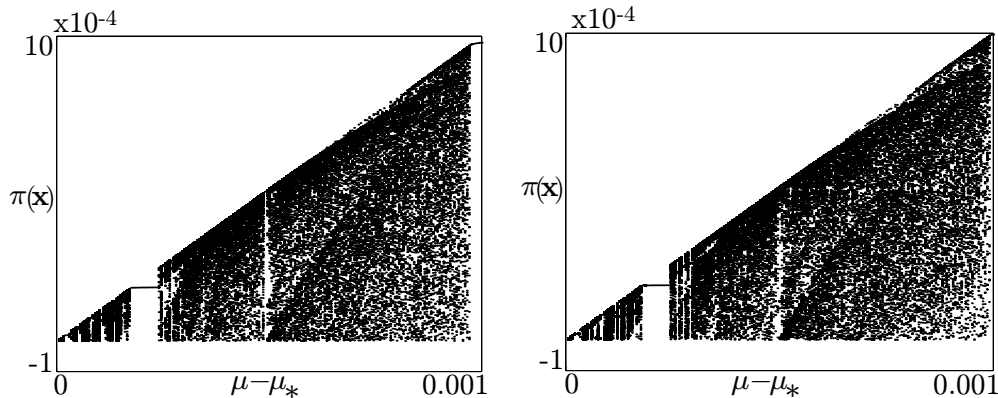


Figure 4.13: Bifurcation diagram generated using direct numerical integration of the vector field for $A = 1.5$ and $\omega = 4$ (left panel) and iterations of full composite map obtained using the discontinuity-mapping approach (right panel).

while the dynamics in a direction normal to the toral surface are governed by an expansion that is linear to lowest order. In contrast, in the case of grazing contact of a co-dimension-two-or-higher invariant torus with a discontinuity surface, significant stretching in a direction normal to the toral surface may result from successive applications of the composite Poincaré map.

Further related to the co-dimensionality of the quasiperiodic grazing attractor is the possibility of deriving a reduced map. As discussed here, while the reduced formulation appears successful in the co-dimension-one case, it typically fails for co-dimension-two or higher cases. Again, this is a result of the existence of the square-root in the dynamics transversal to the grazing attractor.

4.5 Summary

This chapter illustrated grazing bifurcation scenarios in the case of co-dimension-two invariant tori. In particular, grazing bifurcations of a periodic trajectory in a three-dimensional state space and a two-frequency quasiperiodic trajectory in a four-dimensional state space

have been analyzed using numerical integration of the vector field corresponding to the dynamical system and the discontinuity-mapping approach. The effects of the square-root term originating in the local description of the impacting dynamics on such bifurcations have been studied using these two example piecewise-smooth dynamical systems. Also, a rigorous application of the full discontinuity-mapping approach to a co-dimension-two quasiperiodic attractor resulted in a comprehensive understanding of the grazing bifurcations of quasiperiodic system attractors.

Even though grazing bifurcations of co-dimension-two periodic orbits have been extensively studied in the past by several researchers, this dissertation emphasizes the effects of the presence and orientation of the square-root term on such bifurcations. In this case the square-root term is present in the directions normal to the periodic attractor resulting in discontinuous grazing bifurcations for certain parameter values, for example, for $m = 0.28$ in the example. The attracting grazing periodic orbit loses stability at the grazing contact and the ensuing motion is an impacting orbit far away in state space from the original attracting motion. However, for $m = 0.39$ a continuous grazing bifurcation occurs in which the impacting orbit emanating from the grazing contact is close to the original periodic orbit. Also, an inverse period-adding sequence, a typical characteristic of grazing bifurcations, is seen for this case. Since the values of ξ_1 evaluated in the two cases have opposite signs, these two qualitatively different co-dimension-one grazing bifurcations are separated by a co-dimension-two grazing bifurcation point.

In the case of a co-dimension-two periodic trajectory, typically, the square-root stretching is also present in transversal directions. However, in those directions the smooth dynamics that are attracting in nature are to the lowest order linear allowing the dominance of the instability effects of stretching in the case of multiple impacts. An accumulation of the instability takes place because a finite number of iterates between two impacts cannot stabilize the instability created by the previous impact leading to the loss of the local attractor. However, it is possible that the trajectory might attain at most one impact and all the subsequent iterates fall into the nonimpacting region leading to a continuous grazing bifurcation.

In the case of co-dimension-two quasiperiodic system attractor a continuous grazing bifurcation was observed for $A = 1.1$ in the example and the bifurcation diagram shows the existence of sequence of periodic and chaotic windows. These results are also supported by the computation of Lyapunov exponents using both numerical simulation of the original dynamical system and the composite Poincaré map. However, for $A = 1.25$ a seemingly discontinuous grazing bifurcation has been observed where the impacting motion jumps to a period-2 periodic orbit with one impact per period for a small, but positive deviation from grazing. Also, it is shown that, while a reduced formulation may be employed successfully in the case of co-dimension-one attractors, it fails to capture dynamics in directions transversal to the original quasiperiodic attractor in the co-dimension-two case. Additionally, for $A = 1.5$ and $\omega = 4$, the intersection of the quasiperiodic attractor with the Poincaré section based at \mathcal{P} is a discontinuous curve resulting in the mandatory use of the Poincaré section based at \mathcal{P}' . The good agreement between the bifurcation diagrams validates the accuracy of the discontinuity-mapping based at \mathcal{P}' .

In summary, unlike co-dimension-one system attractors, co-dimension-two or higher attractors can experience discontinuous grazing bifurcations owing to the orientation of the square-root term in their transversal directions. However, in the case of co-dimension-two or higher quasiperiodic attractors the discontinuous jump is delayed past the grazing contact. Also, the failure of the reduced formulation necessitates the full machinery of the discontinuity-mapping approach in the analysis of grazing bifurcations of co-dimension-two or higher quasiperiodic attractors.

A note of numerical nature: In Chapters 3 and 4, the data plotted as the intersections of system attractors with \mathcal{P} or \mathcal{P}' represents the intersections of incoming trajectories of the smooth flow with \mathcal{P} or \mathcal{P}' , accounting for possible impacts only after collecting such points of intersection. This allows a straightforward comparison with the data predicted with the composite Poincaré map since this method of collecting data agrees with its construction. Secondly, continuation of impacting periodic orbits poses a solvable problem when

the Poincaré section is a zero level surface of a nonlinear scalar function. In this case the corrected initial condition obtained from the Newton-Raphson algorithm might no longer belong to the Poincaré section resulting in delayed convergence or no convergence at all. As a remedy to this setback, the system is integrated forward or backwards in time until the trajectory reaches the Poincaré section and the point of intersection is then used as the initial condition in solving the variational equations.

Chapter 5

TC-HAT ($\widehat{\text{TC}}$) – A Continuation Toolbox for the Analysis of Hybrid Dynamical Systems

The study of hybrid dynamical systems is mostly confined to numerical investigations involving direct numerical integration of the differential equations governing the dynamical system or the maps that model them. Such numerical schemes based on the time evolution or forward iterates of a system can only locate stable orbits. They fail to give any information about unstable orbits or the bifurcations that would lead to such. Moreover, hybrid dynamical systems are inherently nonlinear (even in the case of linear vector fields) and an effort to obtain approximate solutions typically results in enormous algebraic complexity. Therefore, there is a need for continuation methods, widely employed in the bifurcation analysis of smooth dynamical systems, to be developed and implemented for a comprehensive study of bifurcations in hybrid dynamical systems.

TC-HAT ($\widehat{\text{TC}}$) is a Fortran-based software application which is able to perform partial bifurcation analysis of hybrid dynamical systems, e.g., vibro-impact oscillators with or without friction. In this regard, $\widehat{\text{TC}}$ supersedes and improves (and, in some cases, corrects) the func-

tionality of the existing software application SLIDECONT [11], developed by Yuri Kuznetsov and Fabio Dercole for the study of hybrid dynamical systems with sliding dynamics but no state-space jumps. $\widehat{\text{TC}}$ functions as a driver to a modified version of AUTO 97, a Fortran-based software application for the bifurcation analysis of smooth dynamical systems. In particular, $\widehat{\text{TC}}$ exploits AUTO 97's generalized Boundary Value Problem formulation to locate and continue trajectories of hybrid dynamical systems and their associated bifurcation points under variations in system parameters.

5.1 Mathematical Foundation

Recall the following definition of a hybrid dynamical system and associated trajectories from Chapter 2. Specifically, a *hybrid dynamical system* assumes the existence of a state space X of dimension n and an associated vector-valued function $\mathbf{f}_{\mathbf{I}} : X \rightarrow X$ known as the *vector field*, parameterized by an *index vector* \mathbf{I} in some finite set \mathbb{F} . To each value of the index vector \mathbf{I} associate a smooth *event function* $h_{\mathbf{I}} : X \rightarrow \mathbb{R}$ and a smooth *state jump function* $\mathbf{g}_{\mathbf{I}} : X \rightarrow X$. Then, a *solution* to the corresponding dynamical system is a sequence $\{\mathbf{x}_j : (t_{j-1}, t_j] \rightarrow X\}_{j=1}^m$ of m smooth curves and an associated sequence $\{\mathbf{I}_j\}_{j=1}^m$, such that

$$\mathbf{I}(t) = \mathbf{I}_j, t \in (t_{j-1}, t_j] \quad (5.1)$$

and

1. The corresponding tangent vector at $\mathbf{x}_j(t)$ equals $\mathbf{f}_{\mathbf{I}_j}(\mathbf{x}_j(t))$, i.e., in the case of $X = \mathbb{R}^n$

$$\frac{d}{dt}\mathbf{x}_j(t) = \mathbf{f}_{\mathbf{I}_j}(\mathbf{x}_j(t)). \quad (5.2)$$

2. The j -th segment terminates at an intersection with the *event surface*

$$\{\mathbf{x} \mid h_{\mathbf{I}_j}(\mathbf{x}) = 0, h_{\mathbf{I}_j, \mathbf{x}}(\mathbf{x}) \cdot \mathbf{f}_{\mathbf{I}_j}(\mathbf{x}) \leq 0\}, \quad (5.3)$$

i.e.,

$$h_{\mathbf{I}_j}(\mathbf{x}_j(t_j)) = 0. \quad (5.4)$$

3. The *connectivity* between the j -th and $j + 1$ -th segments is given by the function $\mathbf{g}_{\mathbf{I}_j}$, i.e.,

$$\mathbf{g}_{\mathbf{I}_j}(\mathbf{x}_j(t_j)) = \lim_{t \rightarrow t_{j+}^+} \mathbf{x}_{j+1}(t). \quad (5.5)$$

The sequence $\Sigma = \{\mathbf{I}_j\}_{j=1}^m$ of values of the index vector is called the solution's *signature*. Here, we allow for the possibility of infinite solution sequences and the replacement of m by ∞ .

5.1.1 Problem Formulations

The General Boundary-Value Problem

The general boundary-value problem formulation in $\widehat{\text{TC}}$ can then be formulated as the task of finding a trajectory of a hybrid dynamical system with a prescribed signature satisfying the auxiliary boundary conditions

$$\mathbf{g} \left(\lim_{t \rightarrow t_0^+} \mathbf{x}_1(t), \mathbf{x}_m(t_m) \right) = \mathbf{0} \quad (5.6)$$

for some function \mathbf{g} and any number of additional equations (typically generalized integral equations) corresponding to the introduction of free system parameters.

Periodic Trajectories

Consider the task of finding a periodic trajectory of a hybrid dynamical system with a prescribed signature with a length m base unit. Then, the auxiliary boundary condition corresponds to the connectivity condition

$$\lim_{t \rightarrow t_0^+} \mathbf{x}_1(t) - \mathbf{g}_{\mathbf{I}_m}(\mathbf{x}_m(t_m)) = \mathbf{0}. \quad (5.7)$$

Grazing Trajectories and Bifurcation Points

Alternatively, consider the task of finding a trajectory of a hybrid dynamical system with a prescribed signature in the presence of a single free parameter, such that

$$h_{\mathcal{D}}(\mathbf{x}_j(t_j)) = 0 \quad (5.8)$$

for some j . In particular, suppose that, for some value of the free parameter, a trajectory has been found that achieves approximate grazing contact at a point \mathbf{x}_* with an event surface \mathcal{D} corresponding to the event function $h_{\mathcal{D}}$, such that (without loss of generality)

$$h_{\mathcal{P},\mathbf{x}}(\mathbf{x}_*) \cdot \mathbf{f}_{\mathbf{I}_j}(\mathbf{x}_*) \quad (5.9)$$

is distinctly negative, where

$$h_{\mathcal{P}}(\mathbf{x}) = h_{\mathcal{D},\mathbf{x}}(\mathbf{x}) \cdot \mathbf{f}_{\mathbf{I}_j}(\mathbf{x}). \quad (5.10)$$

Then replace the j -th segment and j -th index vector, with two segments $\mathbf{x}_{j'}$ and $\mathbf{x}_{j''}$ with index vectors $\mathbf{I}_{j'}$ and $\mathbf{I}_{j''}$, such that $h_{\mathbf{I}_{j'}} = h_{\mathcal{P}}$, $h_{\mathbf{I}_{j''}} = h_{\mathbf{I}_j}$, $\mathbf{f}_{\mathbf{I}_{j'}} = \mathbf{f}_{\mathbf{I}_{j''}} = \mathbf{f}_{\mathbf{I}_j}$, $\mathbf{g}_{\mathbf{I}_{j''}} = \mathbf{g}_{\mathbf{I}_j}$ and $\mathbf{g}_{\mathbf{I}_{j'}}$ is the identity. Then, the above problem formulation serves to locate the parameter value and the trajectory corresponding to actual grazing contact.

Saddle-node Bifurcation Points

Alternatively, consider the task of finding a periodic trajectory of a hybrid dynamical system with a prescribed signature with a length m base unit Σ in the presence of two free parameters, such that

$$\mathbf{g}_{\mathbf{I}_m,\mathbf{x}}(\mathbf{x}_m(t_m)) \cdot \mathbf{P}_{\Sigma,\mathbf{x}} \left(\lim_{t \rightarrow t_0^+} \mathbf{x}_1(t) \right) \quad (5.11)$$

has an eigenvector corresponding to the eigenvalue 1.

For this purpose, consider the augmented hybrid dynamical system with state space $\tilde{X} = X \times X$ and an associated vector field $\tilde{\mathbf{f}}_{\mathbf{I}} : \tilde{X} \rightarrow \tilde{X}$ parameterized by the original index

vector \mathbf{I} , where

$$\tilde{\mathbf{f}}_{\mathbf{I}}(\tilde{\mathbf{x}}) = \begin{pmatrix} \mathbf{f}_{\mathbf{I}}(\mathbf{u}) \\ \mathbf{f}_{\mathbf{I},\mathbf{x}}(\mathbf{u}) \cdot \mathbf{v} \end{pmatrix}, \tilde{\mathbf{x}} = \begin{pmatrix} \mathbf{u} \\ \mathbf{v} \end{pmatrix}. \quad (5.12)$$

Moreover, let $\tilde{h}_{\mathbf{I}}(\tilde{\mathbf{x}}) = h_{\mathbf{I}}(\mathbf{u})$ and

$$\tilde{\mathbf{g}}_{\mathbf{I}_j}(\tilde{\mathbf{x}}) = \begin{pmatrix} \mathbf{g}_{\mathbf{I}_j}(\mathbf{u}) \\ \mathbf{g}_{\mathbf{I}_j,\mathbf{x}}(\mathbf{u}) \cdot \left(Id - \frac{\mathbf{f}_{\mathbf{I}_j}(\mathbf{u}) \cdot h_{\mathbf{I}_j,\mathbf{x}}(\mathbf{u})}{h_{\mathbf{I}_j,\mathbf{x}}(\mathbf{u}) \cdot \mathbf{f}_{\mathbf{I}_j}(\mathbf{u})} \right) \cdot \mathbf{v} \end{pmatrix}. \quad (5.13)$$

The task of finding a periodic trajectory of the original hybrid dynamical system with the desired property can then be formulated as the task of finding a trajectory of the augmented hybrid dynamical system with the identical signature satisfying the auxiliary boundary conditions

$$\lim_{t \rightarrow t_0^+} \mathbf{u}_1(t) - \mathbf{g}_{\mathbf{I}_m}(\mathbf{u}_m(t_m)) = \mathbf{0}, \quad (5.14)$$

$$\lim_{t \rightarrow t_0^+} \mathbf{v}_1(t) - \mathbf{g}_{\mathbf{I}_m,\mathbf{x}}(\mathbf{u}_m(t_m)) \cdot \left(Id - \frac{\mathbf{f}_{\mathbf{I}_m}(\mathbf{u}_m(t_m)) \cdot h_{\mathbf{I}_m,\mathbf{x}}(\mathbf{u}_m(t_m))}{h_{\mathbf{I}_m,\mathbf{x}}(\mathbf{u}_m(t_m)) \cdot \mathbf{f}_{\mathbf{I}_m}(\mathbf{u}_m(t_m))} \right) \cdot \mathbf{v}_m(t_m) = \mathbf{0} \quad (5.15)$$

and the integral condition

$$\sum_{j=1}^m \int_{t_{j-1}}^{t_j} \|\mathbf{v}_j(t)\|^2 dt = 1. \quad (5.16)$$

Period-doubling Bifurcation Points

Finally, consider the task of finding a periodic trajectory of a hybrid dynamical system with a prescribed signature in the presence of two free parameters, such that

$$\mathbf{g}_{\mathbf{I}_m,\mathbf{x}}(\mathbf{x}_m(t_m)) \cdot \mathbf{P}_{\Sigma,\mathbf{x}} \left(\lim_{t \rightarrow t_0^+} \mathbf{x}_1(t) \right) \quad (5.17)$$

has an eigenvector corresponding to the eigenvalue -1 .

For this purpose, consider the augmented hybrid dynamical system with state space $\tilde{X} = X \times X$ and an associated vector field $\tilde{\mathbf{f}}_{\mathbf{I}} : \tilde{X} \rightarrow \tilde{X}$ parameterized by the original index vector \mathbf{I} , where

$$\tilde{\mathbf{f}}_{\mathbf{I}}(\tilde{\mathbf{x}}) = \begin{pmatrix} \mathbf{f}_{\mathbf{I}}(\mathbf{u}) \\ \mathbf{f}_{\mathbf{I},\mathbf{x}}(\mathbf{u}) \cdot \mathbf{v} \end{pmatrix}, \tilde{\mathbf{x}} = \begin{pmatrix} \mathbf{u} \\ \mathbf{v} \end{pmatrix}. \quad (5.18)$$

Moreover, let $\tilde{h}_{\mathbf{I}}(\tilde{\mathbf{x}}) = h_{\mathbf{I}}(\mathbf{x})$ and

$$\tilde{\mathbf{g}}_{\mathbf{I}_j}(\tilde{\mathbf{x}}) = \begin{pmatrix} \mathbf{g}_{\mathbf{I}_j}(\mathbf{u}) \\ \mathbf{g}_{\mathbf{I}_j, \mathbf{x}}(\mathbf{u}) \cdot \left(Id - \frac{\mathbf{f}_{\mathbf{I}_j}(\mathbf{u}) \cdot h_{\mathbf{I}_j, \mathbf{x}}(\mathbf{u})}{h_{\mathbf{I}_j, \mathbf{x}}(\mathbf{u}) \cdot \mathbf{f}_{\mathbf{I}_j}(\mathbf{u})} \right) \cdot \mathbf{v} \end{pmatrix}. \quad (5.19)$$

The task of finding a periodic trajectory of the original hybrid dynamical system with the desired property can then be formulated as the task of finding a trajectory of the augmented hybrid dynamical system with the identical signature satisfying the auxiliary boundary conditions

$$\lim_{t \rightarrow t_0^+} \mathbf{u}_1(t) - \mathbf{g}_{\mathbf{I}_m}(\mathbf{u}_m(t_m)) = \mathbf{0}, \quad (5.20)$$

$$\lim_{t \rightarrow t_0^+} \mathbf{v}_1(t) + \mathbf{g}_{\mathbf{I}_m, \mathbf{x}}(\mathbf{u}_m(t_m)) \cdot \left(Id - \frac{\mathbf{f}_{\mathbf{I}_m}(\mathbf{u}_m(t_m)) \cdot h_{\mathbf{I}_m, \mathbf{x}}(\mathbf{u}_m(t_m))}{h_{\mathbf{I}_m, \mathbf{x}}(\mathbf{u}_m(t_m)) \cdot \mathbf{f}_{\mathbf{I}_m}(\mathbf{u}_m(t_m))} \right) \cdot \mathbf{v}_m(t_m) = \mathbf{0} \quad (5.21)$$

and the integral condition

$$\sum_{j=1}^m \int_{t_{j-1}}^{t_j} \|\mathbf{v}_j(t)\|^2 dt = 1. \quad (5.22)$$

5.1.2 Solving Boundary-Value-Problems (BVP's) using Collocation Methods

Collocation methods in general and piecewise polynomial collocation methods in particular provide an accurate and highly adaptive procedure to compute solutions of boundary value problems involving differential equations. In this method, approximants of the form of piecewise polynomials of some predetermined order are sought that satisfy the given differential equation at a discrete set of points in the interval of definition, the *collocation points*. The robustness of this method has made it an indisputable candidate in solving some of the difficult problems in differential equations.

Specifically, consider the differential equation

$$\frac{d\mathbf{x}}{dt} = \mathbf{f}(\mathbf{x}) \quad (5.23)$$

for some vector field \mathbf{f} and denote by $\mathbf{x}(t)$ a solution on the interval $[0, T]$ for some $T > 0$. In an effort to discretize the problem of determining $\mathbf{x}(t)$ given appropriate boundary conditions, introduce the partition

$$0 = t_0 < t_{1/m} < \cdots < t_1 < t_{1+1/m} < \cdots < t_2 < \cdots < t_N = T \quad (5.24)$$

for some integers N and m and let

$$\Delta_j = t_j - t_{j-1} \quad (5.25)$$

for $j = 1, \dots, N$ (cf. Fig. 5.1).

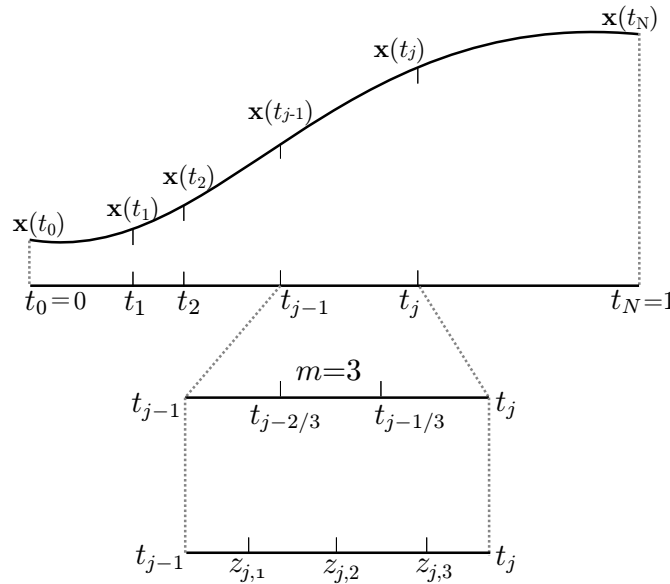


Figure 5.1: Mesh intervals corresponding to a solution trajectory. The extended mesh intervals $t_{j-2/3}$ and $t_{j-1/3}$ and the collocation points $z_{j,i}$ are also shown in the figure.

On each interval $[t_{j-1}, t_j]$, define the Lagrange polynomials

$$l_{j,i}(t) = \prod_{k=0, k \neq i}^m \frac{t - t_{j-k/m}}{t_{j-i/m} - t_{j-k/m}} \quad (5.26)$$

for $i = 0, \dots, m$ and $j = 1, \dots, N$ (see Fig. 5.2 for the Lagrange polynomials in the case of $m = 3$). In particular, $l_{j,i}(t_{j-i/m}) = 1$ and $l_{j,i}(t_{j-k/m}) = 0$ for $k \neq i$. Then, the piecewise

polynomial function $\mathbf{p}(t)$ such that

$$\mathbf{p}(t) = \sum_{i=0}^m l_{j,i}(t) \mathbf{x}(t_{j-i/m}) \quad (5.27)$$

for $t \in [t_{j-1}, t_j]$, interpolates the unknown function $\mathbf{x}(t)$ at the points $\mathbf{x}(t_{j-i/m})$ for $j = 1, \dots, N$, $i = 0, \dots, m$.

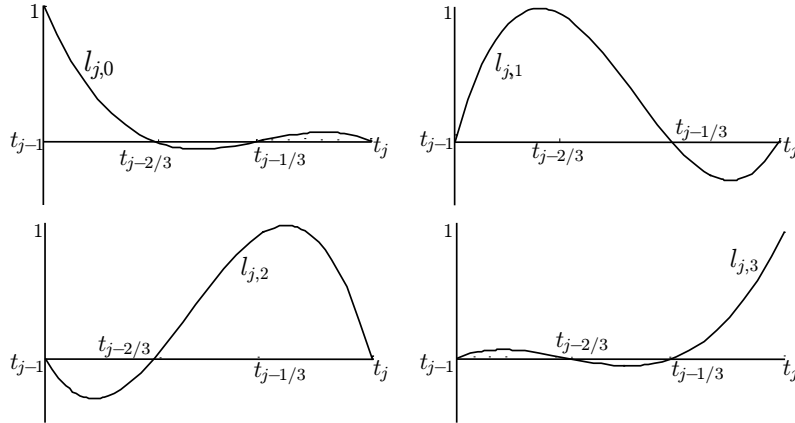


Figure 5.2: Lagrange basis polynomials corresponding to the mesh $[t_{j-1}, t_j]$.

Now, consider the m -th order Legendre polynomial on the interval $[0, 1]$ and denote its roots by z_i , $i = 1, \dots, m$. For each interval $[t_{j-1}, t_j]$, define $z_{i,j}$ as

$$z_{i,j} = t_{j-1} + z_i \Delta_j. \quad (5.28)$$

Then, an approximation to the solution to the original differential equation is obtained by seeking the $n(mN + 1)$ discrete values of the components of the unknown function $\mathbf{x}(t)$ at $t_{j-i/m}$ for $j = 1, \dots, N$, $i = 1, \dots, m$ and t_N so that the piecewise polynomial function $\mathbf{p}(t)$ satisfies the system of nmN equations

$$\mathbf{p}'(z_{j,i}) - \mathbf{f}(\mathbf{p}(z_{j,i})) = \mathbf{0} \quad (5.29)$$

for $j = 1, \dots, N$ and $i = 1, \dots, m$ and the associated n boundary conditions.

Denote by \mathbf{x}_0 an initial guess for the vector consisting of the concatenation of the unknown discretization values $\mathbf{x}(t_{j-i/m})$. Then an improved estimate for the solution vector \mathbf{x}

may be obtained by the addition of a correction $\Delta \mathbf{x}$, where

$$\mathbf{J}(\mathbf{x}_0) \cdot \Delta \mathbf{x} = -\mathbf{F}(\mathbf{x}_0) \quad (5.30)$$

corresponding to a Newton-Raphson-based iteration. Here, $\mathbf{F}(\mathbf{x}_0)$ is the vector of residuals of the set of equations and $\mathbf{J}(\mathbf{x}_0)$ is the Jacobian matrix of the equations with respect to \mathbf{x} evaluated at the point \mathbf{x}_0 . The inversion of the linear equation for $\Delta \mathbf{x}$ may be conveniently obtained using *Gauss elimination*. The process is then iterated until the residual vector \mathbf{F} is within the required tolerance limits.

Single-segment Trajectories

Suppose, for simplicity, that $n = m = N = 2$. In this case,

$$\mathbf{p}(t) = \begin{cases} l_{1,0}(t) \mathbf{x}_0 + l_{1,1}(t) \mathbf{x}_{1/2} + l_{1,2}(t) \mathbf{x}_1 & t \in [t_0, t_1] \\ l_{2,0}(t) \mathbf{x}_1 + l_{2,1}(t) \mathbf{x}_{3/2} + l_{2,2}(t) \mathbf{x}_2 & t \in [t_1, t_2] \end{cases}, \quad (5.31)$$

where \mathbf{x}_0 , $\mathbf{x}_{1/2}$, \mathbf{x}_1 , $\mathbf{x}_{3/2}$, and \mathbf{x}_2 are the unknown values of the approximant at $t = t_0$, $t = t_{1/2}$, $t = t_1$, $t = t_{3/2}$, and $t = t_2$, respectively. Let

$$\alpha_{j,i,k} = l'_{j,i}(t_{j-1} + z_k \Delta_j) \quad (5.32)$$

and

$$\beta_{j,i,k} = l_{j,i}(t_{j-1} + z_k \Delta_j) \quad (5.33)$$

for $j = 1, 2$, $i = 0, 1, 2$, and $k = 1, 2$. Then, the discretized differential equations become

$$\alpha_{0,0,1} \mathbf{x}_0 + \alpha_{0,1,1} \mathbf{x}_{1/2} + \alpha_{0,2,1} \mathbf{x}_1 - \mathbf{f}(\beta_{0,0,1} \mathbf{x}_0 + \beta_{0,1,1} \mathbf{x}_{1/2} + \beta_{0,2,1} \mathbf{x}_1) = \mathbf{0}, \quad (5.34)$$

$$\alpha_{0,0,2} \mathbf{x}_0 + \alpha_{0,1,2} \mathbf{x}_{1/2} + \alpha_{0,2,2} \mathbf{x}_1 - \mathbf{f}(\beta_{0,0,2} \mathbf{x}_0 + \beta_{0,1,2} \mathbf{x}_{1/2} + \beta_{0,2,2} \mathbf{x}_1) = \mathbf{0}, \quad (5.35)$$

$$\alpha_{1,0,1} \mathbf{x}_1 + \alpha_{1,1,1} \mathbf{x}_{3/2} + \alpha_{1,2,1} \mathbf{x}_2 - \mathbf{f}(\beta_{1,0,1} \mathbf{x}_1 + \beta_{1,1,1} \mathbf{x}_{3/2} + \beta_{1,2,1} \mathbf{x}_2) = \mathbf{0}, \quad (5.36)$$

$$\alpha_{1,0,2} \mathbf{x}_1 + \alpha_{1,1,2} \mathbf{x}_{3/2} + \alpha_{1,2,2} \mathbf{x}_2 - \mathbf{f}(\beta_{1,0,2} \mathbf{x}_1 + \beta_{1,1,2} \mathbf{x}_{3/2} + \beta_{1,2,2} \mathbf{x}_2) = \mathbf{0}. \quad (5.37)$$

The Jacobian matrix of the above equations w.r.t. the unknowns \mathbf{x}_0 , $\mathbf{x}_{1/2}$, \mathbf{x}_1 , $\mathbf{x}_{3/2}$, and \mathbf{x}_2 has the form (in the matrix below $\mathcal{I}_{j,i,k} = \alpha_{j,i,k} Id$)

$$\begin{pmatrix} \mathcal{I}_{0,0,1} - \beta_{0,0,1}\mathbf{f}_{,\mathbf{x}}, & \mathcal{I}_{0,1,1} - \beta_{0,1,1}\mathbf{f}_{,\mathbf{x}} & \mathcal{I}_{0,2,1} - \beta_{0,2,1}\mathbf{f}_{,\mathbf{x}} & \mathbf{0} & \mathbf{0} \\ \mathcal{I}_{0,0,2} - \beta_{0,0,2}\mathbf{f}_{,\mathbf{x}} & \mathcal{I}_{0,1,2} - \beta_{0,1,2}\mathbf{f}_{,\mathbf{x}} & \mathcal{I}_{0,2,2} - \beta_{0,2,2}\mathbf{f}_{,\mathbf{x}} & \mathbf{0} & \mathbf{0} \\ \mathbf{0} & \mathbf{0} & \mathcal{I}_{1,0,1} - \beta_{1,0,1}\mathbf{f}_{,\mathbf{x}} & \mathcal{I}_{1,1,1} - \beta_{1,1,1}\mathbf{f}_{,\mathbf{x}} & \mathcal{I}_{1,2,1} - \beta_{1,2,1}\mathbf{f}_{,\mathbf{x}} \\ \mathbf{0} & \mathbf{0} & \mathcal{I}_{1,0,2} - \beta_{1,0,2}\mathbf{f}_{,\mathbf{x}} & \mathcal{I}_{1,1,2} - \beta_{1,1,2}\mathbf{f}_{,\mathbf{x}} & \mathcal{I}_{1,2,2} - \beta_{1,2,2}\mathbf{f}_{,\mathbf{x}} \end{pmatrix} \quad (5.38)$$

Here, $\mathbf{f}_{,\mathbf{x}}$ is a 2×2 matrix corresponding to the Jacobian matrix of the vector field \mathbf{f} with respect to its argument and $\mathbf{0}$ is 2×2 zero matrix. In its expanded form, the Jacobian matrix is a 8×10 matrix of the form

$$A = \begin{pmatrix} a_{11} & a_{12} & a_{13} & a_{14} & a_{15} & a_{16} & 0 & 0 & 0 & 0 \\ a_{21} & a_{22} & a_{23} & a_{24} & a_{25} & a_{26} & 0 & 0 & 0 & 0 \\ a_{31} & a_{32} & a_{33} & a_{34} & a_{35} & a_{36} & 0 & 0 & 0 & 0 \\ a_{41} & a_{42} & a_{43} & a_{44} & a_{45} & a_{46} & 0 & 0 & 0 & 0 \\ 0 & 0 & 0 & 0 & a_{55} & a_{56} & a_{57} & a_{58} & a_{59} & a_{510} \\ 0 & 0 & 0 & 0 & a_{65} & a_{66} & a_{67} & a_{68} & a_{69} & a_{610} \\ 0 & 0 & 0 & 0 & a_{75} & a_{76} & a_{77} & a_{78} & a_{79} & a_{710} \\ 0 & 0 & 0 & 0 & a_{85} & a_{86} & a_{87} & a_{88} & a_{89} & a_{810} \end{pmatrix} \quad (5.39)$$

Here, for each non-zero block, the first two and the last two columns correspond to the mesh points \mathbf{x}_0 , \mathbf{x}_1 , and \mathbf{x}_2 and the intermediate columns correspond to the points $\mathbf{x}_{1/2}$ and $\mathbf{x}_{3/2}$. Denote by A_i the i -th row of A and consider the following sequence of parallel steps of *Gauss*

elimination.

$$B_3 = A_3 + A_1 \left(-\frac{a_{24} a_{33} - a_{23} a_{34}}{-a_{14} a_{23} + a_{13} a_{24}} \right) + A_2 \left(-\frac{a_{14} a_{33} - a_{13} a_{34}}{a_{14} a_{23} - a_{13} a_{24}} \right) \quad (5.40)$$

$$B_4 = A_4 + A_1 \left(-\frac{a_{24} a_{43} - a_{23} a_{44}}{-a_{14} a_{23} + a_{13} a_{24}} \right) + A_2 \left(-\frac{a_{14} a_{43} - a_{13} a_{44}}{a_{14} a_{23} - a_{13} a_{24}} \right) \quad (5.41)$$

$$B_2 = A_2 a_{13} + A_1 (-a_{23}) \quad (5.42)$$

$$B_7 = A_7 + A_5 \left(-\frac{a_{68} a_{77} - a_{67} a_{78}}{-a_{58} a_{67} + a_{57} a_{68}} \right) + A_6 \left(-\frac{a_{58} a_{77} - a_{57} a_{78}}{a_{58} a_{67} - a_{57} a_{68}} \right) \quad (5.43)$$

$$B_8 = A_8 + A_5 \left(-\frac{a_{68} a_{87} - a_{67} a_{88}}{-a_{58} a_{67} + a_{57} a_{68}} \right) + A_6 \left(-\frac{a_{58} a_{87} - a_{57} a_{88}}{a_{58} a_{67} - a_{57} a_{68}} \right) \quad (5.44)$$

$$B_6 = A_6 a_{57} + A_1 (-a_{67}) \quad (5.45)$$

The resultant reduced matrix now takes the form

$$B = \begin{pmatrix} b_{11} & b_{12} & b_{13} & b_{14} & b_{15} & b_{16} & 0 & 0 & 0 & 0 \\ b_{21} & b_{22} & 0 & b_{24} & b_{25} & b_{26} & 0 & 0 & 0 & 0 \\ b_{31} & b_{32} & 0 & 0 & b_{35} & b_{36} & 0 & 0 & 0 & 0 \\ b_{41} & b_{42} & 0 & 0 & b_{45} & b_{46} & 0 & 0 & 0 & 0 \\ 0 & 0 & 0 & 0 & b_{55} & b_{56} & b_{57} & b_{58} & b_{59} & b_{510} \\ 0 & 0 & 0 & 0 & b_{65} & b_{66} & 0 & b_{68} & b_{69} & b_{610} \\ 0 & 0 & 0 & 0 & b_{75} & b_{76} & 0 & 0 & b_{79} & b_{710} \\ 0 & 0 & 0 & 0 & b_{85} & b_{86} & 0 & 0 & b_{89} & b_{810} \end{pmatrix}. \quad (5.46)$$

By a similar set of row-reduction operations, we arrive at a matrix of the form

$$C = \begin{pmatrix} c_{11} & c_{12} & c_{13} & c_{14} & c_{15} & c_{16} & 0 & 0 & 0 & 0 \\ c_{21} & c_{22} & 0 & c_{24} & c_{25} & c_{26} & 0 & 0 & 0 & 0 \\ c_{31} & c_{32} & 0 & 0 & c_{35} & c_{36} & 0 & 0 & 0 & 0 \\ c_{41} & c_{42} & 0 & 0 & 0 & c_{46} & 0 & 0 & 0 & 0 \\ 0 & 0 & 0 & 0 & c_{55} & c_{56} & c_{57} & c_{58} & c_{59} & c_{510} \\ 0 & 0 & 0 & 0 & c_{65} & c_{66} & 0 & c_{68} & c_{69} & c_{610} \\ c_{71} & c_{72} & 0 & 0 & 0 & 0 & 0 & 0 & c_{79} & c_{710} \\ c_{81} & c_{82} & 0 & 0 & 0 & 0 & 0 & 0 & c_{89} & c_{810} \end{pmatrix} \quad (5.47)$$

The two block matrices $P_0 = \begin{pmatrix} c_{71} & c_{72} \\ c_{81} & c_{82} \end{pmatrix}$ and $P_1 = \begin{pmatrix} c_{79} & c_{710} \\ c_{89} & c_{810} \end{pmatrix}$ relate the variations in the terminal point \mathbf{x}_2 to the initial point \mathbf{x}_0 of the solution trajectory. Specifically, when evaluated on the converged solution, P_0 and P_1 satisfy

$$P_0 \cdot \Delta \mathbf{x}_0 + P_1 \cdot \Delta \mathbf{x}_2 = 0 \quad (5.48)$$

which implies that

$$\Delta \mathbf{x}_2 = -(P_1)^{-1} \cdot P_0 \cdot \Delta \mathbf{x}_0 \quad (5.49)$$

Hence, the matrix $-(P_1)^{-1} \cdot P_0$ gives the lowest-order relationship between perturbations in the initial point \mathbf{x}_0 and deviations in the corresponding terminal point \mathbf{x}_2 .

Multisegment Trajectories

In the case of multisegment trajectories in hybrid dynamical systems, each segment may be treated independently from every other segment when formulating the piecewise polynomial approximant and the associated discretized differential equations. The connectivity between subsequent segments enters the boundary-value problem formulation through the boundary conditions. It follows that the sequence of Gauss elimination operations described previously can be applied for each segment independently of each other segment. Thus the Jacobian $\Phi_{\mathbf{I}, \mathbf{x}}(\lim_{t \rightarrow t_{j-1}^+} \mathbf{x}_j(t), t_j - t_{j-1})$ of the flow function that describes the sensitivity of the terminal point $\mathbf{x}_j(t_j)$ of the j -th segment to changes in the initial point $\lim_{t \rightarrow t_{j-1}^+} \mathbf{x}_j(t)$ may be obtained from the corresponding product $-(P_1)^{-1} \cdot P_0$.

In the $\widehat{\text{TC}}$ implementation, the differential equations corresponding to individual segments are all combined to a single set of differential equations in an augmented solution vector consisting of each of the solutions to the individual equations. Moreover, the time variable is rescaled for each segment, so that the initial and terminal points correspond to $t = 0$ and $t = 1$, respectively. Now discretization of the solution vector is achieved by a partition of the time interval that is identical for each of the segments.

Consider, for example, the case of a two-segment trajectory in two dimensions and let $m = N = 2$. Then, the Jacobian of the augmented boundary value problem (not including any boundary or integral conditions) has the form shown in Fig. 5.3. Following a series of

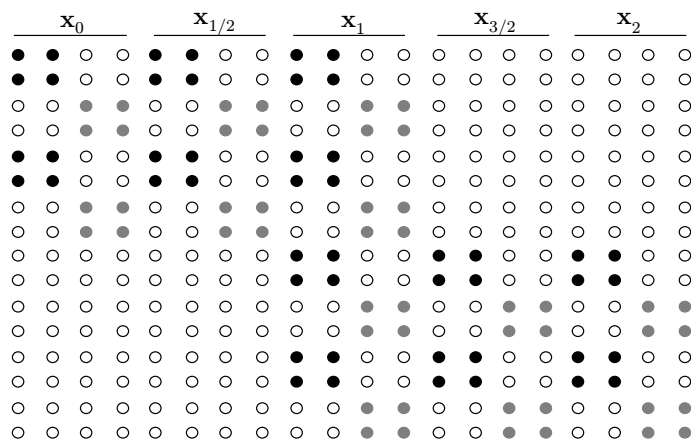


Figure 5.3: Jacobian corresponding to the linearized boundary value problem of a two-segment hybrid dynamical system. Here, any non-zero entry is represented as a black or a grey dot. Moreover, the black dots correspond to one segment and the grey dots corresponds to the other.

parallel row operations, the Jacobian matrix shown in Fig. 5.3 transforms into a matrix as shown in Fig. 5.4. The block diagonal matrices P_1 and P_0 again relate the variations in the terminal point \mathbf{x}_2 to the initial point \mathbf{x}_0 of the solution trajectory independently for each segment.

In the standard implementation of AUTO 97, the Lyapunov stability properties of a periodic orbit are determined through a computation of the eigenvalues of the Jacobian $\Phi_{,\mathbf{x}}(\mathbf{x}_0, T)$, where \mathbf{x}_0 is a point on the periodic orbit and T is the period. Whereas SLIDE-CONT ([11]) relies on a multisegment formulation similar to that described for $\widehat{\text{TC}}$ it fails to accurately account for the corrections to the flow Jacobian shown in Eqs. (2.109-2.110). In contrast, $\widehat{\text{TC}}$ ships with a modified version of AUTO 97 that includes these corrections and, consequently, is able to accurately characterize the linearized stability properties of periodic trajectories of hybrid dynamical systems.

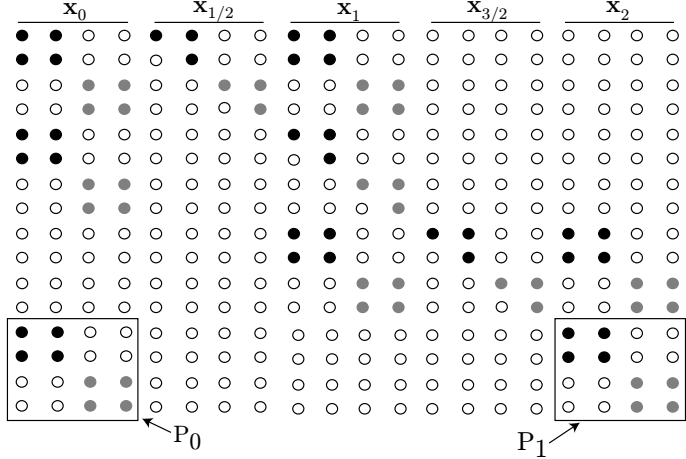


Figure 5.4: The matrix obtained from the matrix in Fig. 5.3 after a set of parallel operations corresponding to Gauss elimination.

5.1.3 Pseudo-Arclength Continuation

Given a boundary-value problem formulation, *continuation methods* serve to locate and trace the solution under variations in a system parameter. A variety of continuation procedures such as sequential continuation [26], Davidenko-Newton-Raphson continuation [12], arclength continuation etc. are available in the literature. The pseudo-arclength continuation scheme, proposed by Keller [24, 25], is a widely used method in the continuation of periodic trajectories of dynamical systems under parameter changes. (Refer [32] for detailed explanation of the Arclength and the Pseudo-arclength continuation procedures.)

Specifically, denote by $\mathbf{F}(\mathbf{x}, \mu) = \mathbf{0}$ a discretized version of the boundary-value problem parametrized by a vector of system parameters μ . Suppose that a solution \mathbf{x}_* has been found for some choice of values μ_* of the vector of system parameters. Suppose, moreover that the nullspace of the matrix

$$\begin{pmatrix} \mathbf{F}_{,\mathbf{x}}(\mathbf{x}_*, \mu_*) & \mathbf{F}_{,\mu}(\mathbf{x}_*, \mu_*) \end{pmatrix} \tag{5.50}$$

is one-dimensional and spanned by the vector

$$\tau = \begin{pmatrix} \mathbf{t}_{\mathbf{x}} \\ \mathbf{t}_{\mu} \end{pmatrix}. \tag{5.51}$$

It follows that $\mathbf{x} = \mathbf{x}_*$, $\mu = \mu_*$, and $\lambda = 0$ is a solution to the equation

$$\tilde{\mathbf{F}}(\mathbf{x}, \mu, \lambda) \stackrel{def}{=} \begin{pmatrix} \mathbf{F}(\mathbf{x}, \mu) \\ \left(\begin{matrix} \mathbf{x} - \mathbf{x}_* & \mu - \mu_* \end{matrix} \right) \cdot \boldsymbol{\tau} - \lambda \end{pmatrix} = \begin{pmatrix} \mathbf{0} \\ 0 \end{pmatrix}. \quad (5.52)$$

and that

$$\tilde{\mathbf{F}}_{(\mathbf{x}, \mu)}(\mathbf{x}_*, \mu_*, 0) = \begin{pmatrix} \mathbf{F}_{,\mathbf{x}}(\mathbf{x}_*, \mu_*) & \mathbf{F}_{,\mu}(\mathbf{x}_*, \mu_*) \\ \mathbf{t}_{\mathbf{x}} & \mathbf{t}_{\mu} \end{pmatrix} \quad (5.53)$$

is invertible. By the implicit function theorem, it follows that for every $\lambda \approx 0$, there exists a unique fixed point $\mathbf{x}(\lambda) \approx \mathbf{x}(0) = \mathbf{x}_*$ corresponding to the value $\mu(\lambda) \approx \mu(0) = \mu_*$ of the vector of system parameters.

During continuation, a Newton-Raphson-based iterative scheme may now be applied to the tangent predictor

$$\mathbf{x}(\lambda) \approx \mathbf{x}_* + \lambda \mathbf{t}_{\mathbf{x}} \quad (5.54)$$

$$\mu(\lambda) \approx \mu_* + \lambda \mathbf{t}_{\mu} \quad (5.55)$$

so as to locate the actual solution along a normal direction to $\boldsymbol{\tau}$. This methodology, which guarantees the successful continuation of solutions near singular points such as saddle-node bifurcations, is implemented in AUTO 97 to continue equilibria and periodic solutions under parameter changes.

5.2 $\widehat{\text{TC}}$ Functions

$\widehat{\text{TC}}$ facilitates bifurcation analysis of periodic trajectories in hybrid dynamical systems. $\widehat{\text{TC}}$ can perform the following specific tasks:

1. Continue a multisegment periodic trajectory of a hybrid dynamical system with a given signature under single-parameter variations while characterizing its Lyapunov stability and detecting saddle-node and period-doubling bifurcations as well as grazing incidence of a trajectory segment with a given event surface.

2. Continue multisegment periodic trajectories of a hybrid dynamical system with grazing incidence under two-parameter variations while detecting co-dimension-two grazing bifurcations.
3. Continue multisegment periodic trajectories of a hybrid dynamical system corresponding to saddle-node or period-doubling bifurcation points under two-parameter variations.

$\widehat{\text{TC}}$ resembles in its fundamental structure the implementation of SLIDECONT. Of the three main continuation tasks of $\widehat{\text{TC}}$ outlined above, however, SLIDECONT is only able to partially perform task 1 and 2. In particular, SLIDECONT is not able to handle nontrivial state jump functions or characterize the Lyapunov stability of periodic trajectories.

5.2.1 Single-parameter Continuation

In order to perform the first task corresponding to the single-parameter continuation of a multisegment periodic trajectory of a hybrid dynamical system, the user must supply three text files¹, `gc.<name>`, `<name>.f`, `<name>.dat`. Specifically, the `gc.<name>` file contains a set of numerical flags and parameter values that govern the continuation process. A description of these constants is given below.

1. GCNDIM - Dimension corresponding to each segment
2. GCIPS - $\widehat{\text{TC}}$ problem type to be solved
3. GCIRS - Label for the starting solution
4. ILP - Flag for the detection of saddle-node bifurcations
5. GCNICP - Number of continuation parameters

¹Here, `<name>` corresponds to the user-specified name of a file.

6. GCICP - Vector containing the continuation parameters
7. NTST - Number of mesh intervals for each segment
8. NCOL - Number of collocation points for each interval
9. IAD - Flag to control the mesh adaptation
10. ISP - Flag to control the detection of bifurcation points
11. ISW - Flag to control the branch switching at bifurcation points
12. IPLT - Flag to control the definition of the solution measure
13. NBC - Number of boundary conditions specified by the user
14. NINT - Number of integral conditions specified by the user
15. NMX - Maximum number of steps in the principal continuation parameter
16. RL0 - Lower bound on the principal continuation parameter
17. RL1 - Upper bound on the principal continuation parameter
18. A0 - Lower bound on the principal solution measure
19. A1 - Upper bound on the principal solution measure
20. NPR - Flag to control the printing the output to fort.8 (p.<name>) file
21. MXBF - Flag to control the maximum number of bifurcations for algebraic problems
22. IID - Flag to control the printing the output to fort.9 (p.<name>) file
23. ITMX - Maximum number of iterations allowed in the location of bifurcation points
24. ITNW - Maximum number of combined Newton-Chord iterations

25. NWTN - Number of iterations after which the Jacobian freezes and the remaining iterations correspond to the Chord method
26. JAC - Flag indicates whether the user supplies the derivatives or not
27. EPSL - Relative convergence criterion for parameters
28. EPSU - Relative convergence criterion for solution components
29. EPSS - Relative convergence criterion for the detection of special points
30. DS - Initial pseudo-arclength step size
31. DSMIN - Minimum allowable absolute value of the pseudo-arclength of the step size
32. DSMAX - Maximum allowable absolute value of the pseudo-arclength of the step size
33. IADS - Controls the frequency of step-size adaptation
34. NTHL - Number of continuation parameters whose influence in the calculation of the step-size is to be modified
35. ITHL - Vector containing the parameters corresponding to NTHL
36. NTHU - Number of state variables whose influence in the calculation of the step-size is to be modified
37. ITHU - Vector containing the states corresponding to NTHU
38. NUZR - Number of values of the principal continuation parameter at which output is desired in the file fort.8 (q.<name>)
39. IUZR - Vector containing the parameter values corresponding to NUZR
40. GCIDIFF - Number indicating the order to which the derivatives are supplied for the continuation process (Recommended value is 1)

41. GCNPSI - Number of test functions to be monitored during the continuation
42. GCIPSI - Vector containing the test functions corresponding to GCNPSI
43. GCNFIXED - Dummy constant
44. GCIFIXED - Dummy constant
45. GCNOSEG - Number of segments for a given periodic trajectory of a hybrid dynamical system
46. GCSEGTYP - Signature of the periodic trajectory defined by GCNOSEG number of segments
47. GCHNO - Vector of length GCNOSEG containing information about the number of event functions to be monitored for each segments. For example, GCHNO(1) is the number of event functions to be monitored for 1-st segment, GCHNO(2) is the number of event functions to be monitored for 2-nd segment and so on.
48. GCHGRZIND - Vector of length GCHNO(1)+GCHNO(2)+...+GCHNO(GCNOSEG) that contains the index-vector information for the event functions to be monitored. The first GCHNO(1) components of GCHGRZIND correspond to the 1-st segment, the next GCHNO(2) components correspond to the 2-nd segment and so on.

The user-specified file <name>.f contains the vector fields \mathbf{f}_I , the event functions h_I , and the state jump functions \mathbf{g}_I and their first and second derivatives w.r.t. state variables and parameters. In addition, user-specific test functions may be included for monitoring during continuation, for example, event functions described in GCHGRZIND with which grazing incidence should be detected.

The <name>.dat file contains the time evolution of the state variables for one complete time period of the periodic trajectory. This file is used when the starting solution for the

continuation is provided by the user. Example `gc.<name>`, `<name>.f` and `<name>.dat` files are shown in the appendix.

The `<fort>.7 (p.<name>)` output file contains the bifurcation diagram. Its format is the same as the output on the screen during a continuation. The `<fort>.8 (q.<name>)` output file contains graphical information of the periodic orbits printed at regular intervals that are dictated by the constant NPR. Also, data in this file is labeled so that it can be used to restart a new continuation without specifying another `<name>.dat` file.

The output file `<fort>.9 (d.<name>)` contains the information about the convergence and Floquet multipliers for a given continuation process. It also contains the index information when a segment of a periodic trajectory attains a grazing contact with an event surface. Using the constant of continuation IID, the reduced Jacobian for the boundary-value problem can be written to the `d.<name>` file.

The problem type “180” is used for single-parameter continuation of periodic trajectories of hybrid dynamical systems. The principal parameter along with the time periods (`PAR(61)`, `PAR(62)`, \dots) for each segment of the periodic trajectory are listed as the continuation parameters in the `gc.<name>` file. This file also contains the signature of the periodic trajectory. The constant ISW is set to “1”.

In certain cases of single-parameter continuation of periodic trajectories of hybrid dynamical systems, the information in the `q.<name>` file from a previous continuation cannot be used directly as the starting solution. Specifically, if the new continuation of a periodic trajectory consists of an extra segment than the previous continuation whose `q.<name>` file is used to obtain the initial solution, then a modification is required to the labeled data. Here, the data corresponding to the label from which the continuation is desired is extracted manually and modified according to the signature of the periodic trajectory of the new continuation and supplied to the program in a `<name>.dat` file.

During a single-parameter continuation, the periodic trajectory might undergo stability changes due to saddle-node and period-doubling bifurcations. Stability changes in the

trajectory can also occur due to grazing bifurcation, i.e., when one of its segments attains a grazing contact with an event surface corresponding to the zero-level surface of an event function. A loci of these bifurcation points can be obtained via two-parameter continuations.

5.2.2 Two-parameter Continuation

As in the case of single-parameter continuation, all the three text files (gc.<name>,<name>.f,<name>.dat.) must also be provided in the case of two-parameter continuation (tasks 2 and 3). Here, two parameters are specified instead of one along with the time period for each segment as the continuation parameters. The value of the constant IRS is set to the label corresponding to the saddle-node, period-doubling or (in certain special cases) grazing bifurcation point.

Moreover, in the case of locating the loci of saddle-node and period-doubling bifurcations, the value of the constant ISW is set to “2”. The signature is set to be same as the one used for the corresponding single-parameter continuation from which the initial solution for the two-parameter continuation is extracted and the same problem type “180” is used.

In the case of locating a loci of grazing bifurcations in two-parameters, the procedure described in one of the previous sections of this chapter may need to be employed. Accordingly, the number of segments and the corresponding signature of the grazing periodic trajectory is changed and the value of the constant ISW is set to “1”. Also, the problem type is changed to “150”. During continuation, the test functions corresponding to this problem type in the subroutine PVLS detect the parameter set for which $\xi_n = 0$ where $n = 1, \dots, 5$ and print them in the output file d.<name> as “UZ” (refer to Chapter 2 for detailed description of the $\xi_n = 0$ co-dimension-two bifurcation points). As discussed previously these co-dimension-two bifurcation points are known to serve as organizing centers for a variety of co-dimension-one bifurcation curves such as saddle-node and period-doubling bifurcations.

5.3 Illustrations using $\widehat{\text{TC}}$

5.3.1 Linear Oscillator

To illustrate the methodology and functionality of $\widehat{\text{TC}}$ consider the vector field

$$\mathbf{f}_1(\mathbf{u}) = \begin{pmatrix} x^2 \\ \alpha y^2 - 2\zeta x^2 - x^1 \\ y^1 + \omega y^2 - y^1((y^1)^2 + (y^2)^2) \\ y^2 - \omega y^1 - y^2((y^1)^2 + (y^2)^2) \end{pmatrix}, \quad (5.56)$$

where

$$\mathbf{u} = \begin{pmatrix} \mathbf{x} \\ \mathbf{y} \end{pmatrix} \in \mathbb{R}^2 \times \mathbb{R}^2 \quad (5.57)$$

is the state vector; the event functions

$$h_1(\mathbf{u}) = 1 - x^1, \quad (5.58)$$

$$h_2(\mathbf{u}) = x^2; \quad (5.59)$$

and the state jump functions

$$g_1(\mathbf{u}) = \begin{pmatrix} x^1 \\ -rx^2 \\ y^1 \\ y^2 \end{pmatrix}, \quad (5.60)$$

$$g_2(\mathbf{u}) = \mathbf{u}. \quad (5.61)$$

Now let

$$\mathbb{Z}_f = \{1\}, \quad (5.62)$$

$$\mathbb{Z}_h = \{1, 2\}, \quad (5.63)$$

$$\mathbb{Z}_g = \{1, 2\}, \quad (5.64)$$

and suppose that \mathbb{F} is the subset of $\mathbb{Z}_f \times \mathbb{Z}_h \times \mathbb{Z}_g$ corresponding to the connectivity graph in Fig. 2.1 from which it follows that the dynamics of the hybrid system is captured by three distinct values of the index vector, namely

$$\mathbf{J}_1 = (\mathbf{f}_1, h_1, g_1), \quad (5.65)$$

$$\mathbf{J}_2 = (\mathbf{f}_1, h_2, g_2). \quad (5.66)$$

$$\mathbf{J}_3 = (\mathbf{f}_1, h_1, g_2). \quad (5.67)$$

In particular, a trajectory for which the signature consists only of $\{\mathbf{J}_2, \mathbf{J}_3\}$ is said to be *nonimpacting*, while a trajectory with segments for which \mathbf{J}_1 is said to be *impacting*.

For each value of the index vector, the dynamics in the \mathbf{y} component are uncoupled from those in the \mathbf{x} component. Indeed, the former contain a globally attractive periodic trajectory

$$\mathbf{y} = \begin{pmatrix} \sin \omega t \\ \cos \omega t \end{pmatrix}. \quad (5.68)$$

Thus, the dynamics in the \mathbf{x} component correspond to the solution to the nonautonomous vector field

$$\tilde{\mathbf{f}}(\mathbf{x}) = \begin{pmatrix} x^2 \\ \alpha \cos \omega t - 2\zeta x^2 - x^1 \end{pmatrix} \quad (5.69)$$

or, equivalently, to the periodically excited linear mass-spring-damper oscillator

$$\ddot{q} + 2\zeta\dot{q} + q = \alpha \cos \omega t, \quad (5.70)$$

where α is the excitation amplitude and ζ is the damping coefficient (see Thota *et al.* [45]).

Fig. 5.5 shows a nonimpacting periodic trajectory of the hybrid dynamical system for $r = 0.8$, $\omega = 2.0$, and $\alpha = 3.0$ with base unit signature $\{\mathbf{J}_2\}$. Fig. 5.6(left panel) shows the results of single-parameter continuation using this trajectory as a starting point and terminating at a point $\alpha = 1.998$ where the periodic trajectory achieves grazing incidence with the event surface $h_1 = 0$ at a point $\mathbf{u} = \begin{pmatrix} 1.0 & 0 & 0.6658 & -0.9977 \end{pmatrix}^T$. Fig. 5.6(right panel) shows the resultant *grazing curve* in the (α, ω) parameter space with base unit signature $\{\mathbf{J}_3\}$.

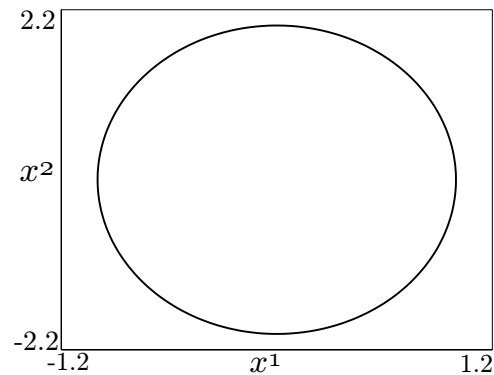


Figure 5.5: A nonimpacting periodic trajectory of the linear oscillator for $\omega = 2.0$ and $\alpha = 3.0$.

Single-parameter continuation for fixed ω and varying α away from the grazing curve requires replacing the periodic trajectory with the equivalent trajectory with base unit signature $\{\mathbf{J}_1\}$. The result of such continuation for two distinct values of ω are shown in Fig. 5.7 and Fig. 5.8. In each case, the right panel shows two selected impacting periodic trajectories corresponding to the grazing and period-doubling bifurcation points and the grazing and saddle-node bifurcation points, respectively.

Fig. 5.9 shows the results of continuation of the saddle-node and period-doubling bifurcation points in (α, ω) parameter space along with the grazing curve. The former curves terminate at a point ($\omega = 1.9975$ and $\alpha = 2.9966$) of quadratic contact with the grazing curve at a co-dimension-two grazing bifurcation point as discussed previously. *Note:* All the periodic trajectories corresponding to the hybrid dynamical system discussed for this example are one-segment trajectories.

In the case of a single-parameter continuation from a grazing periodic trajectory, the direction of continuation (sign of DS) decides the validity of the solution trajectory obtained. If the parameter DS is varied in a certain direction the solution converges to a periodic trajectory similar to the one shown in Fig. 5.10 which, while a valid solution to the associated BVP, is inconsistent with model assumptions and hence can be discarded.

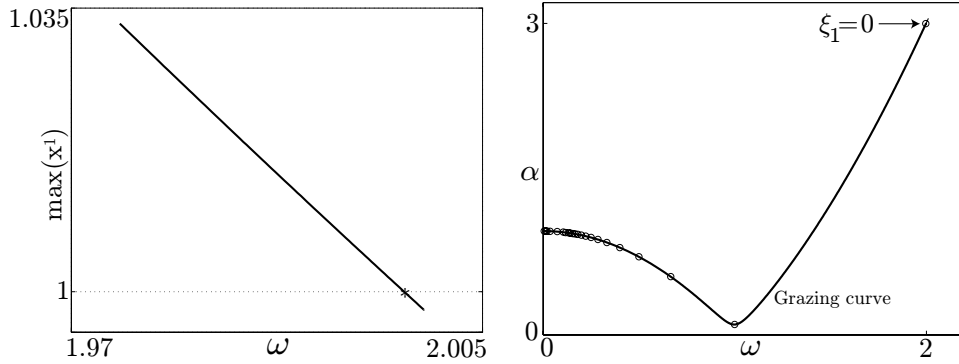


Figure 5.6: Left panel - Diagram indicating the continuation of a nonimpacting periodic trajectory corresponding to the vector field shown in the Eq. (5.56). Here, $\widehat{\text{TC}}$ detects the parameter value corresponding to a grazing incidence with the event surface $h_1 = 0$ that can be used as a starting solution to obtain a grazing curve. Right panel - Grazing curve in the $(\alpha - \omega)$ space obtained using $\widehat{\text{TC}}$. The o 's on the grazing curve correspond to the co-dimension-two bifurcation points $\xi_1 = 0$.

5.3.2 A Nonlinear MEMS Oscillator

Consider the reduced formulation of the nonlinear MEMS oscillator studied in Section 2.2 obtained by restricting attention to the closed subsystem obtained by eliminating the x^1 state variable and let $m_1 = 5$, $m_2 = 1$, $k = 1$, $c = 0.04$, $d = 1$, $e = 0.8$, $\mu_s = 0.4$, $\mu_d = 0.27$, and $\alpha = 1$ (see [7, 52, 54]).

Introduce the additional event function

$$h_{\text{Poincaré}}(\mathbf{x}) = x^4 \quad (5.71)$$

and additional value of the index vectors

$$\begin{aligned} \mathbf{J}_{11} &= (\text{stick}, \text{Poincaré}, \text{identity}) \\ \mathbf{J}_{12} &= (\text{stick}, \text{front}, \text{identity}). \end{aligned} \quad (5.72)$$

Then, Fig. 5.11 shows a nonimpacting periodic trajectory of the hybrid dynamical system for $r = 0.8$, $\omega = 0.8$, and $V = 0.5641$ with base unit signature $\{\mathbf{J}_{11}\}$. A single-parameter continuation using this trajectory as a starting point terminates for $V = 0.5979$ where

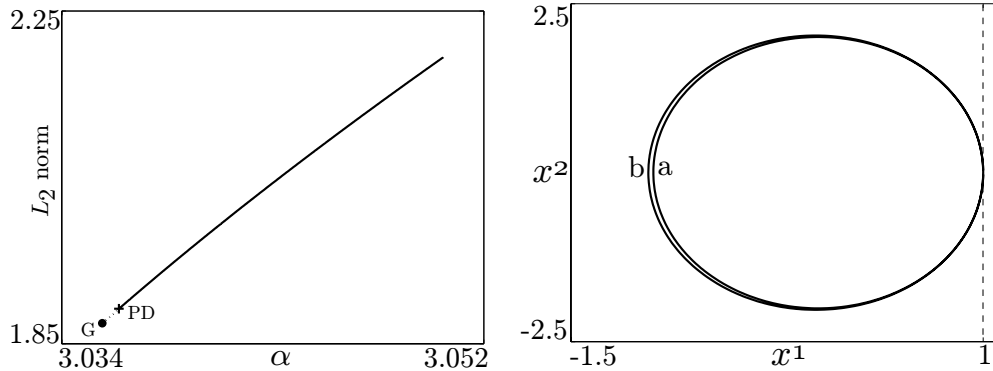


Figure 5.7: Left panel - Bifurcation diagram indicating the continuation of an impacting periodic orbit as a function of α with a grazing periodic orbit as a starting solution, for $\omega = 2.0072$ and $\alpha = 3.0357$. This impacting periodic trajectory experiences a period-doubling bifurcation at $\alpha = 3.0364$ resulting in a stable impacting trajectory. Right panel - Impacting periodic trajectories corresponding to the grazing incidence (a) and period-doubling bifurcation (b) points from the left panel.

the periodic trajectory achieves grazing incidence with the event surface $h_{\text{front}} = 0$ at a point $\mathbf{u} = \begin{pmatrix} 0 & 0.5 & 0 & 0 & 1 \end{pmatrix}^T$. Fig. 5.12 shows the resultant grazing curve in the (V, ω) parameter space using the signature $\{\mathbf{J}_{12}\}$.

Single-parameter continuation for fixed $\omega = 0.8$ and varying V away from the grazing curve requires replacing the grazing periodic trajectory with a two-segment periodic trajectory with base unit signature $\{\mathbf{J}_1, \mathbf{J}_7\}$. Specifically, the segment corresponding to \mathbf{J}_1 is the original grazing curve and the segment corresponding to \mathbf{J}_7 consists of a constant trajectory at the grazing point. The result of such continuation is shown in Fig. 5.13. Here, the branch of periodic trajectories terminates for $V = 0.7469$ where the two-segment periodic trajectory achieves grazing incidence with the event surface $h_{\text{front}} = 0$ at a point $\mathbf{u} = \begin{pmatrix} 0 & 0.5 & -0.00057 & -0.2535 & 0.9673 \end{pmatrix}^T$. The right panel shows selected impacting periodic trajectories corresponding to the period-doubling and grazing bifurcation points.

Fig. 5.14 shows the results of continuation of the saddle-node and period-doubling bifurcation points in (V, ω) parameter space along with the grazing curve through $(0.5979, 0.8)$.

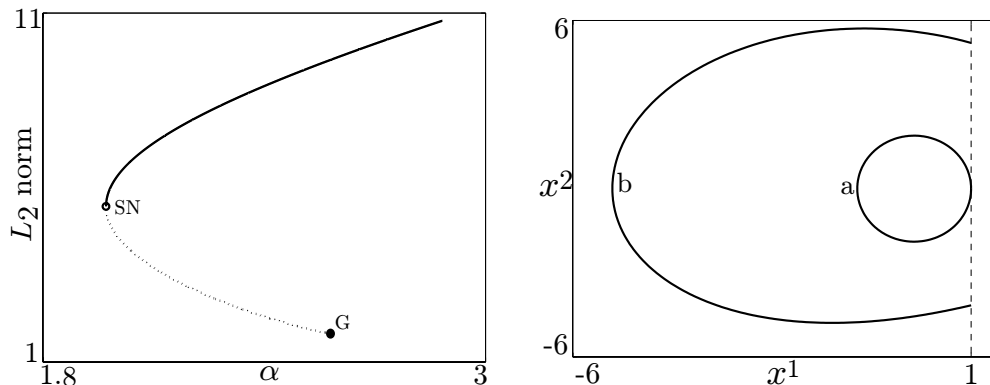


Figure 5.8: Left panel - Bifurcation diagram indicating the continuation of an impacting periodic trajectory as a function of α with a grazing periodic trajectory as a starting solution, for $\omega = 1.8901$ and $\alpha = 2.5797$. This impacting periodic trajectory experiences a saddle-node bifurcation at $\alpha = 1.9713$ resulting in a stable impacting trajectory. Right panel - Impacting periodic trajectories corresponding to the grazing incidence (a) and saddle-node bifurcation points (b) from the left panel.

These curves terminate at a point of quadratic contact with the grazing curve at a co-dimension-two grazing bifurcation point as discussed previously.

Two-parameter continuation of the grazing curve through the $(0.7469, 0.8)$ point in parameter space requires replacing the two-segment grazing periodic trajectory with a three-segment periodic trajectory with base unit signature $\{\mathbf{J}_{12}, \mathbf{J}_1, \mathbf{J}_7\}$ (cf. Fig. 5.15). Specifically, the concatenation of the segments corresponding to \mathbf{J}_{12} and \mathbf{J}_1 is identical (except for the reparametrization) of the \mathbf{J}_1 segment of the grazing trajectory. The result of such continuation is shown in Fig. 5.16.

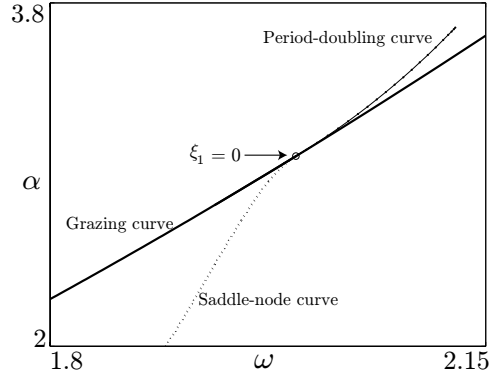


Figure 5.9: Left panel - Diagram depicting the two parameter continuation of grazing trajectories, saddle-node bifurcation points and period-doubling points correspond to impacting periodic trajectories. As mentioned previously, the saddle-node and period-doubling curves intersect the grazing curve tangentially at the co-dimension-two bifurcation point corresponding to $\xi_1 = 0$.

5.3.3 Periodic Orbit in a Three-dimensional State Space

Consider the dynamical system governed by the vector field ([38] and [31])

$$\mathbf{f}_1(\mathbf{x}) = \begin{pmatrix} mx^1 - x^2 - x^1 x^3 \\ mx^2 + x^1 \\ -x^3 + (x^2)^2 + (x^1)^2 x^3 \end{pmatrix}, \quad (5.73)$$

the event function $h_1(\mathbf{x}) = x^1 - \mu$, and the state jump function

$$\mathbf{g}_1(\mathbf{x}) = \begin{pmatrix} x^1 \\ (m - x^3)x^1 - r(x^2 - x^1(m - x^3)) \\ x^3 \end{pmatrix}, \quad (5.74)$$

and restrict attention to trajectory segments with signature

$$\mathbf{J}_1 = (\mathbf{f}_1, h_1, \mathbf{g}_1). \quad (5.75)$$

Single-parameter continuation of a single-segment periodic trajectory for $m = 0.28$ and with base unit signature $\{\mathbf{J}_1\}$ emanating from a grazing periodic trajectory at $\mu \approx -0.7981$

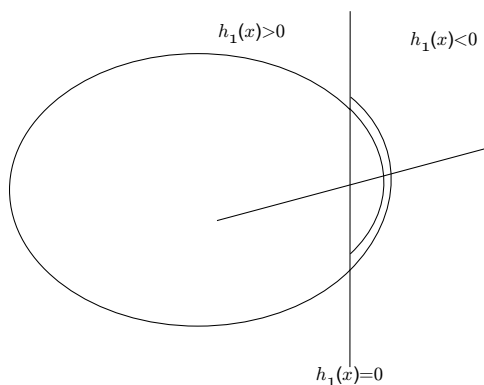


Figure 5.10: Valid solution to the boundary value problem with no physical significance.

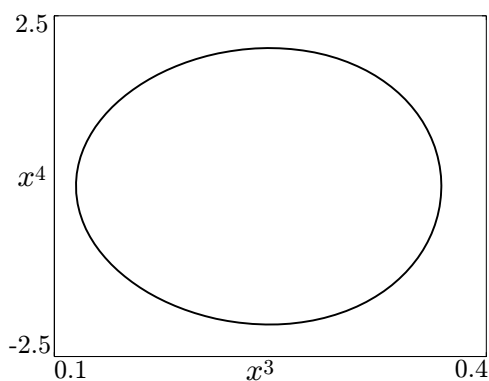


Figure 5.11: A nonimpacting periodic trajectory of the nonlinear mems oscillator for $\omega = 0.8$, and $V = 0.5641$.

is shown in the left panel of Fig. 5.17. Similarly, single-parameter continuation of a single-segment periodic trajectory for $m = 0.39$ and with base unit signature $\{\mathbf{J}_1\}$ emanating from a grazing periodic trajectory at $\mu \approx -0.8271$ is shown in the right panel of Fig. 5.17 (cf. Chapter 4)

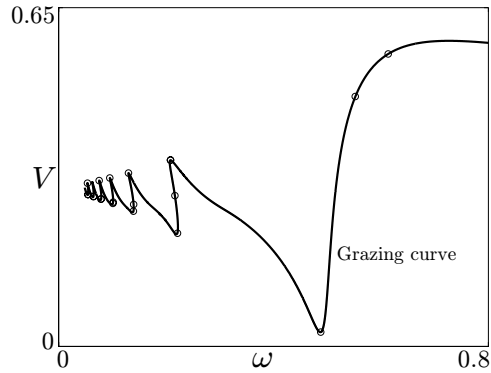


Figure 5.12: Grazing curve in the $(V - \omega)$ space obtained using $\widehat{\text{TC}}$ for the given nonlinear MEMS oscillator. The o 's on the grazing curve correspond to the co-dimension-two bifurcation points $\xi_n = 0$.

5.3.4 Periodic Orbit in a Four-dimensional State Space

Consider the dynamical system governed by the vector field (A forced version of the example discussed above)

$$\mathbf{f}_1(\mathbf{u}) = \begin{pmatrix} mx^1 - x^2 - x^1x^3 \\ mx^2 + x^1 + Ay^2 \\ -x^3 + (x^2)^2 + (x^1)^2x^3 \\ y^1 + \omega y^2 - y^1((y^1)^2 + (y^2)^2) \\ y^2 - \omega y^1 - y^2((y^1)^2 + (y^2)^2) \end{pmatrix}, \quad (5.76)$$

where $\mathbf{u} = \begin{pmatrix} \mathbf{x} \\ \mathbf{y} \end{pmatrix}$, the event function $h_1(\mathbf{u}) = x^1 - \mu$ and the state jump function

$$\mathbf{g}_1(\mathbf{u}) = \begin{pmatrix} x^1 \\ (m - x^3)x^1 - r(x^2 - x^1(m - x^3)) \\ x^3 \\ y^1 \\ y^2 \end{pmatrix} \quad (5.77)$$

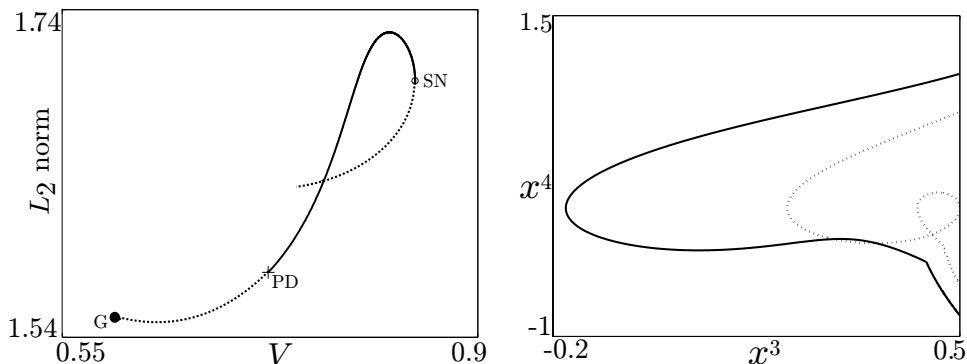


Figure 5.13: Left panel shows the bifurcation diagram corresponding to a one parameter continuation of a two-segment periodic trajectory for $\omega = 0.8$. The locus of saddle-node, period-doubling and secondary grazing bifurcations is also shown in the figure. Here, segment-1 of the two-segment periodic orbit undergoes a secondary grazing incidence with the event surface $h_{\text{front}} = 0$. A few examples of the two-segment periodic trajectories are depicted in the right panel. The dotted trajectory in the right panel indicates the periodic trajectory undergoing a secondary grazing incidence.

and restrict attention to trajectory segments with signature

$$\mathbf{J}_1 = (\mathbf{f}_1, h_1, \mathbf{g}_1). \quad (5.78)$$

Single-parameter continuation of a single-segment periodic trajectory for $A = 1.25$, $\omega = 1.9$, and $r = 0.8$ and with base unit signature $\{\mathbf{J}_1\}$ emanating from a grazing periodic trajectory at $\mu \approx -0.4940$ is shown in the left panel of Fig. 5.18. Here, the right panel shows selected trajectories corresponding to particular points along the branch of periodic trajectories.

5.4 Summary

This chapter presents the basic structure of the software program, $\widehat{\text{TC}}$, for use in the bifurcation analysis of hybrid dynamical systems. Mathematical tools including pseudo-arclength

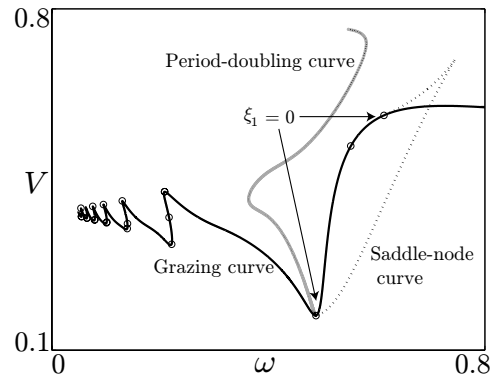


Figure 5.14: This figure presents the two parameter continuation of grazing, saddle-node and period-doubling bifurcation points corresponding to an impacting periodic trajectory. As mentioned previously, the intersection of the grazing curve and the saddle-node and period-doubling curves occur at co-dimension-two bifurcation points corresponding to $\xi_1 = 0$.

continuation and orthogonal collocation methods using piecewise polynomials required in the continuation process are discussed in detail. The chapter also formulates boundary value problems corresponding to the construction and continuation of grazing, saddle-node, and period-doubling bifurcations of periodic trajectories in hybrid dynamical systems. It also presents the methodology required to compute the correct eigenvalues of periodic orbits in hybrid dynamical systems.

The functions of $\widehat{\text{TC}}$ and the problem types involved in its application are discussed using four example hybrid dynamical systems in two or several dimensions. A variety of bifurcation diagrams involving saddle-node, period-doubling, and grazing bifurcations corresponding to these examples are reported. These examples serve to explain the resegmentation process required to restart single- and two-parameter continuation from a grazing periodic trajectory.

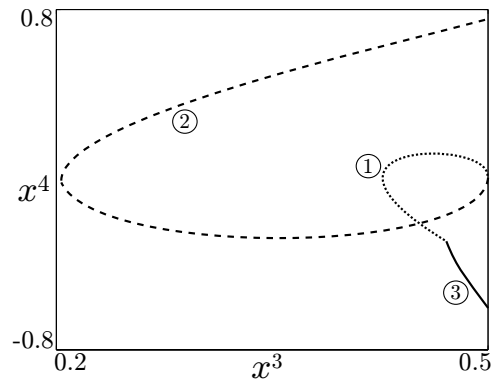


Figure 5.15: Illustration of a procedure to create a starting solution for the continuation of a grazing trajectory of a hybrid dynamical system through $(0.7469, 0.8)$. The trajectory shown here is same as the dotted trajectory in Fig. 5.13.

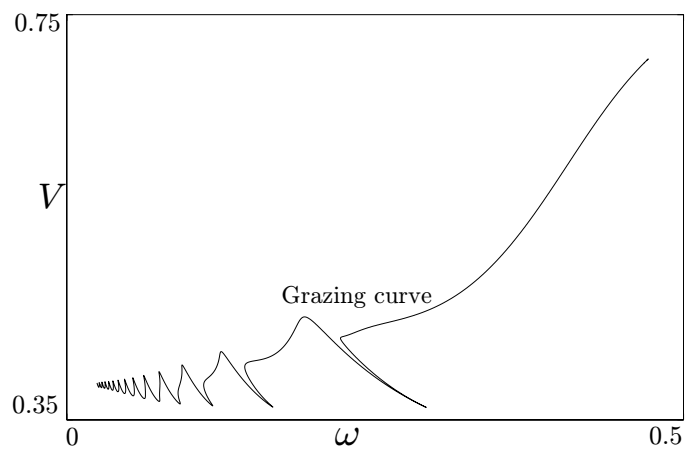


Figure 5.16: The grazing curve corresponding to the MEMS oscillator obtained through the grazing point $(0.7469, 0.8)$.

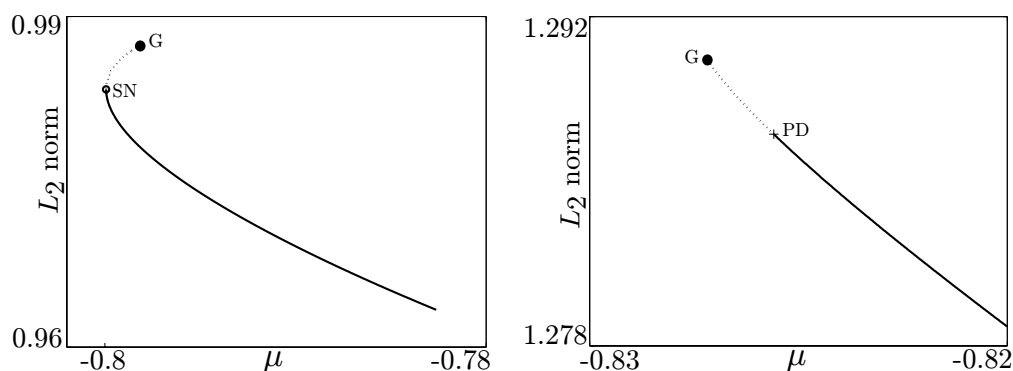


Figure 5.17: Left panel presents the bifurcation diagram corresponding to $m = 0.28$ where $\mu_* \approx -0.7981$. Here, an unstable impacting orbit is born in the immediate vicinity of the grazing periodic trajectory that undergoes a saddle-node bifurcation. On the contrary, the right panel shows a bifurcation diagram corresponding to $m = 0.39$ where an unstable orbit is born for μ greater than μ_* . This unstable orbit undergoes a period-doubling bifurcation to give rise to a stable impacting orbit.

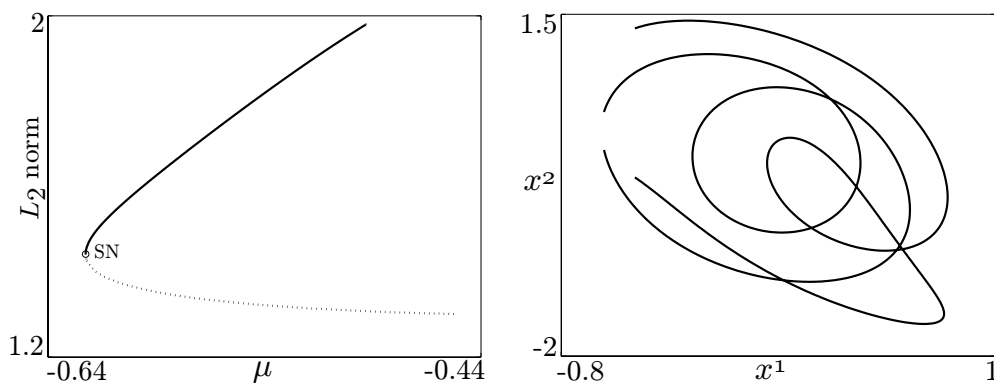


Figure 5.18: Left panel shows the bifurcation diagram corresponding to $A = 1.25$, $\omega = 1.9$, and $\mu_* \approx -0.4940$. Here, a stable period-2 impacting orbit with one impact per period is continued as a function of the parameter μ along with the locus of the saddle-node bifurcation. Right panel shows the impacting periodic trajectories corresponding to two points of the bifurcation diagram on the left.

Chapter 6

Conclusions and Future Recommendations

This dissertation has documented efforts to apply the discontinuity-mapping approach to the bifurcation analysis of grazing quasiperiodic trajectories in hybrid dynamical systems and the development of a computational toolbox for the bifurcation analysis of periodic trajectories in hybrid dynamical systems. The former constitutes the first rigorous formulation of the discontinuity-mapping approach in this context and extends previously obtained heuristic results on the grazing bifurcations of invariant tori. It also establishes the essential characteristics underlying the distinction between continuous and discontinuous grazing bifurcations of periodic and quasiperiodic trajectories in such systems with emphasis on the dimensionality of the associated invariant tori. The computational toolbox vastly extends the ability of existing numerical tools so as to enable comprehensive bifurcation analysis of a broad range of hybrid dynamical systems originating in the physical, biological, and social sciences.

In the case of the application of the discontinuity-mapping approach to grazing bifurcations of quasiperiodic trajectories on invariant tori, it was found that the dominant term of the discontinuity mapping was proportional to the square root of the projection of the

deviation from a point of grazing contact onto a normal vector perpendicular to the corresponding event surface. In the case of co-dimension-one invariant tori, the application of the smooth Poincaré map to this term results in a contribution that either vanishes entirely (as in the case of periodic trajectories in a two-dimensional state space) or is tangential to the grazing invariant torus. In the former case, the analysis of grazing bifurcations falls into the category of border-collision bifurcations and is governed by the piecewise linear nature of the composite Poincaré map. In the latter case, however, it was argued that a local attractor would persist near the original invariant torus for some finite deviation in parameters away from the grazing bifurcation parameter values. In contrast to the periodic case, it was suggested that the quasiperiodicity guarantees that the stabilizing behavior of the smooth dynamics in the limit of small deviations in parameter space dominates any destabilizing effects of the impacts contained in higher-order terms of the discontinuity mapping.

In contrast, in co-dimension-two quasiperiodic system attractors, the analysis suggests and demonstrates numerically that discontinuous jumps may still occur for small but nonvanishing deviations of the system parameter away from the value corresponding to the grazing contact. In this case, the number of iterates between passages near \mathbf{x}_* is bounded from above and the bifurcation behavior is expected to more closely mimic that of a periodic trajectory. Hence, it can be concluded that even though strictly discontinuous grazing bifurcations are impossible in co-dimension-one quasiperiodic system attractors, *seemingly* discontinuous grazing bifurcations can occur in their co-dimension-two (or higher) counterparts for small deviations away from the parameter corresponding to grazing contact.

6.1 Future Recommendations

1. It would be interesting to seek conditions similar to the $\xi_n < 0$ criterion (in the periodic case) to determine the loss of a local attractor resulting in apparently (if not strictly) discontinuous grazing bifurcations of co-dimension-two or higher quasiperiodic

attractors.

2. As an alternative approach to formulate such criterion more numerical examples can be studied using the discontinuity-mapping approach.
3. Experiments can be conducted to better understand and verify previously obtained results in grazing bifurcations of originally quasiperiodic system attractors. Also, meticulous experimentation can provide insights into the conditions that lead to the disappearance of the local attractor in certain cases.
4. It would be interesting to evaluate the extent to which qualitative predictions based on the formulation of a reduced map carry over to general systems. For example, the typical bifurcation sequence from torus-covering chaotic, via periodic, to local chaotic attractors.
5. The conclusion that discontinuous grazing bifurcations are strictly impossible in the quasiperiodic case can be viewed as a basis for a control strategy to eliminate discontinuous grazing bifurcations in the periodic case. This would require introducing quasiperiodic forcing into the system or forcing the system with a frequency that is incommensurate with the existing one. This concept can be explored both numerically and experimentally.
6. Although $\widehat{\text{TC}}$ was developed as an add-on to a modified version of AUTO 97, it appears reasonable to envision that $\widehat{\text{TC}}$ eventually become fully integrated into AUTO 97. This is particularly true given the fact that smooth dynamical systems may be formulated as special cases of hybrid dynamical systems.
7. It would be natural to pursue further automation of the resegmentation process required when restarting $\widehat{\text{TC}}$ from a grazing periodic trajectory.

Bibliography

- [1] P. V. Bayly and L. N. Virgin, “An Experimental Study of an Impacting Pendulum ”, *Journal of Sound and Vibration*, 164(2)(1993), pp. 364–374.
- [2] R. Bishop, “Impact Oscillators ”, *Philosophical Transactions: Physical Sciences and Engineering*, 347(1683)(1994), pp. 347–351.
- [3] C. Budd, and F. Dux, “Intermittency in Impact Oscillators Close to Resonance”, *Non-linearity*, 7(1994), pp. 1191–1224.
- [4] C. Budd, and F. Dux, “The Effect of Frequency and Clearance Variations on Single-Degree-of-Freedom Impact Oscillators ”, *Journal of Sound and Vibration*, 184(3)(1995), pp. 475–502.
- [5] W. Chin, E. Ott, H. E. Nusse, and C. Grebogi, “Grazing bifurcations in impact oscillators”, *Physical Review E*, 50(1994), pp. 4427–4444.
- [6] H. Dankowicz and A. B. Nordmark, “On the origin and bifurcations of stick-slip oscillations”, *Physica D*, 136(1999), pp. 280–302.
- [7] H. Dankowicz, X. Zhao, “Local analysis of codimension-one and codimension-two grazing bifurcations in impact microactuators ”, *Physica D* 202(2005) 238-257.
- [8] H. Dankowicz, J. Jerrelind, “Control of near-grazing dynamics in impact oscillators ”, *Proceedings of the Royal Society of London, series A*, 461(2063)(2005) 3365-3380.

- [9] H. Dankowicz, P. Piiroinen, A.B. Nordmark, “Low-velocity Impacts of Quasiperiodic Oscillations ”, *Chaos Solitons Fractals* 14(2002) 241–255.
- [10] H. Dankowicz, P. Piiroinen, A.B. Nordmark, “Grazing Bifurcations of Initially Quasi-Periodic System Attractors ”, *Proceedings of 18th Biennial Conference on Mechanical Vibration and Noise* (2001), Pittsburgh, USA.
- [11] F. Dercole and Y. A. Kuznetsov, “SLIDECONT: An AUTO 97 Driver for Bifurcation Analysis of Filippov Systems, *ACM Transactions on Mathematical Software* ”, 31(1)(2005), pp. 95 – 119.
- [12] D. F. Davidenko, “On a new method of numerical solution of systems of nonlinear equations ”, *Dokl. Akad. Nauk. SSSR* 88(1953); *Math. Rev.* 14,906.428.
- [13] E. J. Doedel, “AUTO: A program for the automatic bifurcation analysis of autonomous systems ”, *Cong. Num.* 30, 1981, 265-284, (Proc. 10th Manitoba Conf. on Num. Math. and Comp., Univ. of Manitoba, Winnipeg, Canada.)
- [14] E. J. Doedel, H. B. Keller, and J. P. Kernevez, “Numerical Analysis and Control of Bifurcation Problems (II) Bifurcation in Infinite Dimensions ”, *International Journal of Bifurcation and Chaos*, 1(4)(1991), pp. 745 – 772.
- [15] F. Ehrich, “Some observations of chaotic vibration phenomenon in high-speed rotor dynamics”, *Journal of Vibration and Acoustics - Transactions of ASME*, 113 (1)(1991) 50–57.
- [16] M. J. Feigenbaum, “Quantitative Universality for a class of Nonlinear Transformations ”, *Journal of statistical Physica* 19(1978) 25–52.
- [17] S. Foale, “Analytical Determination of Bifurcations in an Impact Oscillator”, *Proceedings of the Royal Society of London, series A*, 347(1994), pp. 373–364.

- [18] S. Foale, and R. Bishop, “Dynamical Complexities of Forced Impacting Systems”, *Philosophical Transactions: Physical Sciences and Engineering*, 328(1651)(1992), pp. 547–556.
- [19] S. Foale, and R. Bishop, “Bifurcations in impacting systems”, *Nonlinear Dynamics*, 6(1994), pp. 285–299.
- [20] M. H. Fredriksson, and A. B. Nordmark, “Bifurcations caused by grazing incidence in many degrees of freedom impact oscillators”, *Proceedings of the Royal Society of London, series A*, 453(1997), pp. 1261–1276.
- [21] M. Golubitsky, and D. G. Schaeffer, “Singularities and Groups in Bifurcation Theory”, Springer-Verlag(1985), New York.
- [22] J. Guckenheimer, and P. Holmes, “Nonlinear Oscillations, Dynamical Systems and Bifurcations of Vector Fields ”, Springer-Verlag (1983), New York.
- [23] M.A. Hassouneh, E.H. Abed and H.E. Nusse, “Robust dangerous border-collision bifurcations in piecewise smooth systems, *Physical Review Letters*, 92(7)(2004).
- [24] H. B. Keller, “Numerical Solutions of Bifurcation and Nonlinear Eigenvalue Problems, in *Applications of Bifurcation Theory (1977)* ”, P. H. Rabinowitz, Ed., Academic Press, New York.
- [25] H. B. Keller, “Lectures on Numerical Methods in Bifurcation Problems ”, Springer-Verlag (1987), New York.
- [26] M. Kubicek and M. Marek, “Computational Methods in Bifurcation Theory and Dissipative Structures ”, Springer-Verlag (1983),New York.
- [27] R.I. Leine, D.H. Van Campen, B.L. Van de Vrande, “Bifurcations in nonsmooth systems”, *Nonlinear Dynamics*, 23(2000) 105–164.

- [28] M. Mita, M. Arai, S. Tensaka, D. Kobayashi, and H. Fujita, “A micromachined impact microactuator driven by electrostatic force”, *IEEE Journal of Microelectromechanical Systems*, 12(1)(2003) 37–41.
- [29] D. B. Moore and S.W. Shaw, “The Experimental Response of an Impacting Pendulum System ”, *International Journal of Nonlinear Mechanics*, 25(1)(1990) 1–16.
- [30] P.C. Müller, “Calculation of Lyapunov Exponents for Dynamics Systems with Discontinuities ”, *Chaos Solitons Fractals* 5(9) (1995), pp. 1671–1681.
- [31] A.H. Nayfeh, B. Balachandran, “Motion Near a Hopf Bifurcation Of A Three-Dimensional System ”, *Mech. Res. Comm* 17(4)(1990) 191-198.
- [32] A. H. Nayfeh, B. Balachandran, “Applied Nonlinear Dynamics: Analytical, Computational and Experimental Methods ”, *Wiley Series in Nonlinear Science* (1995), New York.
- [33] A.B. Nordmark, “Universal limit mapping in grazing bifurcations”, *Physical Review, E* 55(1)(1997) 266–270.
- [34] A.B. Nordmark, “Effects due to low velocity impact in mechanical oscillators”, *International Journal of Bifurcation and Chaos: Applied Sciences and Engineering*, 2(3)(1992), 597–605.
- [35] A. B. Nordmark, “Non-periodic motion caused by grazing incidence in an impact oscillator”, *Journal of Sound and Vibration*, **145**(1991), pp. 279–297.
- [36] H. E. Nusse, E. Ott, and J. A. Yorke, “Border-collision Bifurcations: An Explanation for Observed Bifurcation Phenomena ”, *Physical Review E*, 49(2)(1994), pp. 1073–1076.
- [37] T. S. Parker, L. O. Chua, “Practical Numerical Algorithms for Chaotic Systems ”, *Springer-Verlag* (1989), New York.

- [38] R.H. Rand, “Analytical Approximation For Period-Doubling Following A Hopf Bifurcation ”, *Mech. Res. Comm* 16(2)(1989), pp. 117 – 123.
- [39] S.W. Shaw and P.J. Holmes, “A periodically forced piecewise linear oscillator”, *Journal of Sound and Vibration* 90(1)(1983) pp. 129–155.
- [40] S.W. Shaw, “Forced Vibrations of a Beam with One-Sided Amplitude Constraint: Theory and Experiments ”, *Journal of Sound and Vibration*, 99(2)(1985) 199–212.
- [41] S. H. Strogatz, “Nonlinear Dynamics and Chaos: with Applications to Physica, Biology, Chemistry and Engineering ”, Addison-Wesley Publishing Company: (1994), Reading, MA.
- [42] J. M. T. Thompson and R. Ghaffari, “Chaotic Dynamics of an Impact Oscillator”, *Physical Review A*, 27(3)(1983) pp. 1741–1743.
- [43] J. M. T. Thompson, “Complex Dynamics of Complaint Off-shore Structures”, *Proceedings of the Royal Society of London- series A, Mathematical and Physical Sciences*, 387(1973)(1983) pp. 407–427.
- [44] P. Thota, H. Dankowicz, “Analysis of grazing bifurcations of quasiperiodic system attractors ”, *Physica D*, 220(2)(2006), pp. 163 – 174.
- [45] P. Thota, X. Zhao and H. Dankowicz, “Codimension-two grazing bifurcation points in Single-Degree-of-Freedom impact Oscillators ”, *Journal of Computational Nonlinear Dynamics*, 1(2006), pp. 328–335.
- [46] P. Thota, H. Dankowicz, “Continuous and discontinuous grazing bifurcations in impacting oscillators ”, *Physica D* 214(2006) 187–197.
- [47] M. D. Todd and L. N. Virgin, “An Experimental Impact Oscillator”, *Chaos, Solitons and Fractals*, 8(4)(1997), pp. 699–714.

- [48] G. S. Whiston, “Singularities in Vibro-Impact Dynamics ”, *Journal of Sound and Vibration*, 152(3)(1992), pp. 427–460.
- [49] J. Xie, W. Ding, “Hopf-Hopf bifurcation and invariant torus \mathbf{T}^2 of a vibro-impact system ”, *International Journal of Nonlinear Mechanics*, 40(2005), pp. 531 – 543.
- [50] G. Yuan, S. Banerjee, E. Ott and J.A. Yorke, “Border-collision bifurcations in the buck converter ”, *IEEE Transactions of Circuits and Systems, I* 45(7)(1998) 707–716.
- [51] E. C. Zeeman, “Catastrophe Theory: Selected Papers 1972-1977 ”, Addison-Wesley: Reading(1977), MA.
- [52] X. Zhao, H. Dankowicz, C.K. Reddy, A.H. Nayfeh, “Modeling and Simulation Methodology for Impact microactuators ”, *J. Micromech. Microeng.*, 14(2004) 775–784.
- [53] X. Zhao, H. Dankowicz, “Unfolding degenerate grazing dynamics in impact actuators ”, *Nonlinearity* 19(2)(2006) 399-418.
- [54] X. Zhao, C. K. Reddy and A. H. Nayfeh, “Nonlinear dynamics of an electrically driven impact microactuator”, *Nonlinear Dynamics*, 40(2005), pp. 227–239.

Appendix A

$\widehat{\text{TC}}$ Makefile

```
#-----  
#-----  
#                               Makefile  
#-----  
#-----  
#  
#   TC-HAT  
#  
#   An AUTO97 driver for grazing bifurcation analysis  
#  
#   BY   Phanikrishna Thota & Harry Dankowicz  
#  
#  
#   VERSION 1.0 (last revision 12/2006)  
#  
#-----  
#  
#   *****  
#   *                                           *  
#   *   Periodically forced MEMS oscillator   *  
#   *                                           *  
#   *****  
#  
#-----  
#  
PGM      = mems  
RM       = rm -f  
#  
all: superclean run  
#
```

run: 1 2 3 4

```

#
1:
@echo "1: Grazing curve "
@cp gc.$(PGM).1 gc.$(PGM)
@cp $(PGM).f.1 $(PGM).f
@cp $(PGM).dat.1 $(PGM).dat
@"@gmdat" $(PGM)
@cp q.$(PGM) q.dat.1
@"@gc" $(PGM)
@"@sv" $(PGM).1
@rm fort.* gc.$(PGM) q.$(PGM) $(PGM).f $(PGM).dat
#
2:
@echo "2: Continuation of a hybrid two-segment periodic trajectory from grazing"
@cp gc.$(PGM).2 gc.$(PGM)
@cp $(PGM).f.2 $(PGM).f
@cp $(PGM).dat.2 $(PGM).dat
@"@gmdat" $(PGM)
@cp q.$(PGM) q.dat.2
@"@gc" $(PGM)
@"@sv" $(PGM).2
@rm fort.* gc.$(PGM) q.$(PGM) $(PGM).f $(PGM).dat
#
3:
@echo " "
@echo "3: Starting data for COD-2 continuation of saddle-nodes of a periodic trajectory"
@cp gc.$(PGM).3 gc.$(PGM)
@cp $(PGM).f.3 $(PGM).f
@cp q.$(PGM).2 q.$(PGM)
@"@gc" $(PGM)
@"@sv" $(PGM).3
@rm fort.* gc.$(PGM) q.$(PGM) $(PGM).f
#
4:
@echo " "
@echo "4:Continuation of folds"
@cp gc.$(PGM).4 gc.$(PGM)
@cp $(PGM).f.3 $(PGM).f
@cp q.$(PGM).3 q.$(PGM)
@"@gc" $(PGM)
@"@sv" $(PGM).4
@rm fort.* gc.$(PGM) q.$(PGM) $(PGM).f
#

```

```
clean:
@echo "Cleaning $(PGM)..."
@$(RM) gc.$(PGM) q.$(PGM) $(PGM).f fort.* *.exe *.o *~ core
@echo "Cleaning ... done"
#
superclean:
@echo "Cleaning $(PGM)..."
@$(RM) gc.$(PGM) $(PGM).f $(PGM).dat
@$(RM) r.* p.* q.* d.* fort.* *.exe *.o *~ core
@echo "Cleaning ... done"
```

Appendix B

$\widehat{\text{TC}}$ Constants File gc.<name>

5 180 1 1	NDIM, IPS, IRS, ILP
3 1 61 62	NICP, (ICP(I), I=1, NICP)
50 2 3 2 1 0 0 0	NTST, NCOL, IAD, ISP, ISW, IPLT, NBC, NINT
1000 0.0 1.0 0.0 100.0	NMX, RLO, RL1, A0, A1
1 0 2 10 8 3 0	NPR, MXBF, IID, ITMX, ITNW, NWTN, JAC
1.e-10 1.e-10 1.e-10	EPSL, EPSU, EPSS
0.0001 0.0 0.005 1	DS, DSMIN, DSMAX, IADS
2	NTHL, ((ITHL(I), THL(I)), I=1, NTHL)
61 0.0	
62 0.0	
0	NTHU, ((ITHU(I), THU(I)), I=1, NTHU)
0	NUZR, ((IUZR(I), UZR(I)), I=1, NUZR)
0 1	GCISTART, GCIDIFF
3 1 2 3	GCNPSI, (GCIPSI(I), I=1, GCNPSI)
0	GCNFIXED, (GCIFIXED(I), I=1, GCNFIXED)
2 1 0	GCNOSEG, (GCSEGTY(I), I=1, GCNOSEG)
1 2	(GCFIND(I), I=1, GCNOSEG)
1 2	(GCHIND(I), I=1, GCNOSEG)
1 2	(GCGIND(I), I=1, GCNOSEG)
1 1	GCHNO(1), (GCHGRZIND(I), I=1, GCHNO(1))
2 2 1	GCHNO(2), (GCHGRZIND(I+GCHNO(1)), I=1, GCHNO(2))

Appendix C

$\widehat{\text{TC}}$ Functions File <name>.f

```
C-----  
C-----  
C                               mems.f  
C-----  
C-----  
C  
C   TC-HAT  
C  
C   An AUTO97 driver for grazing bifurcation analysis  
C  
C   BY Phanikrishna Thota & Harry Dankowicz  
C  
C  
C   VERSION 1.0 (last revision 8/2006)  
C  
C-----  
C  
C   *****  
C   *                                     *  
C   * Periodically forced MEMS oscillator *  
C   *                                     *  
C   *****  
C  
C-----  
C  
C   -----  
C   SUBROUTINE GCFUNC(GCNDIM,X,PAR,GCIDIFF,FI,  
C   + DFIDX,DFIDP,DFIDXDX,DFIDXDP,SEGNO)  
C   -----  
C
```

```

IMPLICIT DOUBLE PRECISION (A-H,O-Z)
c
INCLUDE 'mems.h'
c
INTEGER GCNDIM,GCIDIFF,PHANI,SEGNO
c
DIMENSION X(GCNDIM),PAR(*),FI(GCNDIM)
DIMENSION DFIDX(GCNDIM,GCNDIM),DFIDP(GCNDIM,*)
DIMENSION DFIDXDX(GCNDIM,GCNDIM,GCNDIM)
DIMENSION DFIDXDP(GCNDIM,GCNDIM,*)
c
-----
c
Vector field selection
c
-----
IF (SEGNO.EQ.1) THEN
c
-----
c
Vector field 1
c
-----
c
Right-hand side
c
-----
c
FI(1)=0.0D0
FI(2)=X(3)
FI(3)=-X(2)-0.04D0*X(3)
+  +0.5D0*(1-X(5))*(PAR(1)/(1.0D0-X(2)))**2
FI(4)=X(4) + 2*PAR(2)*X(5) - X(4)*(X(4)**2+X(5)**2)
FI(5)=X(5) - 2*PAR(2)*X(4) - X(5)*(X(4)**2+X(5)**2)
c
First derivatives
c
-----
IF (GCIDIFF.GE.1) THEN
c
with respect to state
DFIDX(2,3)=1.0D0
DFIDX(3,2)=-1.0D0 + (1-X(5))*(PAR(1)**2)/(1.0D0-X(2))**3
DFIDX(3,3)=-0.04D0
DFIDX(3,5)=-0.5D0*(PAR(1)**2)/(1.0D0-X(2))**2
DFIDX(4,4)=1.0D0 - 3.0D0*X(4)**2 - X(5)**2
DFIDX(4,5)=2.0D0*(PAR(2) - X(4)*X(5))
DFIDX(5,4)=-2.0D0*(PAR(2) + X(4)*X(5))
DFIDX(5,5)=1.0D0 - 3.0D0*X(5)**2 - X(4)**2
c
with respect to parameters

```

```

      DFIDP(3,1)=PAR(1)*(1-X(5))*(1/(1.0D0-X(2)))**2
      DFIDP(4,2)=2.0D0*X(5)
      DFIDP(5,2)=-2.0D0*X(4)
c
      END IF
c
c      Second derivatives
c      -----
c      IF (GCIDIFF.GE.2) THEN
c
c          with respect to state twice
c
      DFIDXDX(4,3,3)=3.0D0*(1-X(6))*(PAR(1)/(1.0D0-X(3)))**2**2
      DFIDXDX(4,3,6)=- (PAR(1)**2)/(1.0D0-X(3))**3
      DFIDXDX(4,6,3)=- (PAR(1)**2)/(1.0D0-X(3))**3
      DFIDXDX(5,5,5)=-6.0D0*X(5)
      DFIDXDX(5,5,6)=-2.0D0*X(6)
      DFIDXDX(5,6,5)=-2.0D0*X(6)
      DFIDXDX(5,6,6)=-2.0D0*X(5)
      DFIDXDX(6,5,5)=-2.0D0*X(6)
      DFIDXDX(6,5,6)=-2.0D0*X(5)
      DFIDXDX(6,6,5)=-2.0D0*X(5)
      DFIDXDX(6,6,6)=-6.0D0*X(6)
c
c          with respect to state and parameters
      DFIDXDP(4,3,3)=2.0D0*PAR(1)*(1-X(6))/(1.0D0-X(3))**3
      DFIDXDP(4,6,3)=-PAR(1)/(1.0D0-X(3))**2
      DFIDXDP(5,6,4)=2.0D0
      DFIDXDP(6,5,4)=-2.0D0
c
      END IF
c
      ELSE IF (SEGNO.EQ.2) THEN
c
c          -----
c          Vector field 2
c          -----
c
c          Right-hand side
c          -----
c
      FI(1)=0.2*(X(2)+0.04D0*X(3)
+      -0.5D0*(1-X(5))*(PAR(1)/(1.0D0-X(2)))**2)-3.17844
      FI(2)=X(3)
      FI(3)=1.2*(-X(2)-0.04D0*X(3)

```

```

+      +0.5D0*(1-X(5))*(PAR(1)/(1.0D0-X(2)))**2)+3.17844
      FI(4)=X(4) + 2*PAR(2)*X(5) - X(4)*(X(4)**2+X(5)**2)
      FI(5)=X(5) - 2*PAR(2)*X(4) - X(5)*(X(4)**2+X(5)**2)

c
c      First derivatives
c      -----
c      IF (GCIDIFF.GE.1) THEN
c
c          with respect to state
      DFIDX(1,2)=0.2*(1.0D0 - (1-X(5))*(PAR(1)**2)/(1.0D0-X(2)))**3)
      DFIDX(1,3)=0.2*(0.04D0)
      DFIDX(1,5)=0.2*(0.5D0*(PAR(1)**2)/(1.0D0-X(2)))**2)
      DFIDX(2,3)=1.0D0
      DFIDX(3,2)=-1.2*(1.0D0 - (1-X(5))*(PAR(1)**2)/(1.0D0-X(2)))**3)
      DFIDX(3,3)=-1.2*(0.04D0)
      DFIDX(3,5)=-1.2*(0.5D0*(PAR(1)**2)/(1.0D0-X(2)))**2)
      DFIDX(4,4)=1.0D0 - 3.0D0*X(4)**2 - X(5)**2
      DFIDX(4,5)=2.0D0*(PAR(2) - X(4)*X(5))
      DFIDX(5,4)=-2.0D0*(PAR(2) + X(4)*X(5))
      DFIDX(5,5)=1.0D0 - 3.0D0*X(5)**2 - X(4)**2

c
c          with respect to parameters
      DFIDP(1,1)=-0.2*PAR(1)*(1-X(5))*(1/(1.0D0-X(2)))**2
      DFIDP(3,1)=1.2*PAR(1)*(1-X(5))*(1/(1.0D0-X(2)))**2
      DFIDP(4,2)=2.0D0*X(5)
      DFIDP(5,2)=-2.0D0*X(4)

c
c      END IF

c
c      Second derivatives
c      -----
c      IF (GCIDIFF.GE.2) THEN
c
c          with respect to state twice
      DFIDXDX(2,3,3)=0.2*3.0D0*(1-X(6))*(PAR(1)/(1.0D0-X(3)))**2)**2
      DFIDXDX(2,3,6)=-0.2*(PAR(1)**2)/(1.0D0-X(3))**3
      DFIDXDX(2,6,3)=-0.2*(PAR(1)**2)/(1.0D0-X(3))**3
      DFIDXDX(4,3,3)=1.2*3.0D0*(1-X(6))*(PAR(1)/(1.0D0-X(3)))**2)**2
      DFIDXDX(4,3,6)=-1.2*(PAR(1)**2)/(1.0D0-X(3))**3
      DFIDXDX(4,6,3)=-1.2*(PAR(1)**2)/(1.0D0-X(3))**3
      DFIDXDX(5,5,5)=-6.0D0*X(5)
      DFIDXDX(5,5,6)=-2.0D0*X(6)
      DFIDXDX(5,6,5)=-2.0D0*X(6)
      DFIDXDX(5,6,6)=-2.0D0*X(5)

```

```

DFIDXDX(6,5,5)=-2.0D0*X(6)
DFIDXDX(6,5,6)=-2.0D0*X(5)
DFIDXDX(6,6,5)=-2.0D0*X(5)
DFIDXDX(6,6,6)=-6.0D0*X(6)
c
c      with respect to state and parameters
DFIDXDP(4,3,3)=2.0D0*PAR(1)*(1-X(6))/(1.0D0-X(3))**3
DFIDXDP(4,6,3)=-PAR(1)/(1.0D0-X(3))**2
DFIDXDP(5,6,4)=2.0D0
DFIDXDP(6,5,4)=-2.0D0
c
      END IF
c
      ELSE
      PRINT *, 'GCFUNC error: SEGNO=', SEGNO
      STOP
      END IF
c
RETURN
END
c
-----
SUBROUTINE GCBOUND(GCNDIM,X,PAR,GCIDIFF,
+ H,DHDX,DHDP,DHDXX,DHDXDP,SEGNO)
-----
c
      IMPLICIT DOUBLE PRECISION (A-H,O-Z)
c
      INCLUDE 'mems.h'
c
      INTEGER GCNDIM,GCIDIFF,PHANI
      INTEGER SEGNO
c
      DIMENSION X(GCNDIM),PAR(*),DHDX(GCNDIM),DHDP(*)
      DIMENSION DHDXX(GCNDIM,GCNDIM),DHDXDP(GCNDIM,*)
c
      -----
c      Discontinuity boundary
c      -----
c
      IF (SEGNO.EQ.1) THEN
c
      boundary function
c      -----
      H=0.5D0-X(2)

```

```
c
c   First derivatives
c   -----
c   IF (GCIDIFF.GE.1) THEN
c
c       with respect to state
c       DHDX(2)=-1.0D0
c
c       with respect to parameters
c
c   END IF
c
c   Second derivatives
c   -----
c   IF (GCIDIFF.GE.2) THEN
c
c       with respect to state twice
c
c       with respect to state and parameters
c
c   END IF
c
c   ELSE IF (SEGNO.EQ.2) THEN
c
c       boundary function
c       -----
c       H=X(1)
c
c       First derivatives
c       -----
c       IF (GCIDIFF.GE.1) THEN
c
c           with respect to state
c           DHDX(1)=1.0D0
c
c           with respect to parameters
c
c       END IF
c
c       Second derivatives
c       -----
c       IF (GCIDIFF.GE.2) THEN
c
c           with respect to state twice
c
```

```

c      with respect to state and parameters
c
c      END IF
c
c      END IF
c
c      RETURN
c      END
c
c      -----
c      SUBROUTINE GCSTPNT(GCNDIM,X,PAR,T,SEGNO)
c      -----
c
c      IMPLICIT DOUBLE PRECISION (A-H,O-Z)
c
c      INCLUDE 'mems.h'
c
c      INTEGER GCNDIM,SEGNO
c
c      DIMENSION X(GCNDIM),PAR(*)
c
c      Initialize parameters
c      -----
c
c      PAR(1)=0.59798D0
c      PAR(2)=0.8D0
c      PAR(61)=3.9267D0
c      PAR(62)=0
c
c      Initialize solution
c      -----
c
c      RETURN
c      END
c
c      -----
c      SUBROUTINE GCPVLS(GCNDIM,X,PAR,SEGNO)
c      -----
c
c      IMPLICIT DOUBLE PRECISION (A-H,O-Z)
c
c      INCLUDE 'mems.h'
c
c      INTEGER GCNDIM,SEGNO

```

```

c
c      DIMENSION X(GCNDIM),PAR(*)
c
c      User functions
c      -----
c      PAR(?)=?
c
c
c      RETURN
c      END
c
c      -----
c      SUBROUTINE GCBCND
c      -----
c
c      Dummy subroutine
c
c      RETURN
c      END
c
c      -----
c      SUBROUTINE GCSOLVALHP(GCNDIM,PAR,X,HP,SEGNO)
c      -----
c
c      Returns the value of the Poincare function Hp
c      evaluated on the solution points
c
c      IMPLICIT DOUBLE PRECISION (A-H,O-Z)
c      INTEGER SEGNO
c
c      INCLUDE 'gccont.h'
c
c      DIMENSION X(GCNDIM),PAR(*)
c
c      Poincare section
c      -----
c      DOUBLE PRECISION HP
c
c      Poincare section definition
c      -----
c      IF (SEGNO.EQ.1) THEN
c
c          HP=-X(3)
c
c      ELSE IF (SEGNO.EQ.2) THEN

```

```

C
      HP=0.2*(X(2)+0.04D0*X(3)
+      -0.5D0*(1-X(5))*(PAR(1)/(1.0D0-X(2)))**2)-3.17844
C
      END IF
C
      RETURN
      END
C
-----
C
SUBROUTINE GCPOINCARE(GCNDIM,X,PAR,GCIDIFF,
+ HPI,DHPIDX,DHPIDP,DHPIDXDX,DHPIDXDP)
C
-----
C
      IMPLICIT DOUBLE PRECISION (A-H,O-Z)
C
      INCLUDE 'mems.h'
C
      INTEGER GCNDIM,GCIDIFF,PHANI
C
      DIMENSION X(GCNDIM),PAR(*),DHPIDX(GCNDIM),DHPIDP(*)
      DIMENSION DHPIDXDX(GCNDIM,GCNDIM),DHPIDXDP(GCNDIM,*)
C
C
      RETURN
      END
C
-----
C
SUBROUTINE GCICND
C
-----
C
      Dummy subroutine
C
      RETURN
      END
C
-----
C
SUBROUTINE GCFOPT
C
-----
C
      Dummy subroutine
C
      RETURN
      END
C

```

```

c -----
c SUBROUTINE JUMPMAP(GCNDIM,U1,PAR,UJUMP,
+ COEFFRES,UJUMPDX,UJUMPDP,SEGNO)
c -----
c
c IMPLICIT DOUBLE PRECISION (A-H,O-Z)
c
c INCLUDE 'mems.h'
c INCLUDE 'gccont.h'
c
c INTEGER GCNDIM,SEGNO
c
c DIMENSION U1(GCNDIM)
c DIMENSION UJUMP(GCNDIM)
c DIMENSION PAR(*)
c DIMENSION UJUMPDX(GCNDIM,GCNDIM)
c DIMENSION UJUMPDP(GCNDIM,*)
c
c DOUBLE PRECISION PHANI
c
c DATA PHANI/0.0D0/
c
c COEFFRES=0.80D0
c
c Debug
c IF (DEBUG) THEN
c   IF (DBGLEV.GE.DBGL2) THEN
c     PRINT *,'enter in JUMPMAP'
c   END IF
c END IF
c
c IF (SEGNO.EQ.1) THEN
c
c   DO K=1,GCNDIM
c     UJUMP(K)=U1(K)
c   END DO
c   UJUMP(1)=U1(1)+(1+COEFFRES)*U1(3)/6
c   UJUMP(3)=-COEFFRES*U1(3)
c
c Derivatives of the jump map w.r.t the state
c UJUMPDX(1,1)=1.0D0
c UJUMPDX(1,3)=(1+COEFFRES)/6
c UJUMPDX(2,2)=1.0D0
c UJUMPDX(3,3)=-COEFFRES
c UJUMPDX(4,4)=1.0D0

```

```
      UJUMPDX(5,5)=1.0D0
c
ELSE IF (SEGNO.EQ.2) THEN
c
      DO K=1,GCNDIM
        UJUMP(K)=U1(K)
      END DO
c
c      Derivatives of the jump map w.r.t the state
      UJUMPDX(1,1)=1.0D0
      UJUMPDX(2,2)=1.0D0
      UJUMPDX(3,3)=1.0D0
      UJUMPDX(4,4)=1.0D0
      UJUMPDX(5,5)=1.0D0
c
      END IF
c      Derivatives of the jump map w.r.t the parameters
c
RETURN
END
c
```

Appendix D

\widehat{TC} Constants File <name> .dat

t	X1	X2	X3	.
0.0000000000000000	0.0000000000000000	0.5000000000000000	-0.0000000000000001	.
0.0111679249845897	0.0000000000000000	0.4999688308510247	-0.0055817549964804	.
0.0264340963409201	0.0000000000000000	0.4998254026508901	-0.0132070988582660	.
0.0417228099319304	0.0000000000000000	0.4995651838610360	-0.0208306768444159	.
0.0570544546593348	0.0000000000000000	0.4991873416469904	-0.0284542533340556	.
0.0724575218955978	0.0000000000000000	0.4986902588581793	-0.0360834013476695	.
0.0879508614380055	0.0000000000000000	0.4980720037397322	-0.0437185845208427	.
0.1035706129400290	0.0000000000000000	0.4973293188809573	-0.0513683290744998	.
0.1193362213237477	0.0000000000000000	0.4964589708833897	-0.0590323543110860	.
0.1352957785187343	0.0000000000000000	0.4954553713008992	-0.0667235154828182	.
...
...
1.0000000000000000	0.0000000000000000	0.4954553713008992	-0.0667235154828182	.

Vita

Phanikrishna Thota was born in Nizamabad, India, on April 24, 1980 and lived there for seventeen years until he moved to Hyderabad in August-1997 to attend the Jawaharlal Nehru Technological University College of Engineering. As a result he received a Bachelors degree in Mechanical Engineering in June 2001. He later came to the United States of America to attend the University of Kentucky in July 2001 and completed his Masters program with Mechanical Engineering as his major. In 2003, he joined Dr. Harry Dankowicz at the Department of Engineering Science and Mechanics at Virginia Tech to continue for his Ph.D. He then moved to University of Illinois at Urbana-Champaign along with his advisor as a visiting scholar to that university.